Universitat Autònoma de Barcelona

# The accretion flow onto white dwarfs and its X-ray emission properties

**NATALY OSPINA ESCOBAR**

DOCTORAL THESIS

# The accretion flow onto white dwarfs and its X-ray emission properties

*Author:*
NATALY OSPINA ESCOBAR

*Supervisor:*
Dr. MARGARITA HERNANZ CARBÓ

*Tutor:*
Dr. JAVIER RODRÍGUEZ VIEJO

*A thesis submitted in fulfillment of the requirements for the degree of Doctor of Philosophy*

*in the*

UNIVERSITAT AUTÒNOMA DE BARCELONA

Universitat Autònoma de Barcelona

DEPARTAMENT DE FÍSICA

ICE CSIC Consejo Superior de Investigaciones Científicas IEEC

June 26, 2017

# *Abstract*

Explosive burning of hydrogen on top of accreting white dwarfs causes nova outbursts. The binary system where classical novae occur is a cataclysmic variable (main sequence star companion), whereas (some) recurrent novae occur in symbiotic binaries (red giant star companion). The analysis of the X-ray emission from novae in their post outburst stages provides important information about the nova explosion mechanism and the reestablishment of accretion. In some cases, like V2487 Oph 1998, observations with XMM-Newton a few years after outburst indicate that accretion was re-established; X-ray spectra look like those of magnetic cataclysmic variables (of the intermediate polar class). In this work a numerical model of the accretion flow onto magnetic white dwarfs and of their corresponding X-ray emission has been developed to be compared with observations of post outburst novae where accretion is active again. We have obtained the distributions of the different physical quantities that describe the emission region, temperature, density, pressure and velocity, for different masses of the white dwarf and accretion rates. The associated X-ray spectrum is also obtained. These results have been applied to the nova V2487 Oph 1998 with the aim to obtain its white dwarf mass since this nova has been identified as a good candidate for a recurrent nova and a type Ia Supernova progenitor.

# CONTENTS

# INTRODUCTION

## Motivation

White Dwarfs are attractive experimental laboratories where the electron degeneracy plays an important role for supporting the stars against gravity. Accretion in white dwarf systems can occur through discs, accretion columns or directly onto the magnetic poles, depending of the magnetic field of the white dwarf. A white dwarf accretes matter from a companion star, typically a red dwarf, that fills its Roche lobe. This matter forms an accretion disc inside the Roche lobe of the white dwarf. The disc, however, is disrupted by the white dwarf magnetic field at some distance from the white dwarf surface. As a result the accreting matter freely falls onto the white dwarf surface and forms a strong shock near its surface.

An accreting white dwarf is of great importance in the Universe because some of them probably cause type Ia Supernova explosions as the white dwarf mass reaches the Chandrasekhar limit, and deliver synthesized heavy elements out to the surrounding space.
Because the exact scenario leading to these explosions is still unclear, X-rays are crucial to study the recovery of this accretion in outburst and post outburst novae. They provides unique and crucial information about the characteristics of the white dwarf, mass, chemical composition, luminosity, the accreted material, chemical composition, and those related with the properties of the binary system, mass accretion rate, which are determining to understand the explosion mechanism.
Soft X-rays reveal the hot white dwarf photosphere, whenever hydrogen nuclear burning is still on and expanding envelope is transparent enough, whereas harder X-rays give information about the ejecta and/or the accretion flow in the reborn cataclysmic variable. Therefore, high resolution spectra provide a new way of measuring the mass of the white dwarf. The emission line ratios give the plasma temperature of the accretion shock, which through accretion shock theory and a mass-radius relationship, yields the white dwarf mass (e.g. Ishida & Fujimoto (1995)).

The purpose of this work is to study the structure of the emission region, temperature,

density, pressure and gas velocity distributions, and to calculate the X-ray spectrum from this region. A numerical model of accretion onto white dwarf is presented and is used to determine the parameters and the estructure of the emission region of the Nova Oph 1998 (V2487 Oph).

V2487 Oph has been observed with the *XMM-Newton* and *INTEGRAL* satellites in different epochs. The analysis of the 4th and 5th observations of *XMM-Newton*, 4.3 and 8.8 years after outburst, respectively are presented. Also, the analysis of the *INTEGRAL* observations for this nova combined with the *XMM-Newton* observations are shown. Finally, as the X-ray spectra can be used for white dwarf mass determination, the white dwarf mass have been determined and compared with the mass determination of Hachisu et al. (2002). We have obtained a value of $M_{WD} = 1.39\ \mathrm{M}_{\odot}$ which is slightly higher than the determined by Hachisu et al. (2002), $M_{WD} = 1.35\ \mathrm{M}_{\odot}$, from the visual light curve.

## Contents of this thesis

This thesis is organized as follows; In Chapter 1, we briefly review the scenario of white dwarf binaries in close binary systems and its X-ray emission properties. In Chapter 2, we refer some of the main accretion column structure models which has been utilized to study the structure of the emission region and to estimate the white dwarf mass. In Chapter 3, we describe the physical quantities of the emission region required to model the observed X-ray spectra and we represent the spectrum models of the thermal plasma. In Chapter 4, we review the famous Nova Oph 1998, and apply the spectral model to the *XMM-Newton* and *INTEGRAL* data of this nova, and we discuss our new results in relation to the white dwarf mass estimation. Finally, Chapter 5 summarizes conclusions of this thesis and describes future prospects.

# 1

# WHITE DWARFS IN CLOSE BINARY SYSTEMS

White dwarfs (WDs) are the endpoints of stellar evolution of almost 98% of low-mass stars with masses smaller than $8-10M_{\odot}$. Typical white dwarf masses goes from $\sim 0.6M_{\odot}$ to a maximum value equal to the Chandrasekhar mass, $\sim 1.4M_{\odot}$, (Chandrasekhar, 1931). Their chemical composition is either a carbon-oxygen (CO) or an oxygen-neon (ONe) mixture, although it can also be pure He. These stars no longer burn nuclear fuel. Instead, they are slowly cooling as they radiate away their residual thermal energy to very low luminosities, typically $L \sim 10^{-4.5}L_{\odot}$, when isolated. These stars can also be found in close binary systems where they can explode when they are accreting matter.

When a binary system contains a compact object such as a white dwarf, gas from the other star can accrete onto the compact object. This releases gravitational potential energy, causing the gas to become hotter and emit radiation. There are two main types of binary systems in which white dwarfs can accrete matter and subsequently explode. The most common case is a *cataclysmic variable* (CV), where the companion is a main sequence star transferring hydrogen-rich matter. In this system, mass transfer occurs via Roche lobe overflow. As a consequence of accretion, hydrogen burning in degenerate conditions on top of the white dwarf leads to a thermonuclear runaway and a nova explosion, which does not disrupt the white dwarf. Therefore, after enough mass is accreted again from the companion star, a new explosion will occur with a typical recurrence time of $10^4 - 10^5$ years.
The second scenario where a white dwarf can explode as a nova is a *symbiotic binary*, where the white dwarf accretes matter from the stellar wind of a red giant companion.

This scenario leads to more frequent nova explosions than in cataclysmic variables, with typical recurrence periods smaller than 100 years.
Any differences between the isolated stars and the white dwarfs in CVs might then shed light on the physics of the accretion process itself.

## 1.1 Cataclysmic variables

As mentioned above, cataclysmic variables are close binary systems consisting of a white dwarf (primary star) and a low mass main sequence star or red giant (secondary star or companion star). The secondary star fills its Roche Lobe and the matter overflows the lobe is accreted by the primary white dwarf star (see Warner (1995); Ritter (2010); Knigge, Baraffe, & Patterson (2011) for reviews). As the name, CVs are stars which increase their brightness drastically on time scale from as short as a few seconds to several years.

Cataclysmic variables are primarily classified by observational properties as the strength of the magnetic field and characteristics of its optical variations. These characteristics are in turn believed to depend on the nature of the primary star and the accretion process. Wherefore the strenght of the magnetic field influences the physical conditions in the accretion and the dominant radiation mechanisms.
Systems in which the white dwarf surface magnetic field is $< 10^7$ G are called *non-magnetic CVs* and these systems display a variety of observational characteristics leading to further sub-types like: *(a)* classical novae which shows large eruptions of $\sim 6 - 19$ magnitudes in the optical; *(b)* recurrent Novae that are previous novae seen to re-erupt; *(c)* dwarf novae (DN) that shows regular outbursts of $\sim 2 - 5$ magnitudes and they are further classified into SU UMa stars showing occasional super-outbursts, Z Cam stars that shows protracted standstills between outbursts, and U Gem stars that are basically all other DN; *(d)* nova-like variables consisting of VY Scl stars which shows occasional drops in brightness and UX UMa stars consisting of all other non-eruptive variables; *(e)* AM Canum Venaticorum stars (AM CVn), characterized by a very short orbital period at $5 - 65$ min and the absence of hydrogen features but of helium lines. Cataclysmic variables in which the white dwarf surface magnetic field is very high, i.e., $\geq 10^7$ G, are called *magnetic CVs* (mCVs) and are further classified according to their magnetic field strengths in two varieties known as *(a)* Polars or AM Her systems, with a magnetic field around $10^{(7-9)}$ G, and *(b)* Intermediate Polars (IPs) or DQ Her systems, with a magnetic field lower than Polars, $10^{(5-7)}$ G. Nevertheles, there are a few mCVs with properties that are intermediate to those of Polars and Intermediate Polars (for details, see Section § 1.2). Basic classification of CVs is shown in Figure 1.1.

According to the accretion scenario, in the non-magnetic CVs accretion takes place via an accretion disk produced to conserve the angular momentum of the accreting material. In the mCVs, however, the pressure of the magnetic field disrupts completely or partially

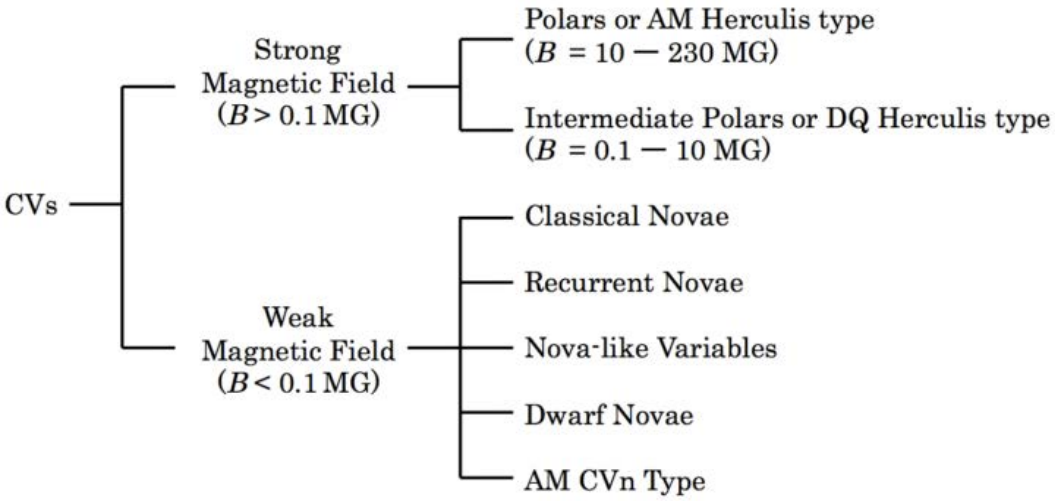


FIGURE 1.1: Clasification of cataclysmic variables. (From Hayashi (2014)).

the accretion disk depending on the strength of the magnetic field and the accreting material is guided along the magnetic field lines to the poles of the white dwarf in an accretion stream or an accretion curtain.

### 1.1.1 Polars

As mentioned before, the Polars, or AM Her systems following the name of its representative object, have a strong magnetic field $(10-230)$ MG. Since matter filling up the Roche lobe of the secondary star is captured by the magnetic field lines and accretes onto the magnetic pole, the accretion disk can not be formed around the white dwarf (see Figure 1.2).

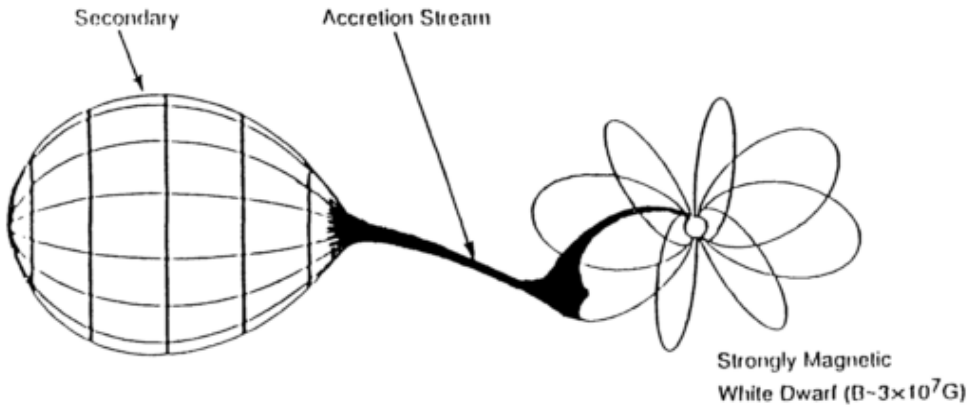


FIGURE 1.2: Schematic representation of geometry and components of a Polar. (From Cropper (1990)).

As white dwarfs in Polars are strongly magnetized, the most significant X-ray emission is the cyclotron cooling and it can dominate bremsstrahlung cooling (Lamb & Masters (1979); King & Lasota (1979)). The inclusion of cyclotron cooling lowers the average temperature of the emission region and hence softens the X-ray spectrum, which permit observes an excess of soft X-rays in Polars. In addition, this magnetic field is strong enough

for the orbital and spin periods of its white dwarf to be synchronized, $P_{orb} \simeq P_{spin}$ (for a review of Polars, see Cropper (1990)).

### 1.1.2 Intermediate Polars

Intermediate Polars, also called DQ Her systems, have a magnetic field as strong as $0.1 - 10$ MG. However this white dwarf field is too weak to synchronize its rotation with the orbital rotation (i.e. $P_{spin} \ll P_{orb}$).
Unlike Polars, most IPs have accreting disks, an schematic view of Intermediate Polar system is see in Figure 1.3, whereas in the inner region, the disk is truncated, and the gas almost freely falls onto a white dwarf channeled along its magnetic field. Near the white dwarf surface a stationary shock stands to convert the kinematic energy of the bulk gas motion into thermal energy (see Patterson (1994); Hellier (1996) for reviews of IPs). Because the temperature of the shock-heated gas is typically $> 10$ keV, and the density is low, hard X-rays are emitted via optically thin thermal emission and cyclotron cooling plays an insignificant role. Then, the heated gas forms a post shock region with a temperature gradient, wherein the gas descends while it cools via the X-ray emission (e.g. Aizu (1973); Frank, King, & Raine (1992); Wu (1994); Wu, Chanmugam, & Shaviv (1994)). As a result, the total spectrum from the post-shock region is observed as a sum of multi-temperature emission components.

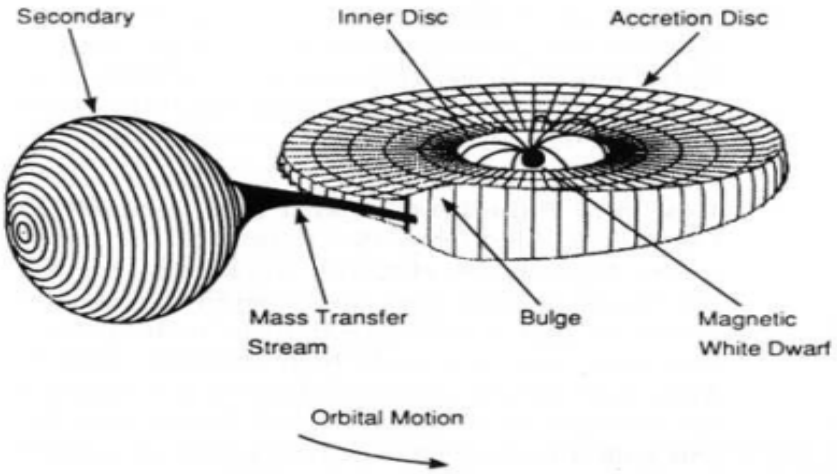


FIGURE 1.3: Schematic representation of geometry and components of an Intermediate Polar. (From Mason, Rosen, & Hellier (1988)).

## 1.2 X-rays emission from accreting white dwarfs

Accreting white dwarfs in binary systems have long been known to be X-ray emitters and accretion can occur through discs, accretion columns or a combination of these, depending on their magnetic fields.

In non-magnetic CVs, in which the magnetic field of the white dwarf is too weak to disrupt the accretion disk, the material in the inner disk must dissipate its rotational kinetic energy in order to accrete onto the slowly rotating white dwarf. During their quiescent state, non-magnetic CVs are profuse sources of hard X-rays, with energies of $10\ \mathrm{keV}$ or higher. The origin of the X-ray emission is thought to be a hot, optically thin plasma in the boundary layer, i.e. the transition region between the disk and the white dwarf. The structure of the boundary layer is poorly understood, and theoretical modeling is complicated by the strong shearing and turbulence present in the accretion flow (e.g., Narayan & Popham (1993)). Observations have shown that the X-ray emitting region is generally small and close to the white dwarf surface (e.g., Mukai et al. (1997)). Basic accretion theory predicts that half of the total accretion energy should emerge from the disk at optical and ultraviolet (UV) wavelengths, while the other half is released in the hot boundary layer as X-ray and extreme UV emission (Lynden-Bell & Pringle, 1974).
On the other hand, in magnetic CVs like Polars, the ionized infalling matter hits the magnetic field and coupled onto the magnetic field lines, flowing toward the orbital plane. The matter follows the magnetic field lines until it is piled up in an accretion column in the vicinity of the white dwarf magnetic poles, just above its surface, where all the radiation is emitted as a consequence of the accretion process. Otherwise an accretion disk can form which is disrupted at the magnetospheric radius. Again, the matter is forced along the field lines into the magnetic polar regions of the white dwarf, as occurs in typical situation for Intermediate Polars scenarios.
Early theories for accretion onto a magnetic white dwarf (Aizu (1973), Lamb & Masters (1979) and King & Lasota (1979)) predict that the matter falling in with supersonic velocities is decelerated by a factor of $\sim 4$ (Rankine Hugoniot conditions) and heated to $\sim 10^8$ K in a strong shock standing above the white dwarf surface. Hence, for magnetic CVs the kinetic energy is released from the post-shock flow in the form of thermal bremsstrahlung at hard X-ray energies with typically $kT_{br} \sim 10 - 60\ \mathrm{keV}$ (Warner, 1995) as well as cyclotron radiation in the optical and infrared. It is expected that half of the hard bremsstrahlung radiation is detected directly and the other half is intercepted by the white dwarf photosphere. Here photons with $kT \leq 10\ \mathrm{keV}$ are preferentially absorbed and the radiation is re-emitted at lower energies as soft X-rays and extreme ultaviolet (EUV). Reprocessed radiation from the illuminated photosphere is emitted as a blackbody soft X-ray component with $kT_{bbody} \sim 25 - 100\ \mathrm{eV}$.
With increasing magnetic field, cyclotron cooling becomes more and more efficient, reducing the maximum temperature in the shock and, hence, increasing the cyclotron emission in comparison with that of thermal bremsstrahlung. For this reason in Polars the cyclotron emission is dominant and in X-rays they are detected mainly at lower energies (soft X-ray band). On the other hand, in systems where the magnetic pressure does not inhibit the formation of the accretion disk, i.e., IPs, due to higher mass flow rate, $\dot{M}$, the emergent emission is essently of the thermal bremsstrahlung type.
However a fraction of the hard X-rays produced in the post-shock region can illuminate the white dwarf photosphere and be reflected, and eventually reach the distant observer.

This effect is visible through the detection of a fluorescent Fe K$\alpha$ emission line at $6.4$ keV, indicating neutral Fe, a clear signature of a mass flow accreting onto the white dwaf. This is likely produced in CVs by reflection in the accretion disk for non-magnetic systems (e.g. Rana et al. (2006)) and in the cooler pre-shock flow (Ezuka & Ishida, 1999) or in the white dwarf surface for magnetic CVs (Matt (1999) for a review). In any case, this feature reveals reflection of hard X-rays on cold matter, although a detailed analysis of spectra reveals that the $6.4$ keV line is often associated to Fe complex lines due to thermal bremsstrahlung process. Two other Fe K$\alpha$ emission lines could be produced by iron in intermediate states of ionization (Hellier & Mukai, 2004) from plasmas with temperatures of $10^7 - 10^8$ K at $6.68$ keV (Fe XXV, i.e. He-like Fe) and $6.97$ keV (Fe XXVI, i.e. H-like Fe), whereas the fluorescent line comes from relatively neutral iron (Fe I-XVII) having temperatures $\leq 10^6$ K. Therefore the observation of the Fe K$\alpha$ fluorescence emission line requires that accretion is active. This is quite usual in accreting white dwarfs in magnetic cataclysmic variables, mostly in Intermediate Polars (Hellier et al. (1996), Fujimoto & Ishida (1997), Haberl, Motch, & Zickgraf (2002)), de Martino et al. (2004), Evans & Hellier (2007)), but also in non-magnetic systems (see, e.g., Pandel et al. (2005) and Rana et al. (2006)).

Since IPs host weakly magnetized white dwarfs with respect to Polars this could qualitatively explain why they are hard X-ray emitters. However, in the last years a soft and rather absorbed X-ray emission has been found in a growing number of Intermediate Polars. The ROSAT satellite was the first to discover IPs with a significant soft X-ray component, $E < 2$ keV, (Mason et al. (1992); Haberl et al. (1994); Motch et al. (1996); Burwitz et al. (1996)). Such a component was also recognized in a few other systems observed with BeppoSAX (de Martino et al. (2004)) and with the XMM-Newton (Haberl, Motch, & Zickgraf (2002); de Martino et al. (2004); de Martino et al. (2008); Staude et al. (2008); Evans & Hellier (2007)).
Moreover, as noted by Anzolin et al. (2008), in most cases the black-body temperatures, $50 - 120$ eV, are larger than those found in Polars, $20 - 60$ eV, and with a lower soft-/hard flux ratio. The higher temperatures found in IPs indicate higher accretion rates, in line with higher luminosities. Multiple and partial absorption is also seen in the soft X-ray spectra of IPs (e.g., see Girish & Singh (2012)) indicating the presence of complicated patterns of absorption by accretion curtains in the line of sight. The detection of a soft X-ray optically thick component in these systems (see Anzolin et al. (2009); Girish & Singh (2012)) poses further questions in the interpretation of the X-ray emission properties of IPs.

In addition, recent X-ray observations with XMM-Newton of Polars in high states of accretion have revealed an increasing number of systems that do not exhibit a distinct soft X-ray component but rather a more 'IP-like' X-ray spectrum (Ramsay & Cropper (2004); Vogel et al. (2008); Ramsay et al. (2009); Bernardini et al. (2014)). However, the magnetic fields and orbital periods of these Polars do not appear to be very dissimilar from all other

Polars with a more classic type of behaviour. Hence, the distinction between the two subclasses now appears less marked than ever before, requiring further investigations and trying to understand the evolutionary link between IPs and Polars.

# 2

# ACCRETION COLUMN STRUCTURE MODELS

## 2.1 History of post-shock accretion column modeling

The standard model of accretion onto white dwarfs was developed in the 1970s by Hoshi (1973) and Aizu (1973).

Hoshi (1973) considered a steady and spherically symmetric accretion model onto white dwarfs and proposed a fully numerical calculation solving the hydrodynamic equations by direct numerical integration. Near the white dwarf surface a shock is formed and a hot plasma between the shock front and the white dwarf surface emits thermal radiation, this region between the white dwarf's surface and the shock is called the "emission region". He estimated some physical quantities, for example, an effective temperature and emission measure following his model, however did not calculate the distribution of the physical quantities.

Aizu (1973) analytically calculated the distributions of the temperature and density in parallel to the plasma flow for the pure bremsstrahlung case. He solved hydrodynamic equations using the method of successive approximation and provided a conversion formula to determined the white dwarf mass based on the effective temperature of the bremsstrahlung spectrum. Aizu (1973) assumed that the thickness of the emission region, which correspond to the accretion column height, is negligible against the white dwarf radius. This assumption means that the gravitational potential is constant in the

emission region and there is not energy input.

Since Aizu (1973) assumption is reasonable and the distributions of the physical quantities are useful for estimation of observed spectra, his model had been used to reproduce the observed spectra for more than ten years after his publication.

These models have been developed along the years including different effects like white dwarf gravity, influence of cyclotron and compton cooling, power-law cooling function, electron conduction and electron leaking and taken into account both planar and spherical geometries. Some of them considered also geometrically extended post-shock region, modified formulation and boundary conditions and solved the hydrodynamic equations by direct numerical integration and analytical and semi-analytical approximations (e.g. Fabian, Pringle, & Rees (1976); Hayakawa & Hoshi (1976); Katz (1977); King & Lasota (1979); Kylafis & Lamb (1979); Wada et al. (1980); Imamura (1981); Langer, Chanmugam, & Shaviv (1981); Langer, Chanmugam, & Shaviv (1982); Chevalier & Imamura (1982); Frank, J. King, A. R. and Lasota (1983); Imamura & Durisen (1983); Frank & King (1984); Chanmugam, Langer, & Shaviv (1985); Imamura et al. (1987); Wolff, Gardner, & Wood (1989); Wu, Kinwah and Wickramasinghe (1992); Frank, King, & Raine (1992); Wu (1994); Wu, Chanmugam, & Shaviv (1994); Wu, Chanmugam, & Shaviv (1995) Imamura et al. (1996); Woelk, U. and Beuermann (1996); Saxton et al. (1998); Ramsay et al. (1998); Cropper et al. (1999); Ezuka & Ishida (1999); Saxton (1999); Saxton & Wu (1999);Wu & Cropper (2001); Beardmore, Osborne, & Hellier (2000); Canalle et al. (2005); Saxton et al. (2005); Saxton et al. (2007); Hayashi & Ishida (2014a)).
Some of these models were used to estimate the white dwarf masses in several Intermediate Polars and Polars (Cropper, Ramsay, & Wu (1998); Ramsay (2000); Revnivtsev et al. (2004); Falanga, Bonnet-Bidaud, & Suleimanov (2005); Suleimanov, Revnivtsev, & Ritter (2005); Brunschweiger et al. (2009); Yuasa et al. (2010); Hayashi & Ishida (2014b)). However, in all these models the accreting plasma was assumed to fall from infinity. Suleimanov et al. (2016) eliminates this assumption and proposed a new method for simultaneous determination of the white dwarf mass and the magnetospheric radius.

At the moment, Aizu (1973) model is the most widely used in the description of the post-shock accretion column structure. This model and the analytical model of Frank, King, & Raine (2002), which is based on the assumption of constant pressure in the post shock region, are introduced below.

### 2.1.1 Aizu Model

Aizu (1973) studied the accretion of gas by a white dwarf. In particular, the structure of a hot plasma formed by accretion. He found that the temperature distribution in the plasma is determined only by the mass of the star, while the density and the thickness of the plasma depends also on the accretion rate.

The accretion is assumed to be steady and spherically symmetric. Near the stellar surface a shock front is formed at ($r = R + x$: shock wave position; where $x$ is the thickness of the region and $R$ the stellar radius) and a hot plasma between the front and the surface emits thermal bremsstrahlung.
If the accretion rate is not small, the plasma density is not small and the cooling time of the hot plasma is short. Then, the thickness $x$ of this region is small compared with the stellar radius $R$ and the gravity change in this region can be neglected; At the shock wave, the gas density ($\rho$), pressure ($P$), velocity ($v$: inward direction is taken as positive) and temperature ($T$) have discontinuities. Suffixes $f$ and $b$ are used to refer the *front* and *back* sides of the shock wave. In the case of a strong shock these quantities are given by Hoshi (1973):

$$v_f = 4v_b = \left(\frac{2GM}{R}\right)^{1/2} \tag{2.1}$$

$$T_b = \left(\frac{3}{8}\right)\left(\frac{GMm_H\mu}{kR}\right) \tag{2.2}$$

$$\rho_f = \rho_b/4 = \left(4\pi R^2 v_f\right)^{-1} A \tag{2.3}$$

where $G$, $k$, $m_H$ and $\mu$ are the gravitational constant, the boltzmann constant, the mass of a hydrogen atom and the mean molecular weight of the falling gas ($\mu = 0.615$[1]), respectively.

The equations of continuity, motion and energy are given respectively by (See details of general hydrodynamics formulation in Appendix A):

$$\rho v r^2 = \rho_b v_b (R + x)^2 = A/4\pi \tag{2.4}$$

$$v\left(\frac{dv}{dr}\right) + \rho^{-1}\left(\frac{dp}{dr}\right) + \frac{GM}{r^2} = 0 \tag{2.5}$$

$$\rho v T\left(\frac{dS}{dr}\right) = \rho\varepsilon_{ff} \tag{2.6}$$

Where, $S$ is the entropy per unit mass:

$$S = \left(\frac{3kT}{2\mu m_H}\right)\ln(T\rho^{-2/3}) \tag{2.7}$$

The hot plasma of this region is assumed to be optically transparent and its energy loss is due only to the thermal bremsstrahlung. Its rate per unit of mass, $\varepsilon_{ff}$, is given by

[1]The gas is assumed to be composed only by Hydrogen and Helium with the chemical composition in mass as $X = 0.7$ and $Y = 0.3$.

(Hayakawa, Matsuoka, & Sugimoto, 1966):

$$\varepsilon_{ff} = 4\sqrt{\frac{\pi}{2}}\left(\frac{8e^6}{3\pi c^2 m\hbar}\right)\left(\frac{k}{mc^2}\right)^{1/2}\frac{1}{\mu_e}\sum_i \frac{Z_i^2}{\mu_i}\overline{G}\rho T^{1/2} \quad \mathrm{erg/gm\ s}$$

If the cooling time is defined by:

$$t_c = \frac{3kT}{2\mu m_H \varepsilon_{ff}} \tag{2.8}$$

its possible write the energy equation (Equation (2.6)) as:

$$v\frac{d}{dr}\ln(T\rho^{-2/3}) = t_c^{-1} \tag{2.9}$$

Taking the bottom of the emission region as the place where the falling gas cools appreciably, the thickness $x$ is estimated as $x \sim vt_c$, and this quantity can be calculated on the *back* side of the shock front as:

$$x \sim v_b t_{cb} \equiv x_b \tag{2.10}$$

For simplicity, Aizu (1973) assumed that the *bottom* of the emission region coincides with the stellar surface, neglecting the structure of the photosphere.

Now, introducing non-dimensional quantities:

$$y = \tfrac{v}{v_b}, \qquad z = \tfrac{T}{T_b}, \qquad u = \tfrac{r}{R+x}$$

and using:

$$\alpha = x_b/R \tag{2.11}$$

$$q = \frac{R}{R+x} \tag{2.12}$$

its possible rewrite Equations (2.4)∼(2.6) in the following forms:

$$\rho = \rho_b y^{-1} u^{-2} \tag{2.13}$$

$$[y - (3zy^{-1})]dy + 3dz + (-6zu^{-1} + 8u^{-2})du = 0 \tag{2.14}$$

$$\alpha q u^2 y^2 z^{1/2} d\ln(zy^{2/3}u^{4/3}) = du \tag{2.15}$$

The boundary conditions at the shock front are:

$$y = z = u = 1 \tag{2.16}$$

and near the stellar surface where a steady sink of the flow is assumed,

$$y \to 0 \qquad z \to 0 \qquad \text{as} \qquad u \to q \tag{2.17}$$

The unknown parameter $q$ is determined by Equations (2.13)$\sim$(2.15) together with the boundary conditions (2.16) and (2.17).

The equations are solved in the expansion of $\alpha$. The zeroth-order quantities are denoted by suffix 0, and the first-order ones by a suffix 1. We select $y$ as independent variable since the zeroth-order approximation of Equation (2.15) yields at constant $u_0$. Therefore, we can assume the following expansions:

$$z = z_0 + \alpha z_1 \qquad u = u_0 + \alpha u_1 \qquad q = q_0 + \alpha q_1$$

In this expansion the boundary conditions (2.16) and (2.17) become:

$$z_0 = u_0 = 1 \qquad z_1 = u_1 = 0 \qquad \text{at} \qquad y = 1 \tag{2.18}$$

$$z_0 \to 0, \quad u_0 \to q_0 \quad \text{and} \quad z_1 \to 0, \quad u_1 \to q_1 \quad \text{as} \quad y \to 0 \tag{2.19}$$

Therefore the zeroth-order solutions of Equations (2.14) and (2.15) are:

$$u_0 = 1, \quad q_0 = 1 \quad \text{and} \quad z_0 = y(4-y)/3 \tag{2.20}$$

The first approximation provides variations of physical quantities as a function of the distance $r$. Applying the boundary conditions (2.18), the relation between the relative distance and relative velocity is given by:

$$\begin{aligned}(r - R - x)/R &\cong \alpha u_1 \\ &= (8/9\sqrt{3})\alpha[15\sin^{-1}(1-(y/2)) - (5\pi/2) - (39\sqrt{3}/4) \\ &\quad + \{15 + (5/2)y + 2y^2\}\{y(1-(y/4))\}^{1/2}]\end{aligned} \tag{2.21}$$

Applying the boundary conditions (2.19) to Equation (2.21), and taking into account that $\alpha q_1 = -x/(R+x) \cong -x/R$, it is possible obtain:

$$x = -(8/9\sqrt{3})x_b[15\sin^{-1}(1) - (5\pi/2) - (39\sqrt{3}/4)] = 0.605x_b \tag{2.22}$$

The first-order approximation of the relative temperature as a function of the relative velocity is:

$$\begin{aligned}z_1 = (64/9\sqrt{3})y[(\pi/6) + (13\sqrt{3}/16) - \sin^{-1}(1-(y/2)) \\ - \{1 + y - (y^2/2) + (y^3/8)\}\{y(1-(y/4))\}^{1/2}]\end{aligned} \tag{2.23}$$

The left panel of Figure 2.1 shows $z_0$, $z_1$ and $z_0 + \alpha z_1$ as functions of the relative height $(r-R)/x$. The temperature drops relatively slowly as the gas flows over the emission region. The dominant feature of the temperature distribution is determined only by the stellar mass and is not influenced by the accretion rate as long as the latter is not too small.

The right panel of Figure 2.1 shows the square of relative velocity $y^2 = (v/v_b)^2$ (*black*), relative density $\rho/\rho_b$ (*red*) and relative pressure (*blue*) given as functions of $(r - R)/x$. It is seen the increase of density as the gas aproaches to the surface is slow over most of the emission region, but it sharp near the surface.

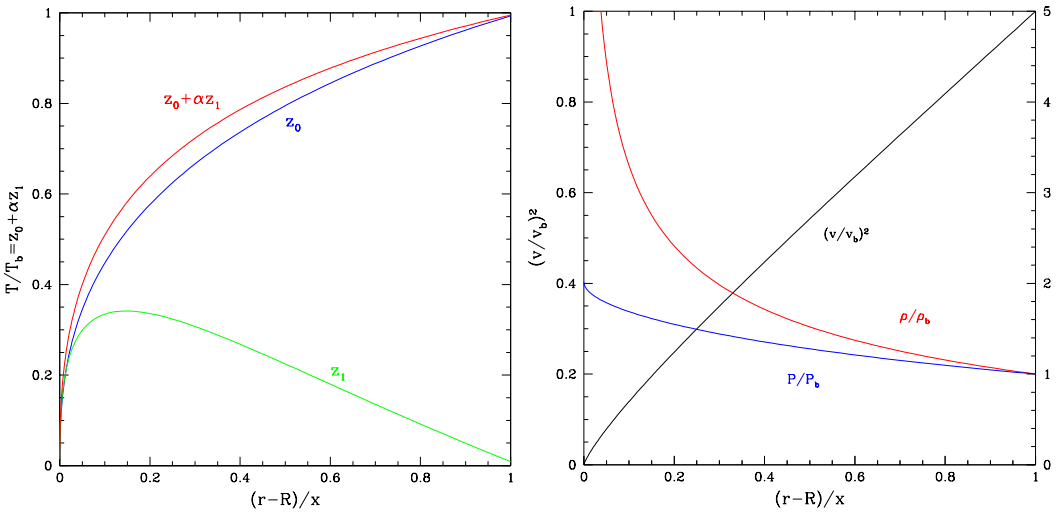


FIGURE 2.1: *Left:* Temperature distribution in the emission region. In the ordinate are plotted $T/T_b = z$, its zeroth-order approximation $z_0$ and its correction $z_1$, where $z = z_0 + \alpha z_1$. The abscisa is the height from the WD surface $r - R$ divided by the thickness $x$ of the region. *Right:* Square of velocity, density and pressure distributions in the emission region. All quantities are normalized to the values at the shock surface. (Figure, *left* and *right*, adapted from Aizu (1973)).

The relative energy spectrum $P_0(r, E)$ is given by:

$$P_0(r, E) = (9\sqrt{3}/16)(x/kT_b x_b)y^{-5/2}(4 - y)^{-1/2}\exp(-\beta/z_0) \tag{2.24}$$

where $\beta = E/kT_b$.

If the thickness of the emission region is small compared with the stellar radius, the X-ray luminosity is given by the gravitational energy gained by the gas falling on to the shock front.

Based on Equation (2.24) it is possible to examine which part of the region contributes most to the emission at a given X-ray energy. Figure 2.2 shows the results of Equation (2.24) for $\beta = \varepsilon/kT_b = 2, 1$ and $0.25$,[2] respectively.

From Figure 2.2 it is posible conclude that at $E \sim 2$ keV the contribution from the region close to the surface is very large, while at $E = 15$ keV the upper emission region makes a dominant contribution.

[2]For a white dwarfs of mass $M_{WD} = 0.29M_\odot$.

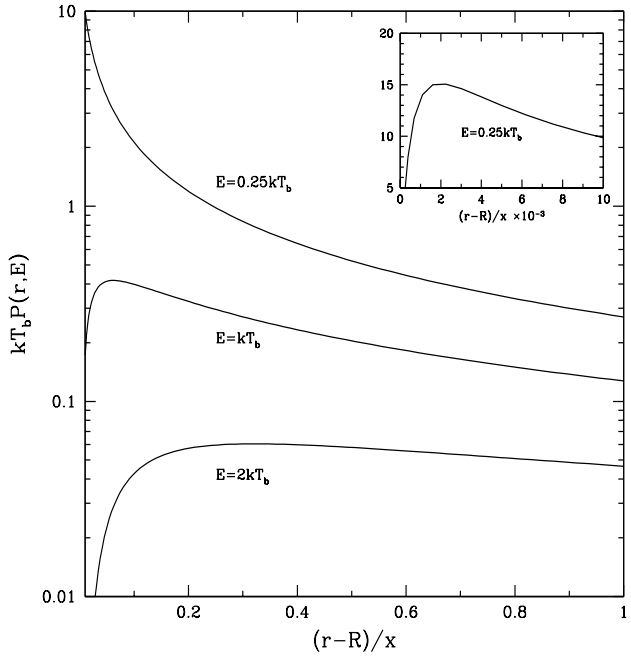


FIGURE 2.2: Distribution of emissivity spectrum in the emission region. Three cases of $\beta$ are shown. The inner panel is a magnified, in abscissa, figure of the upper part ($\varepsilon = 0.25kT_b$). (Figure adapted from Aizu (1973)).

### 2.1.2 Frank, King & Raine Model

Frank, King, & Raine (2002)[3] considered the accretion column (see Figure 2.3) problem for white dwarfs and derived a simple numerical model for the post-shock region.
It's known from spherical acccretion, that accreting matter is expected to be highly supersonic and essentially in free-fall above the polecaps. Since, in order to accrete, the infalling material must be decelerated to subsonic velocities and it is expected that some sort of strong shock to occur in the accretion stream.
The temperature at the base of the column can be given as

$$T_b = \left( \frac{L_{acc}}{4\pi R^2 f \sigma} \right)^{1/4} \tag{2.25}$$

and the gas pressure at the base of the column by

$$P_b = \frac{\rho_b k T_b}{\mu m_H} \tag{2.26}$$

which is of the same order as the ram pressure of the infalling material:

$$P_{ram} = \rho v^2 \tag{2.27}$$

where $\rho_b$ is the density at temperature $T_b$ in the envelope, while $\rho$ is the density in the

[3]Frank, King, & Raine (2002) corresponds to the 3rd Edition of the book *Accretion power in Astrophysics*. First Edition is cited as Frank, King, & Raine (1992).

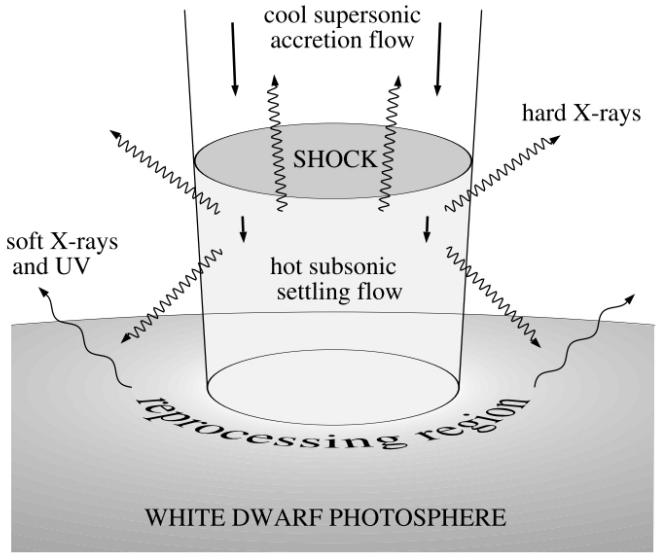


FIGURE 2.3: Accretion column geometry for a magnetized white dwarf. Accreting plasma is assumed circular and uniform across the column. (Frank, King, & Raine (2002)).

stream just about the region where stopping occurs, i.e. where the gas velocity is equal to $v = (2GM/R)^{1/2}$.
From Equation (2.26) it is possible to find the density $\rho_b$ in the region where stopping occurs

$$\rho_b = \frac{\mu m_H}{kT_b} P_{ram} \tag{2.28}$$

The aim is try to characterize the structure of this region by 'switching on' an accretion stream and following the development of the shock and associated cooling mechanisms by using the gas dynamics equations. In order to construct an accretion column model it is necessary specify how the shock-heated material cools. In principle, inserting this into the energy equation, its possible to obtain the density, temperature, velocity, etc. in the post-shock gas.

Frank, King, & Raine (2002) considered the case where the accretion column is steady, one-fluid and one-dimensional plasma flow with accretion rate $\dot{M} \gtrsim 10^{16}\mathrm{g\ s^{-1}}$ along a magnetic channel of uniform cross-section with constant gravitational acceleration $g = GM/R^2$, free-free losses and electron conduction. The assumption $g = \mathrm{constant}$ is equivalent to assuming a shock heigh, $D$, much smaller than the white dwarf radius, $R$. They also assumed that the cooling is purely radiative and the emission is dominated by thermal bremsstrahlung.
Under these assumptions, and considering $z$ the vertical coordinate, the equations of mass, momentum and energy conservation can be written as follows

$\rho v = constant$

$$\rho v\frac{dv}{dz}+\frac{d}{dz}\left(\frac{\rho kT}{\mu m_H}\right)+g\rho=0 \tag{2.29}$$

$$\frac{d}{dz}\left[\rho v\left(\frac{3kT}{\mu m_H}+\frac{v^2}{2}+gz\right)+\frac{\rho vkT}{\mu m_H}\right]=-a\rho^2T^{1/2}$$

Here, the ideal gas law has been used

$$P=\frac{\rho kT}{\mu m_H} \tag{2.30}$$

and the bremsstrahlung emission has been written as

$$4\pi j_{br}=a\rho^2T^{1/2} \tag{2.31}$$

Using $\rho v=\text{constant}$ in the third of Equations (2.29), it is possible substract the momentum equation and obtain a simplified energy equation

$$\frac{3}{2}v\frac{dT}{dz}+T\frac{dv}{dz}=-\frac{a\mu m_H}{k}\rho T^{1/2} \tag{2.32}$$

the second of Equations (2.29) can be written in the form

$$P+\rho v^2=P_{ram}+g\int_0^D\rho dz \tag{2.33}$$

where $z=0$ is the base of the column $(v\sim 0)$. Of course, at this point, the depedence of $\rho$ with $z$ is still unknown and its not possible perform the integration on the right hand side which represents the effect of the weight of cooling gas in the column.
Because the velocity in a strong shock drops by a factor $1/4$ across the shock and the gas is compressed by a factor 4, inmediately behind the shock, the jump conditions are:

$$v^2=\frac{1}{4}v_1 \qquad \text{and} \qquad \rho_2=4\rho_1 \tag{2.34}$$

shows that the gas pressure $P$ is three-quarters of the ram pressure $P_{ram}$ (Equation (2.28)). Neglecting the integral part then, $P$ reaches the value $P_{ram}$ at $z=0$. Thus $P$ varies only by a factor $\frac{4}{3}$ in the region of interest then, this suggest that

$$P=\text{constant}=P_{ram} \tag{2.35}$$

Being $P$ constant from gas ideal law we can deduce that $\rho T$ is also constant. Therefore, combining with the continuty requeriment of $\rho v=\text{constant}$, we obtained:

$$\frac{v}{v_2}=\frac{T}{T_s}=\frac{\rho_2}{\rho} \tag{2.36}$$

And using this in Equation (2.32)

$$\frac{3}{2}v\frac{dT}{dz} = \frac{\mu m_H a}{k}T_s^2\frac{\rho_2}{(-v_2)} \tag{2.37}$$

So that

$$T^{5/2} = \frac{\mu m_H a}{k}\frac{\rho_2 T_s^2}{(-v^2)}z + \text{constant} \tag{2.38}$$

At the base of the column, $(z = 0)$, it is expected that $v \sim 0$, so $T \sim 0$ and the constant must be very small.
Finally it is obtained that

$$\frac{T}{T_s} = \left(\frac{z}{D}\right)^{2/5} \tag{2.39}$$

where

$$D = \frac{kT_s^{1/2}(-v)}{\mu m_H a \rho_2}$$

Using the definition of $a$ and $D_{rad} \sim -v_2 t_{rad}$ it is easy to see that $D \sim \frac{1}{3}D_{rad}$.

The structure found is shown in Figure 2.4.

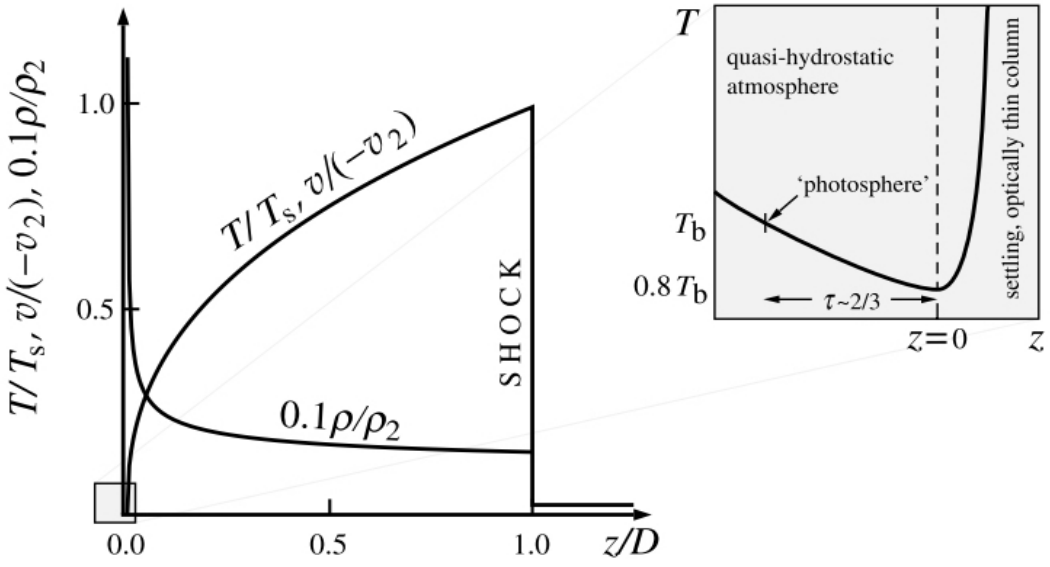


FIGURE 2.4: *Left:* Radiative accretion column. *Right:* the base of the column near $z = 0$, showing how the column solutions matches to a quasi-hydrostatic atmosphere solution having affective temperature $T_b$ at the point where $T = 0.8T_b$. (Image from Frank, King, & Raine (2002)).

It is necessary to check the self-consistency of the assumptions made deriving this solution. Frank, King, & Raine (2002) neglected the weight term $g\int_0^D \rho dz$ in the integral of the momentum equation by comparison with the ram pressure term. From Equation (2.36) and Equation (2.39):

$$g\int_0^D \frac{\rho dz}{P_{ram}} = \frac{5}{3}\left(\frac{GM}{R^2}\right)\rho^2\frac{D}{4\rho^2 v_{ff}^2} = \frac{5}{12}\left(\frac{D}{R}\right) \tag{2.40}$$

The term $\rho v^2$ is neglected by comparison with $P \cong P_{ram}$, obtaining finally

$$\frac{\rho v^2}{P_{ram}} \sim \rho v_2^2 \left(\frac{z}{D}\right)^{2/5} /(4\rho_2 v_2^2) = \frac{1}{4}\left(\frac{z}{D}\right)^{2/5} < 1 \tag{2.41}$$

## 2.2 A Numerical Model

With the aim of studying the structure of the emission region onto accreting white dwarfs (the temperature, density, pressure and gas velocity distributions) and to calculate the X-ray spectrum of the thermal bremsstrahlung from this region. An accretion column structure model is presented in order to compare the X-ray spectrum obtained with the observed spectra.

### 2.2.1 Numerical Method and boundary conditions

#### Basic equations

Given a 1-dimensional cylindrical accretion column, or post-shock region (PSR) the heated matter settles down to the WD surface in the subsonic regime and loses energy by optically thin bremsstrahlung. Following the method of Frank, King, & Raine (1992), Cropper et al. (1999) and Suleimanov, Revnivtsev, & Ritter (2005), the accretion flow can be fully described using the following set of hydrodynamical equations, with the mass continuity equation given by

$$\frac{d}{dz}(\rho v) = 0 \tag{2.42}$$

where $z$ is the spatial coordinate shown in Figure 2.5 whose origin is the WD centre, $\rho$ is the density and $v$ the flow velocity.
The momentum equation is

$$\frac{d}{dz}(\rho v^2 + P) = -\frac{GM_{WD}}{z^2}\rho \tag{2.43}$$

and the energy equation

$$v\frac{dP}{dz} + \gamma P\frac{dv}{dz} = -(\gamma - 1)\Lambda \tag{2.44}$$

These equations must be supplemented by the ideal-gas law (Equation (2.30)).

Here $T$ is the temperature, $P$ is the thermal pressure of the plasma, $\gamma$ the adiabatic index ($\gamma = 5/3$), $\mu$ the mean molecular weight of a fully ionized plasma with the solar abundance, $m_H$ is the mass of a hydrogen atom and $G$ is the constant of gravitation.

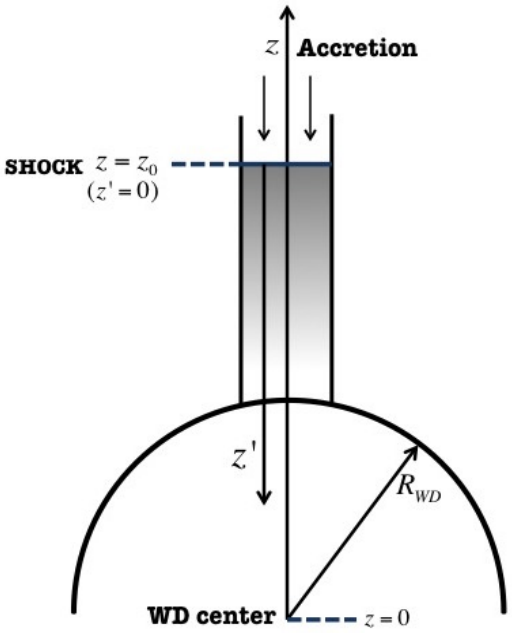


FIGURE 2.5: Geometry of the post-shock region model.

The cooling rate $\Lambda$ due to thermal optically thin radiation is given by

$$\Lambda = \left(\frac{\rho}{\mu m_H}\right)^2 \Lambda_N(T) \tag{2.45}$$

where $\Lambda_N(T)$ is the cooling function. In this work $\Lambda_N(T)$ has been taken for solar chemical composition as calculated and tabulated by Sutherland & Dopita (1993) (hereafter, refered as **"cooling Sutherland & Dopita"**).
Besides this cooling function, it has been also adopted the expression of total bremsstrahlung emission from Zombeck (1982) (hereafter, refered as **"cooling Zombeck"**).

$$\Lambda = 1.4 \times 10^{-27} T^{1/2} n_e n_Z Z^2 g_B(T) \quad \text{erg cm}^{-3}\,\text{s}^{-1} \tag{2.46}$$

Since the contributions of all ions is $\sum n_e n_Z Z^2 \approx 1.4 n_e^2$ and $g_B(T) \approx 1.2$. Then,

$$\Lambda = 2.4 \times 10^{-27} T^{1/2} n_e^2 \quad \text{erg cm}^{-3}\,\text{s}^{-1} \tag{2.47}$$

given that $\Lambda_N(T) = 2.4 \times 10^{-27} T^{1/2}$, finally

$$\Lambda = \Lambda_N(T) n_e^2 \tag{2.48}$$

where

$$n_e = \frac{\rho}{\mu_e m_H} \tag{2.49}$$

is the electron number density.

The integral of the mass continuity equation (Equation (2.42)) is

$$\rho v = a \tag{2.50}$$

where $a$[4] is the local mass accretion rate at the WD surface $[a] = \mathrm{g\ s^{-1}\ cm^{-2}}$. Using this integral, it is possible to replace $\rho$ in the Equations (2.43) and (2.44) by $a/v$ and with the substitution $z' = z_0 - z$ ($z_0$: shock coordinate) finally obtain

$$\frac{dv}{dz'} = g(z')\frac{1}{v} - \frac{1}{a}\frac{dP}{dz'} \tag{2.51}$$

$$\frac{dP}{dz'} = \frac{(\gamma-1)\Lambda a + g(z')\gamma P a/v}{\gamma P - av} \tag{2.52}$$

where

$$g(z') = \frac{GM_{WD}}{(z_0 - z')^2} \tag{2.53}$$

**Method of solution**

Equations (2.51) and (2.52) can be solved with the appropriate boundary conditions. As it is commonly accepted the suggestion about a strong adiabatic shock at the top of the post-shock region ($z = z_0$), the equations are solved from the top of the post-shock accretion region $z = z_0(z' = 0)$, to white dwarf surface, $z = R_{WD}(z' = z_0 - R_{WD})$, with the following boundary conditions

$$v_0 = 0.25\sqrt{2GM_{WD}/z_0} \tag{2.54}$$

$$\rho_0 = \frac{a}{v_0} \tag{2.55}$$

$$P_0 = 3av_0 \tag{2.56}$$

$$T_0 = 3\frac{\mu m_H}{k}v_0^2 \tag{2.57}$$

and soft landing

$$v = 0 \tag{2.58}$$

at the white dwarf surface ($z = 0$).

[4] $4\pi r^2 \rho v = \dot{M}$

The white dwarf radius is calculated from the Nauenberg (1972) white dwarf mass-radius relation

$$R_{WD} = 7.8 \times 10^8 \mathrm{cm} \left[ \left( \frac{1.44 M_\odot}{M_{WD}} \right)^{2/3} - \left( \frac{M_{WD}}{1.44 M_\odot} \right)^{2/3} \right]^{1/2} \tag{2.59}$$

The boundary conditions are uniquely given by specifying $M_{WD}$, $a$ and $z_0$[5], which is the distance from the shock front to the white dwarf surface (i.e. the shock height). Of them, the shock position $z_0$ matching the boundary conditions is found by iteration using shooting method.

In the numerical code, the application of the shooting method exactly implements multi-dimensional globally convergent Newton-Raphson method, which performs the numerical integration using the quality-controlled Runge-Kutta method (see Appendix B for details).

### Spectra computations

The post-shock region models are optically thin and the relative spectra can be calculated by integrating the local bremsstrahlung emissivity over the height $z$

$$F_E = \int_{R_{WD}}^{z_0} j(z) dz \tag{2.60}$$

where the local emissivity is taken in the following form (Zombeck, 1982):

$$j(z) = 9.52 \times 10^{-38} \left( \frac{\rho(z)}{\mu m_H} \right)^2 T^{-1/2}(z) \left( \frac{E}{kT(z)} \right)^{-0.4} \times \exp\left( \frac{-E}{kT(z)} \right) \mathrm{erg\ cm^{-3}\ s^{-1}} \tag{2.61}$$

With the aim to study the structure of the emission region and determine the mass of white dwarfs and elucidate the magnetic character of the cataclysmic variable, the spectra obtained are provided in a single FITS[6] file suitable for the analysis of X-ray observations in XSPEC (Arnaud (1996)). For details see Section § 3.3.2.

[5] Vector with initial values of $z_0$ to narrow the shock position or shock height. Because, results depends slightly on the choice of the starting point.

[6] Flexible Image Transport System format

# 3

# STRUCTURE OF THE EMISSION REGION

The hydrodynamic calculations presented in previous chapter predict the behaviour of temperature, density, velocity, and pressure in the emission region. By comparing these predictions with the continuum of the observed X-ray spectra important parameters of the system, such as the white dwarf mass, can be constrained (e.g., Ishida (1991); Cropper, Ramsay, & Wu (1998); Beardmore, Osborne, & Hellier (2000); Ramsay (2000)).

The new model presented in Section § 2.2 is differentiated from other models (e.g Cropper et al. (1999); Suleimanov, Revnivtsev, & Ritter (2005)) mainly on the following three points: (1) the cooling function, (2) the assumed initial value of the shock height, and (3) the local mass accretion rate.

In the case of the cooling function, the approximation of Zombeck (1982) has been used because it is a simple way to obtain the total emission bremsstrahlung. Also, for comparison, the computed cooling of Sutherland & Dopita (1993) is adopted since it is one of the most used in different works (e.g. Suleimanov, Revnivtsev, & Ritter (2005); Brunschweiger et al. (2009); Yuasa et al. (2010)). Given that the results to solve the Equations (2.51) and (2.52) through the shooting method depends on the choice of the starting point, a vector with initial values of $z_0$ is selected with the aim to improve the calculation of the shock position. A local mass accretion rate of $a = 1\ \mathrm{g\ cm^{-2}\ s^{-1}}$, corresponding to an accreation rate of $\dot{M} = 1.2 \times 10^{-7}\ \mathrm{M_\odot/yr}$ for a white dwarf with mass of $M_{WD} = 0.7\ \mathrm{M_\odot}$, is typically used (e.g., Suleimanov, Revnivtsev, & Ritter, 2005). However, in this case the accreton rate is taken as $\dot{M} = 4.3 \times 10^{-8}\ \mathrm{M_\odot/yr}$.

## 3.1 Cooling function

Close to the white dwarf surface the infalling matter produce a strong shock where the gas is heated up to temperatures of $\sim 10-40$ keV. The post shock flow becomes subsonic and cools via thermal bremsstrahlung and cyclotron radiation.
The cooling mechanism has been the subject of many theoretical studies (e.g., Aizu (1973); Cropper et al. (1999); Canalle et al. (2005); Hayashi & Ishida (2014a)). When the accretion rate of the system is high, $\gtrsim 10^{16}$ g s$^{-1}$, and the white dwarf magnetic field is weak, $B \sim 1$ MG, bremsstrahlung cooling usually dominates. If the accretion rate is low, $\lesssim 10^{16}$ g s$^{-1}$, and the magnetic field is strong, $B \gtrsim 10$ MG, then cyclotron cooling is the dominant process, at least near the shock (Lamb & Masters (1979); King & Lasota (1979)). It is straightforward to calculate the post shock accretion flow with only optically thin bremsstrahlung cooling (see e.g., Aizu (1973); Chevalier & Imamura (1982)). The inclusion of cyclotron cooling complicates the calculations because of large opacity effects (Woelk, U. and Beuermann (1996), Cropper, Ramsay, & Wu (1998), Cropper et al. (1999)). An exact treatment of cyclotron cooling requires to solve the radiative transfer and hydrodynamic equations simultaneously. This means that is unlikely to find a simply analytic solution. However, assuming a relatively high local mass accretion rate, $> 1$ g cm$^{-2}$s$^{-1}$, it is possible to ignore cyclotron cooling since it is not important in such conditions (Suleimanov et al., 2016).

Therefore, the cooling rate $\Lambda$ due to thermal optically thin radiation is given by:

$$\Lambda = n_e^2 \Lambda_N(T) \tag{3.1}$$

where the cooling function $\Lambda_N$ is given by Zombeck (1982) (cooling Zombeck) in the form:

$$\Lambda_N(T) = 2.4 \times 10^{-27} T^{1/2} \tag{3.2}$$

Alternatively, the cooling function derived by Sutherland & Dopita (1993) (cooling Sutherland & Dopita) from tabulated values of $\Lambda_N$ as a function of $T$, and derived for a solar chemical composition is used in the form:

$$\Lambda = \left(\frac{\rho}{\mu m_H}\right)^2 \Lambda_N(T) \tag{3.3}$$

In this work both cooling functions are used. Figure 3.1 shows the comparison between the cooling function of Zombeck and cooling Sutherland & Dopita, for temperatures from $log(T) = 4.0$ to $8.5$ K and for a mass $M_{WD} = 0.8$ M$_\odot$ and accretion rate $\dot{M} = 4.3 \times 10^{-8}$ M$_\odot$/yr.

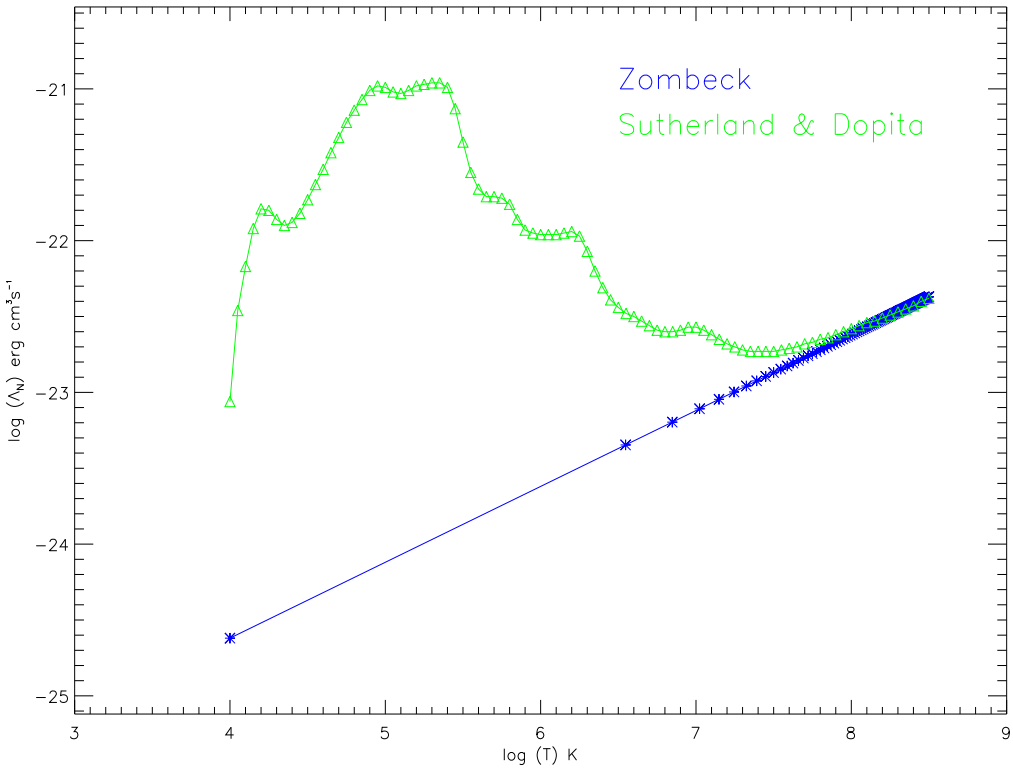


FIGURE 3.1: Normalized cooling functions for solar metallicity and temperatures between $log(T) = (4.0 - 8.5)$ K. *blue line* corresponds to cooling Zombeck; *green line* to cooling Sutherland & Dopita.

## 3.2 Distribution of the physical quantities in the emission region

The flux emitted in the shock region depends on the temperature ($T$) and density ($\rho$). These magnitudes, and the related pressure ($P$) and velocity ($v$), change with the distance from the shock position, $z = z_0$, to the white dwarf surface, $z = R_{WD}$, (see Figure 2.5). With the aim to characterize the emission region, these physical quantities are obtained for *(1)* different masses, and *(2)* different accretion rates. The obtained profiles are also compared with those derived previously by Aizu (1973) and Frank, King, & Raine (2002) (Section § 3.2.1).

Figure 3.2 and 3.3 show the run of these magnitudes as a function of the distance in the shock region $(z - R_{WD})/R_{WD}$, where $z$ is the spatial coordinate (see Figure 2.5), for a white dwarf of mass $M_{WD} = 0.8$ M$_\odot$ and accretion rate $\dot{M} = 4.3 \times 10^{-8}$ M$_\odot$/yr using the Zombeck (Equation (3.1)) and Sutherland & Dopita (1993) cooling function (Equation (3.3)), respectively.

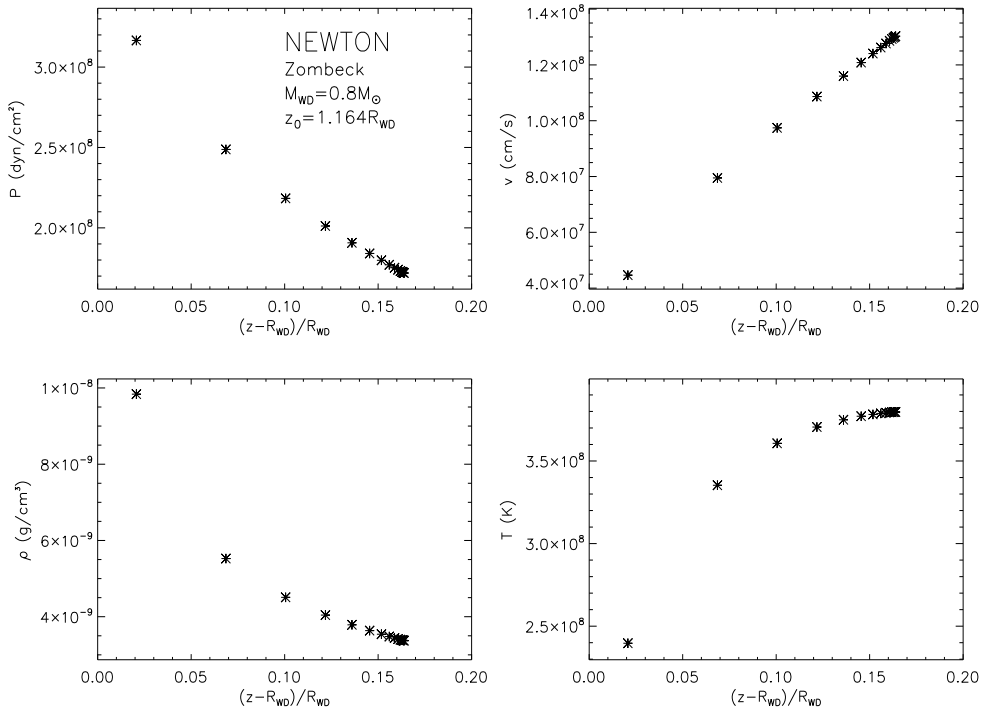


FIGURE 3.2: Pressure (*top-left*), velocity (*top-right*), density (*bottom-left*) and temperature (*bottom-rigth*) profiles with bremsstrahlung cooling approximation of Zombeck (1982).

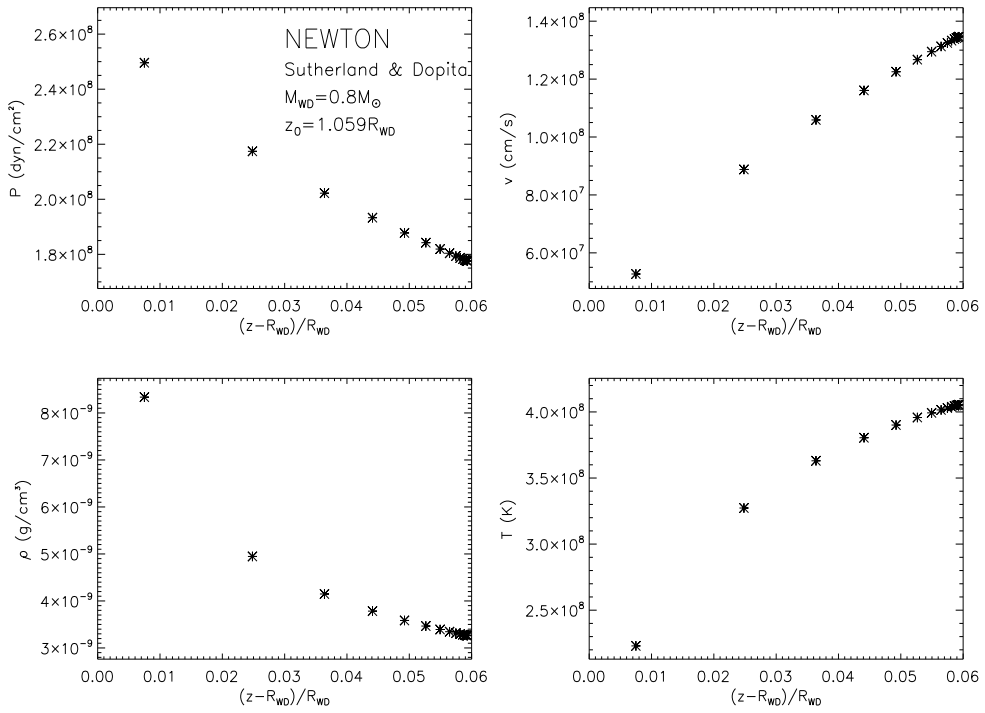


FIGURE 3.3: As Figure 3.2, using the results of the cooling function obtained by Sutherland & Dopita (1993).

In both cases, Figures 3.2 and 3.3, the velocity is close to zero in the white dwarf surface increasing from there off. It reachs the largest value in the position of the shock. Likewise the temperature reach its maximun at the shock. On the contrary, the density decreases as we move away of the white dwarf surface as well as the pressure.

Table 3.1 summarizes the principal parameters of the post shock region for cooling Zombeck and cooling Sutherland & Dopita, respectively.

TABLE 3.1: Estimation of principal physical quantities of the emission region with cooling Zombeck and Sutherland & Dopita for $M_{WD} = 0.8\ \mathrm{M}_{\odot}$ and $\dot{M} = 4.3 \times 10^{-8}\ \mathrm{M}_{\odot}/\mathrm{yr}$.

| $M_{WD} = 0.8\ \mathrm{M}_{\odot}$ | | |
|---|---|---|
| **Parameter** | **Zombeck** | **Sutherland & Dopita** |
| Shock | $1.164\ \mathrm{R_{WD}}$ | $1.059\ \mathrm{R_{WD}}$ |
| $T_{min}$ | $\sim 2.4 \times 10^{8}$ | $\sim 2.3 \times 10^{8}$ |
| $T_{max}$ | $\sim 3.8 \times 10^{8}$ | $\sim 4.0 \times 10^{8}$ |
| $\rho_{min}$ | $\sim 3.4 \times 10^{-9}$ | $\sim 3.3 \times 10^{-9}$ |
| $\rho_{max}$ | $\sim 9.8 \times 10^{-9}$ | $\sim 8.3 \times 10^{-9}$ |

Figure 3.4 shows the direct comparison of the temperature, density, velocity and pressure profiles of the post shock region obtained using both the Zombeck and Sutherland & Dopita cooling functions. In the same way, Figure 3.5 shows the normalized temperature and density profiles in both cases.

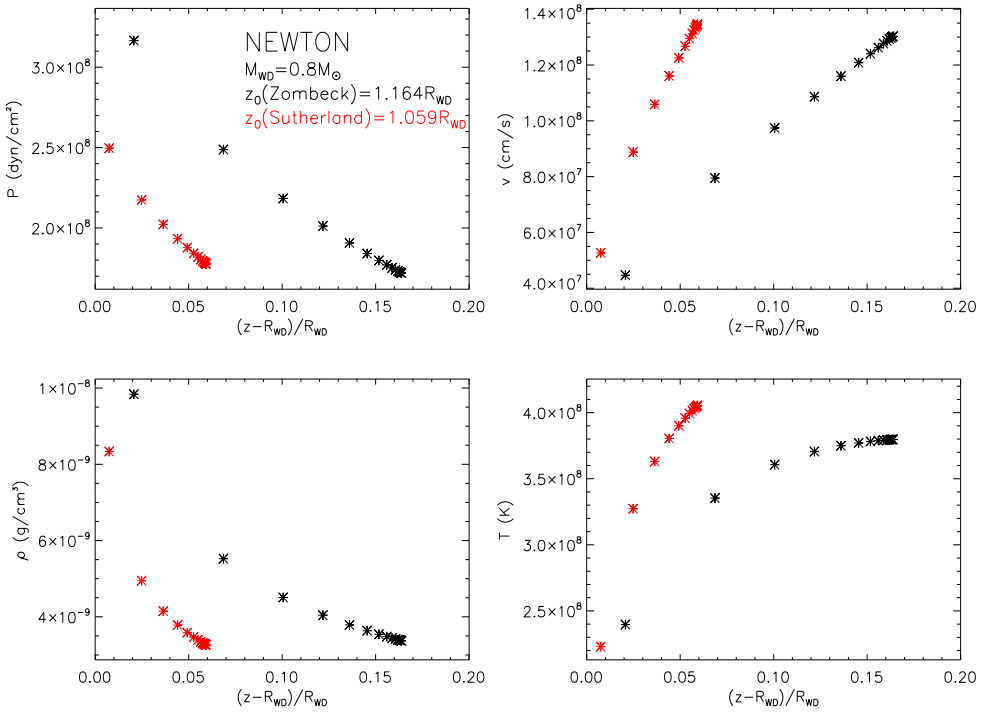


FIGURE 3.4: Comparison profiles for: pressure (*top-left*), velocity (*top-right*), density (*bottom-left*) and temperature (*bottom-rigth*) with pure bremsstrahlung cooling with *(black)* cooling functions of Zombeck and *(red)* Sutherland & Dopita.

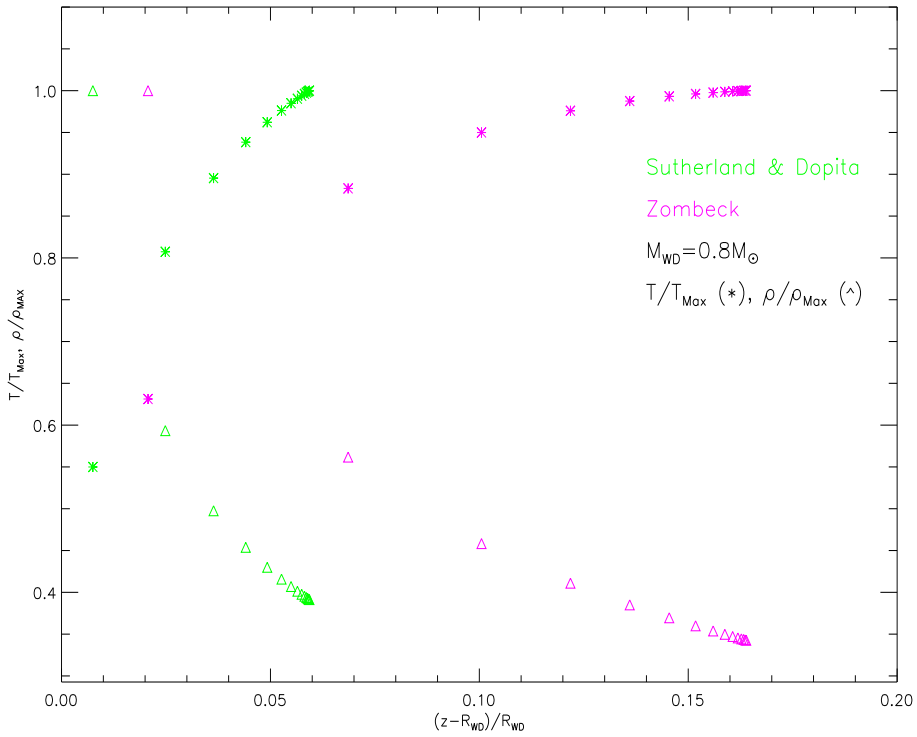


FIGURE 3.5: Comparison temperature (*asterisk*) and density (*triangles*) profiles for cooling Zombeck (*magenta*) and cooling Sutherland & Dopita (*green*).

From Figures 3.4 and 3.5 it is possible to appreciate that there are not major differences in the minimun and maximun values for the different physical quantities. Neverthless the main difference between both coolings is the determination of the shock height. The shock position calculated with cooling Zombeck is greater than the obtained from cooling Sutherland & Dopita. The implications of the shock height in the calculated spectrum is treated in detail in subsequent Sections (e.g. Section § 3.3).

### Influence of mass

It is also interesting to investigate how these profiles change as a function of the white dwarf mass. The local mass accretion rate, $a$, as a function of mass that have been used are listed in Table 3.2.

TABLE 3.2: Local mass accretion rate per unit area, $a$, for different masses of white dwarfs and $\dot{M} = 4.3 \times 10^{-8}\ \mathrm{M}_{\odot}/\mathrm{yr}$.

| $\dot{M} = 4.3 \times 10^{-8}\ \mathrm{M}_{\odot}/\mathrm{yr}$ | |
|---|---|
| $M_{WD}\ (\mathrm{M}_{\odot})$ | $a\ (\mathrm{gr\,cm^{-2}\,s^{-1}})$ |
| 0.6 | $2.86000 \times 10^{-1}$ |
| 0.8 | $4.39250 \times 10^{-1}$ |
| 1.0 | $7.19204 \times 10^{-1}$ |
| 1.2 | 1.44905 |

In Figures 3.6 and 3.7 the temperature, density, velocity, and presure profiles have been plotted for four different white dwarf masses: $M_{WD} = (0.6,\ 0.8,\ 1.0 \text{ and } 1.2)\mathrm{M}_{\odot}$, with $\dot{M} = 4.3 \times 10^{-8}\ \mathrm{M}_{\odot}/\mathrm{yr}$ using cooling Zombeck and cooling Sutherland & Dopita, respectively.

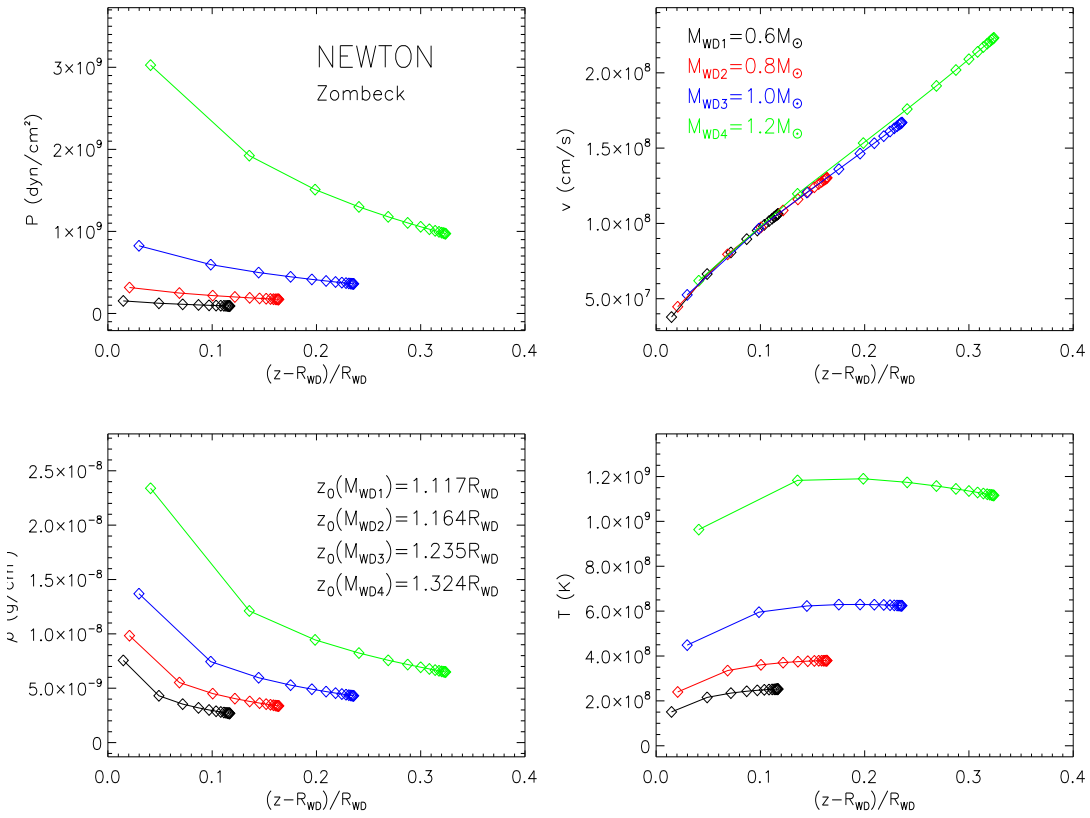


FIGURE 3.6: Pressure (*top-left*), velocity (*top-right*), density (*bottom-left*) and temperature (*bottom-rigth*) profiles with bremsstrahlung cooling approximation of Zombeck for four different white dwarf masses: *black:* 0.6 $\mathrm{M}_{\odot}$, *red:* 0.8 $\mathrm{M}_{\odot}$, *blue:* 1.0 $\mathrm{M}_{\odot}$ and *green:* 1.2 $\mathrm{M}_{\odot}$.

As mass increase, pressure, density and temperature also increases and by the boundary condition $v = 0$, the velocity profiles have approximately the same minimum value. Close to the shock point the velocity get its maximun and get larger as mass increase. The main difference observed in the profiles from Figures 3.6 and 3.7 is the shock height and will be discussed in detail later.

In order to determine how the shock height varies according to the mass of the white dwarf, Yuasa et al. (2010) calculated the shock temperature and height for different masses. Figure 3.8 shows the dependency of the shock height and the shock temperature on the white dwarf mass by interpolating data points with spline functions. For higher white dwarf masses, the gas velocity at the shock height becomes higher, and therefore the gas density falls for a given accretion rate. This causes a decrease in the plasma cooling rate and cooling time, yielding higher shock heights.

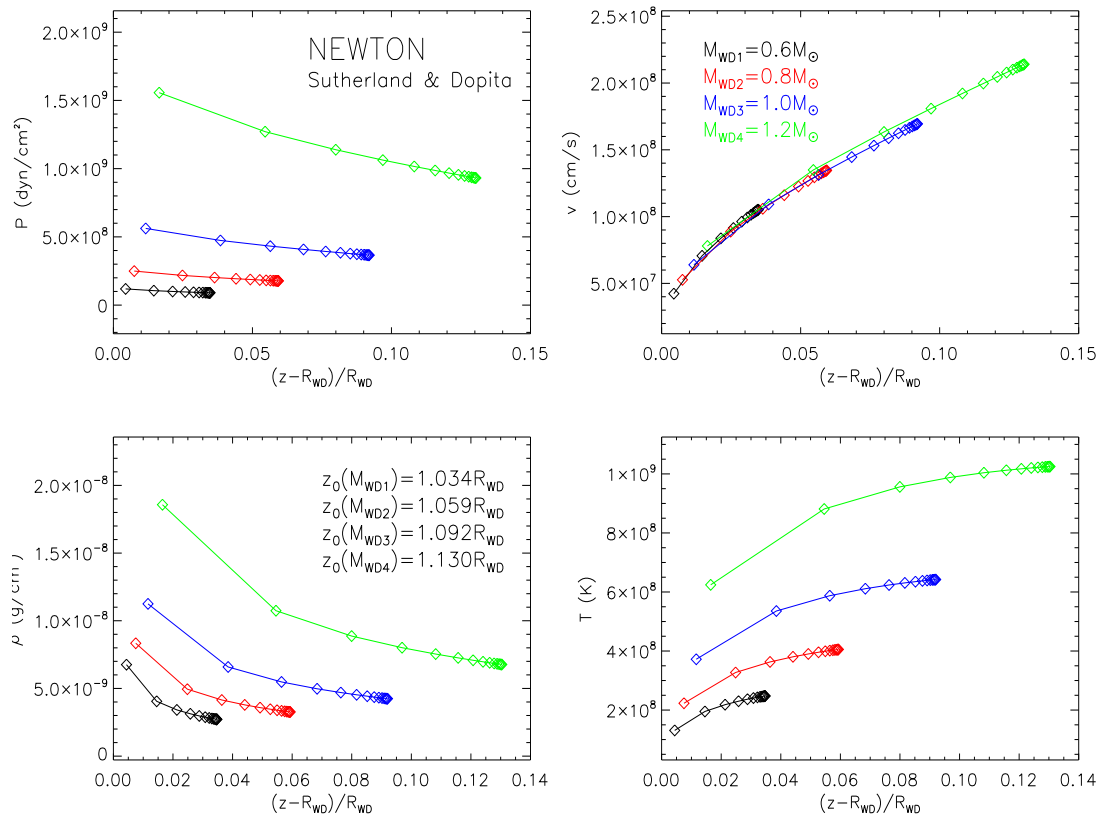


FIGURE 3.7: As Figure 3.6, using the results of the cooling function obtained by Sutherland & Dopita (1993).

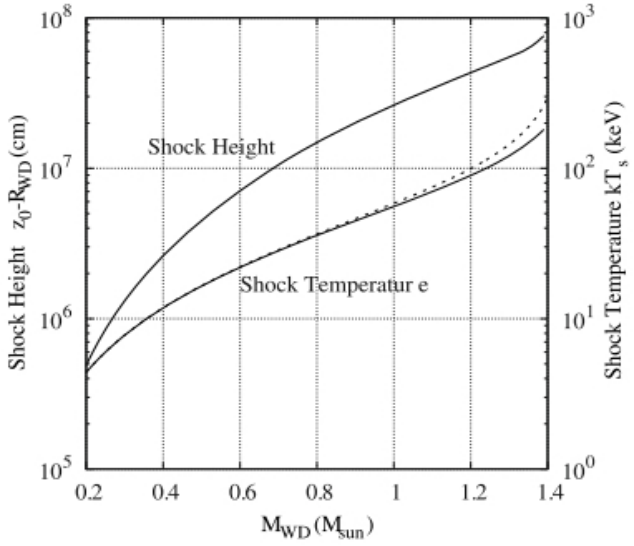


FIGURE 3.8: Results of the numerical solutions of Yuasa et al. (2010) for the shock height from the white dwarf surface *(thick solid line)* and the shock temperature *(thin solid line)*, shown against the white dwarf mass. For comparison, the dashed line shows the shock temperature calculated by assuming no-gravity in the post shock region. (Image from Yuasa et al. (2010)).

Figure 3.9 shows the behaviour of shock height, $z_0$, as a function of the white dwarf mass, for both cooling functions assuming an accretion rate of $\dot{M} = 4.3 \times 10^{-8}\ \mathrm{M}_{\odot}/\mathrm{yr}$ using the model presented here.

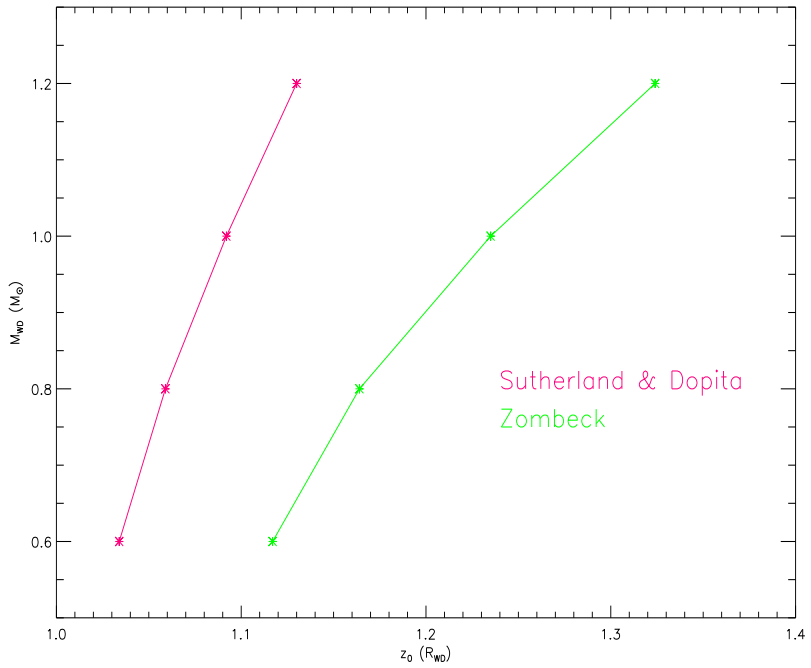


FIGURE 3.9: White dwarf masses as a function of the shock height, $z_0$ in units of $\mathrm{R_{WD}}$. (*Magenta*) points corresponds to cooling Sutherland & Dopita; (*green*) points corresponds to cooling Zombeck.

Like Yuasa et al. (2010), from Figure 3.9 it is possible appreciate that the flow velocity and temperature decrease with the height and with the white dwarf mass; values of velocity and temperature at $z_0$ (shock) are largest for more massive white dwarfs. But the density and pressure increases when the height decreases. However, its values also increases for larger masses.

Also, there is a clear difference in the shock heights calculated with each cooling function, being the values obtained with cooling Zombeck greater than those of cooling Sutherland & Dopita. Moreover, this diference increases with white dwarf mass.

#### Influence of the accretion rate

The local mass accretion rate, $a$, can be related to the total accretion rate $\dot{M}$ via $\dot{M} = 4\pi R_{WD}^2 a f$, where $f$ is a fraction of the post shock region cross section to the white dwarf surface area. Since $a$ significantly affects the structure of the post shock region, some authors (e.g. Yuasa et al. (2010); Hayashi & Ishida (2014a)) have investigated the dependence of the local mass accretion rate in the calculation of the properties of the post shock region.

Figure 3.10 shows the result of the numerical solutions performed by Yuasa et al. (2010) it shows that a lower value of $a$ gives a lower shock temperature at any mass of white dwarf. But for higher mass, difference of the resulting shock temperatures is more or less conspicuous.

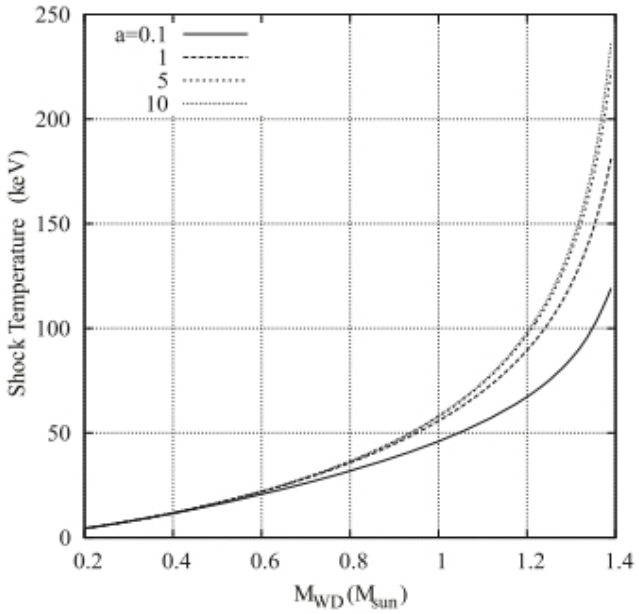


FIGURE 3.10: Results of the numerical solutions of Yuasa et al. (2010) of the post shock region model when changing the accretion rate. Shock temperatures are plotted with solid, long dashed, short dashed, and dotted lines for accretion rates of $a = (0.1,\ 1.0,\ 5.0 \text{ and } 10)\ \mathrm{g\ cm^{-2}s^{-1}}$. (Image from Yuasa et al. (2010)).

For example, for a white dwarf mass of $0.8\ \mathrm{M_\odot}$, Yuasa et al. (2010) appreciate a difference of a factor of $1.13$ between the results obtained for $a = 0.1\ \mathrm{g\ cm^{-2}s^{-1}}$ and $a = 1.0\ \mathrm{g\ cm^{-2}s^{-1}}$. In the same way, a factor of $1.02$ between $a = 1.0\ \mathrm{g\ cm^{-2}s^{-1}}$ and $a = 10\ \mathrm{g\ cm^{-2}\ s^{-1}}$. While for a mass of $M_{WD} = 1.2\ \mathrm{M_\odot}$, the difference increases to factors of $1.33$ and $1.10$; this means that the estimated white dwarf mass is affected by less than $\sim 30\%$ in the range $a = (0.1 - 10)\mathrm{g\ cm^{-2}s^{-1}}$ for a white dwarf less massive than $1.2\ \mathrm{M_\odot}$ where most white dwarfs are likely to belong. However, some observations suggest that the local mass accretion rate distributes in a wider range.

Meanwhile, Hayashi & Ishida (2014a) modelled the post shock region of Intermediate Polars with a local mass accretion rate being floated in the range between $0.0001$ and $100\ \mathrm{g\ cm^{-2}s^{-1}}$, considering cylindrical and dipolar geometry.
From Hayashi & Ishida (2014a), Figure 3.11 shows the density distributions of the cylindrical and dipolar post shock accretion columns with the local mass accretion rate of $0.0001$, $0.01$, $1$ and $100\ \mathrm{g\ cm^{-2}s^{-1}}$ in the case of $M_{WD} = 0.7\ \mathrm{M_\odot}$. In this figure, the right ends of each profile corresponds to the shock front. The other ends are terminated at $0.1$ per cent of a post shock accretion column height of each case. This figure implies that the post shock region becomes taller with a lower local mass accretion rate due to a longer

cooling time. When the local mass accretion rate is sufficiently high, $a \gtrsim 5\ \mathrm{g\,cm^{-2}s^{-1}}$ for a $0.7\ \mathrm{M_\odot}$ white dwarf, the density increases towards the white dwarf surface with a power-law function of the distance from the white dwarf surface. On the other hand, when the local mass accretion rate is sufficiently low, $a \gg 5\ \mathrm{g\,cm^{-2}s^{-1}}$ for the $0.7\ \mathrm{M_\odot}$ white dwarf, the density distribution deviates from the power law.

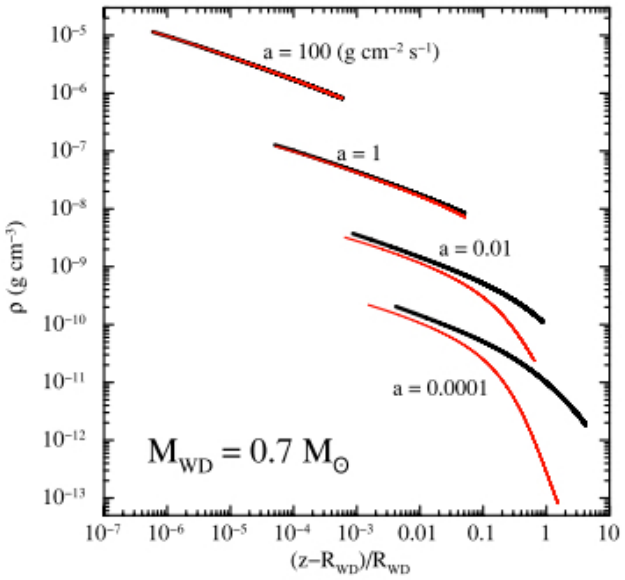


FIGURE 3.11: Density distributions of the cylindrical *(black)* and dipolar *(red)* post shock accretion colums for the white dwarf mass of $0.7\ \mathrm{M_\odot}$ and $a$ of 0.0001, 0.01, 1, $100\ \mathrm{g\,cm^{-2}s^{-1}}$, obtained from Hayashi & Ishida (2014a) model. The right ends of the distributions correspond to the tops of the post shock accretion columns. The other ends are terminated at $0.1$ per cent of the post shock accretion column height. (Image from Hayashi & Ishida (2014a))

Figure 3.12, shows a peak in the middle of the post shock accretion column at low enough local mass accretion rate. This is because energy input by gravity overcomes cooling energy loss since the low density reduces the cooling rate, and the tall post shock accretion column retains larger amount of gravitational energy to be released below the shock front. The averaged temperature of the dipolar post shock accretion column monotonically decreases as the flow descends the post shock accretion column for the $M_{WD} = 0.7\ \mathrm{M_\odot}$ throughout the range $a = (0.0001 - 100)\mathrm{g\ cm^{-2}s^{-1}}$ unlike the cylindrical case.

Relations between the height of the post shock accretion column and the local mass accretion rate are shown in Figure 3.13 for $0.4\ \mathrm{M_\odot}$, $0.7\ \mathrm{M_\odot}$ and $1.2\ \mathrm{M_\odot}$ masses. The post shock region constantly extends upwards with the lower local mass accretion rate, but the slope of the post shock accretion column height abruptly changes at a certain value of $a$. At around the high end of $a$, the height is inverse proportional to $a$, and the height of the post shock region is almost identical between the two post shock accretion column geometries.

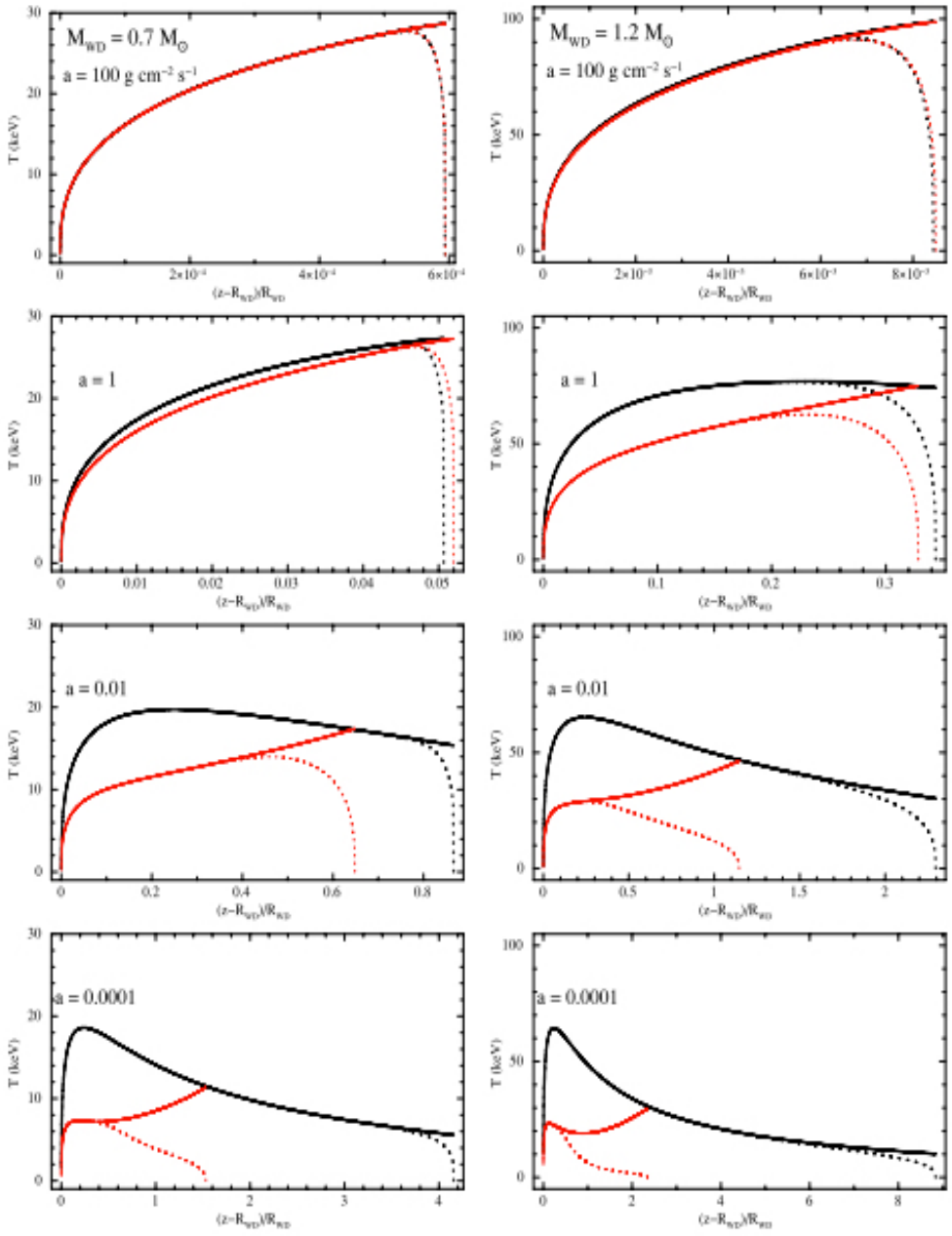


FIGURE 3.12: Averaged *(solid)* and electron *(dotted)* temperature distributions of the cylindrical *(black)* and dipolar *(red)* post shock accretion columns for the white dwarf mass of $0.7\ \mathrm{M}_{\odot}$ (left-hand columns) and $1.2\ \mathrm{M}_{\odot}$ (right-hand columns) and $a$ of $0.0001$, $0.01$, $1$, $100\ \mathrm{g\,cm^{-2}s^{-1}}$ from bottom to top panels. (Image from Hayashi & Ishida (2014a)).

The local mass accretion rate significantly affects the structure of the post shock accretion column, and there is a critical rate below which the profiles of the density and temperature distributions deviate from those of the Cropper et al. (1999) where the local mass accretion rate is fixed at $1\ \mathrm{g\,cm^{-2}s^{-1}}$). This happens when the local mass accretion rate is between $5$ and $100\ \mathrm{g\,cm^{-2}s^{-1}}$ for the $0.7\ \mathrm{M}_{\odot}$ and $1.2\ \mathrm{M}_{\odot}$ white dwarf, respectively, or the height of the post shock accretion region becomes $1$ per cent of the white dwarf radius.

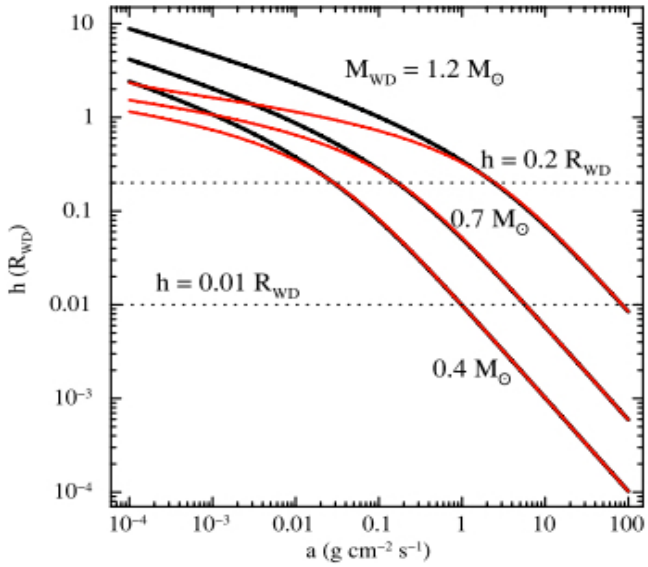


FIGURE 3.13: The post shock accretion column heights for the 0.4, 0.7 and 1.2 $M_\odot$ white dwarfs as a function of the local mass accretion rate. *Black* and *red* lines show the cylindrical and dipolar cases, respectively. The two horizontal dotted lines represent 1 and 20 per cent of the white dwarf radius. Note that the heights in this figure are normalized by each white dwarf radii. (Image from Hayashi & Ishida (2014a)).

In order to examine the dependence of the structure of the accretion rate, calculations with different accretion rates have been perfomed as shown in Figure 3.14, for cooling Zombeck, and Figure 3.15, for cooling Sutherland & Dopita. The values of local mass accretion rates adopted are presented in Table 3.3 for a white dwarf mass of 1.0 $M_\odot$.

TABLE 3.3: Values of accretion rate for a white dwarf mass $M_{WD} = 1.0\ M_\odot$.

| $M_{WD} = 1.0\ M_\odot$ | |
|---|---|
| $\dot{M}$ ( $M_\odot$/yr) | $a$ (gr $cm^{-2}$ $s^{-1}$) |
| $1.0 \times 10^{-10}$ | $1.67257 \times 10^{-3}$ |
| $1.0 \times 10^{-9}$ | $1.67257 \times 10^{-2}$ |
| $1.0 \times 10^{-8}$ | $1.67257 \times 10^{-1}$ |
| $1.0 \times 10^{-7}$ | 1.67257 |

From Figures 3.14 and 3.15 it is possible to observe that these results are in agreement with the expected results of Yuasa et al. (2010) and Hayashi & Ishida (2014a). The post shock region extends upwards with a lower $a$, i.e. the height $z_0$ is evidently proportional to $a^{-1}$.

When the local mass accretion rate is sufficiently high, the density increases towards the white dwarf surface. Moreover, the temperature, shows a peak in the middle of the post shock region (as in Hayashi & Ishida (2014a)). At low enough local mass accretion rate, the temperature increase as local mass accretion rate increase. But, for a higher local mass accretion rate, the temperature starts to decrease inward the white dwarf surface.

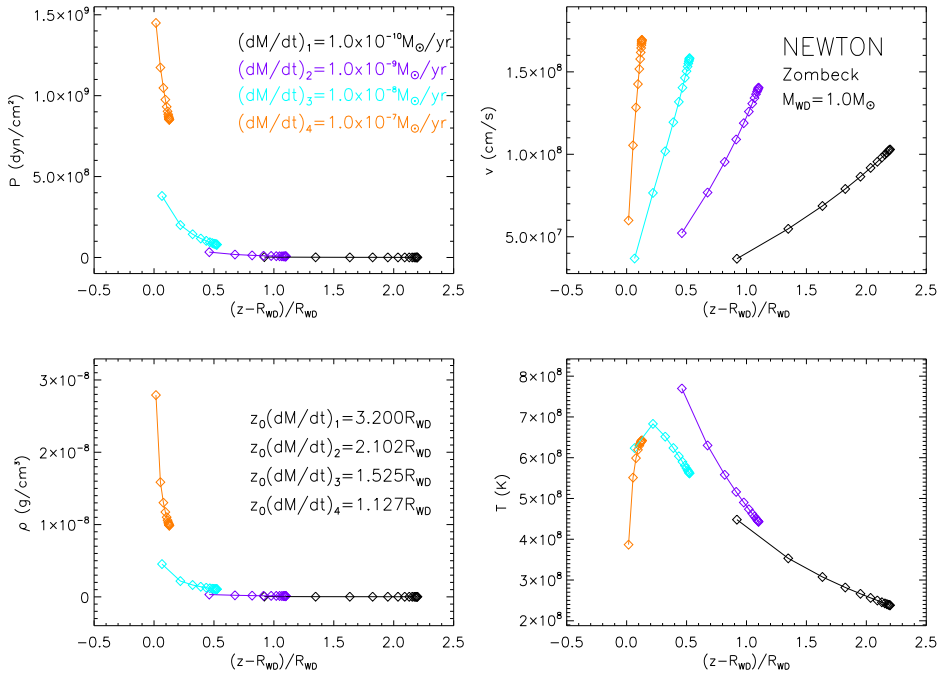


FIGURE 3.14: Pressure (*top-left*), velocity (*top-right*), density (*bottom-left*) and temperature (*bottom-rigth*) profiles with bremsstrahlung cooling approximation of Zombeck for different accretion rates: *orange:* $1.0 \times 10^{-10}$ $M_\odot$/yr, *cyan:* $1.0 \times 10^{-9}$ $M_\odot$/yr, *purple:* $1.0 \times 10^{-8}$ $M_\odot$/yr and *black:* $1.0 \times 10^{-7}$ $M_\odot$/yr.

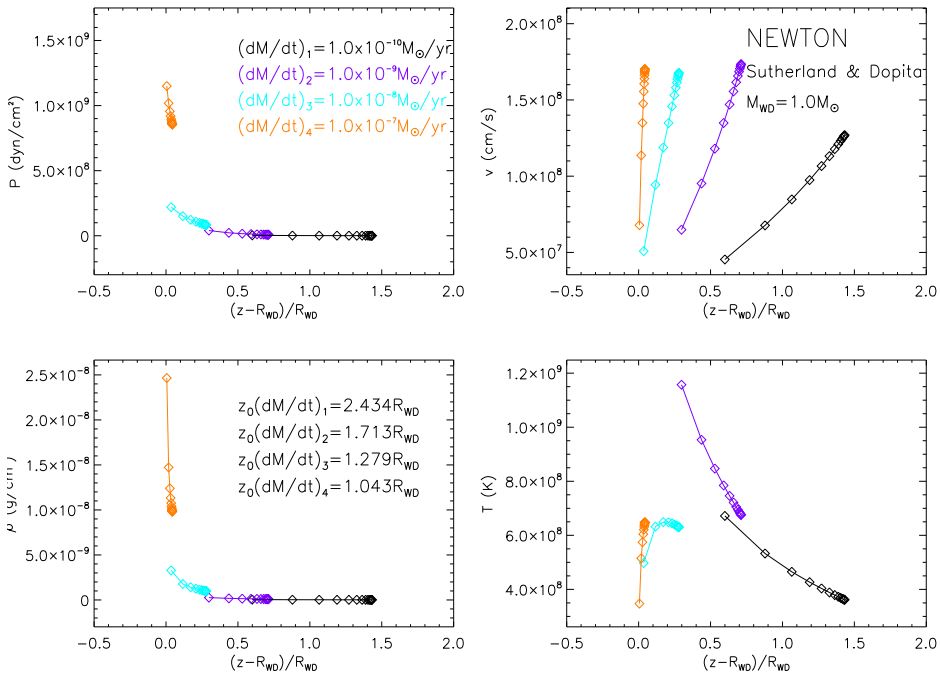


FIGURE 3.15: Pressure (*top-left*), velocity (*top-right*), density (*bottom-left*) and temperature (*bottom-rigth*) profiles with the results of the cooling function obtained by Sutherland & Dopita and for different accretion rates: *orange:* $1.0 \times 10^{-10}$ $M_\odot$/yr, *cyan:* $1.0 \times 10^{-9}$ $M_\odot$/yr, *purple:* $1.0 \times 10^{-8}$ $M_\odot$/yr and *black:* $1.0 \times 10^{-7}$ $M_\odot$/yr.

### 3.2.1 Profile comparisons among different models

The distributions of physical quantities in the post shock region are presented for a white dwarf mass of $M_{WD} = 0.8\ \mathrm{M}_{\odot}$ as a function of the distance in the shock region $(z - R_{WD})/R_{WD}$ using the numerical model described in Section §2.2 for both cooling functions, Zombeck and Sutherland & Dopita, are compared with models of Aizu (1973) and Frank, King, & Raine (2002) described in Sections §2.1.1 and §2.1.2, respectively.

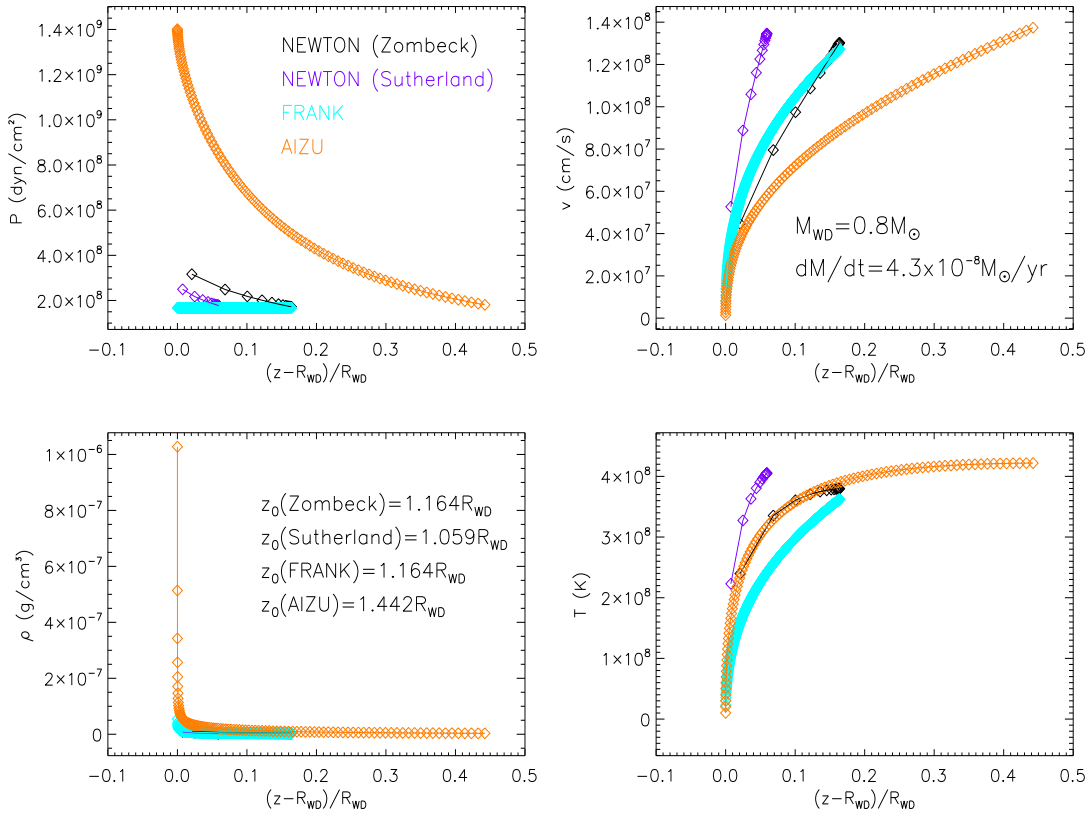


FIGURE 3.16: Pressure (*top-left*), velocity (*top-right*), density (*bottom-left*) and temperature (*bottom-rigth*) profiles with pure bremsstrahlung cooling as a function of $(z - R_{WD})/R_{WD}$ for a white dwarf mass of $0.8\ \mathrm{M}_{\odot}$. (*black:*) cooling function of Zombeck; (*purple:*) cooling of Sutherland & Dopita; (*cyan:*) Frank analytical approximation; (*orange:*) Aizu model.

Figure 3.16 shows the profiles with both cooling function, Zombeck *(black)* and Sutherland & Dopita *(purple)*, and Aizu (1973) *(orange)* and Frank, King, & Raine (2002) *(cyan)* approximations. The shock height, $z_0$, obtained is higher with the Aizu (1973) model, meanwhile the calculated with the cooling function of Sutherland & Dopita gives the lower value. Since in Frank, King, & Raine (2002) the shock position should be assumed, it takes the shock height determined with the cooling function of Zombeck.

This variation between the models in the determination of the shock height can be observed in Table 3.4 for different masses of white dwarfs.

TABLE 3.4: Shock height for different values of white dwarf masses with pure bremsstrahlung cooling, for the cooling functions of Zombeck and Sutherland & Dopita, and Aizu and Frank, King & Raine models.

| Model | $M_{WD}$ ($M_\odot$) | $\dot{M}$ ($M_\odot$/yr) | $z_0$ ($R_{WD}$) | |
|---|---|---|---|---|
| | | | Zombeck | Sutherland & Dopita |
| NEW | 0.6 | $4.3 \times 10^{-8}$ | 1.117 | 1.034 |
| | 0.8 | $4.3 \times 10^{-8}$ | 1.164 | 1.059 |
| | 1.0 | $4.3 \times 10^{-8}$ | 1.235 | 1.092 |
| | 1.2 | $4.3 \times 10^{-8}$ | 1.324 | 1.130 |
| | 1.4 | $4.3 \times 10^{-8}$ | 1.451 | 1.264 |
| FRANK | 0.6 | $4.3 \times 10^{-8}$ | 1.117 | — |
| | 0.8 | $4.3 \times 10^{-8}$ | 1.164 | — |
| | 1.0 | $4.3 \times 10^{-8}$ | 1.235 | — |
| | 1.2 | $4.3 \times 10^{-8}$ | 1.324 | — |
| AIZU | 0.6 | $4.3 \times 10^{-8}$ | 1.258 | — |
| | 0.8 | $4.3 \times 10^{-8}$ | 1.442 | — |
| | 1.0 | $4.3 \times 10^{-8}$ | 1.699 | — |
| | 1.2 | $4.3 \times 10^{-8}$ | 2.095 | — |

Due to this difference in the shock height, the pressure profile (top-left) between Aizu (1973) and the cooling Zombeck and Sutherland & Dopita seems to be more different that it really is. In fact, if the models are compared for the same post shock region the values of the pressure are similars. Neverthless the pressure in the anaylitical approximation of Frank, King, & Raine (2002) is assumed to be constant through the emission region.

These differences are less evident in the velocity profiles (top-right). The velocities at the shock (maximum velocities) are very similar among the models and the values nearby to the white dwarf surface are close to zero as is expected from the boundary condition, $v = 0$. Temperature profiles (bottom-right) exhibit a similar behaviour but, it is noticed that temperatures of Frank are slightly lower than the other ones. As well as the temperatures obtained with cooling Sutherland & Dopita are slighlty higher than the determined with the other models.
On the other hand, density profiles (bottom-left) have similar estimations between the models, the only difference, again, is observed in the pressure profiles (due to the shock height).

## 3.3 Spectrum continuum

In Section § 3.2, hydrodynamic calculations were carried out to determine the structure of the emission region. The temperature and density distributions obtained have been used

to generate the X-ray spectra emitted from the post shock accretion region with the goal to investigate the behaviour of the flux emitted in the emission region and determine the mass of the white dwarf (e.g. Ishida (1991); Cropper, Ramsay, & Wu (1998); Beardmore, Osborne, & Hellier (2000); Ramsay (2000)).

The post shock region model has been computed assuming solar abundances and fully ionized of all the abundant elements in the emission region. From Equation (2.61) the local bremsstrahlung emissivity is obtained for all the temperatures $T(z)$ and densities $\rho(z)$. Since the emergent spectra is the sum of many local emissivity spectra, the total bremsstrahlung spectra is obtained integrating Equation (2.61) from shock $z = z_0$ ($z' = 0$) to surface of the white dwarf $z = R_{WD}$ ($z' = z_0 - R_{WD}$) (Equation (2.60)), for an energy range between $1$ keV and $100$ keV. This assumption is reasonable at temperatures $kT > 1$ keV, therefore, the computed spectra are realiable at relatively high energies only ($E \gtrsim 3$ keV). At lower energies, the spectra are dominated by numerous emission spectral lines and photo-recombination continua (see e.g. Canalle et al. (2005)).
Examples of model spectra are presented in Figures 3.17 and 3.18 for a white dwarf mass of $0.8$ $M_\odot$ and an accretion rate $\dot{M} = 4.3 \times 10^{-8}$ $M_\odot/\mathrm{yr}$ for pure bremmstrahlung with the cooling functions of Zombeck and Sutherland & Dopita, respectively.

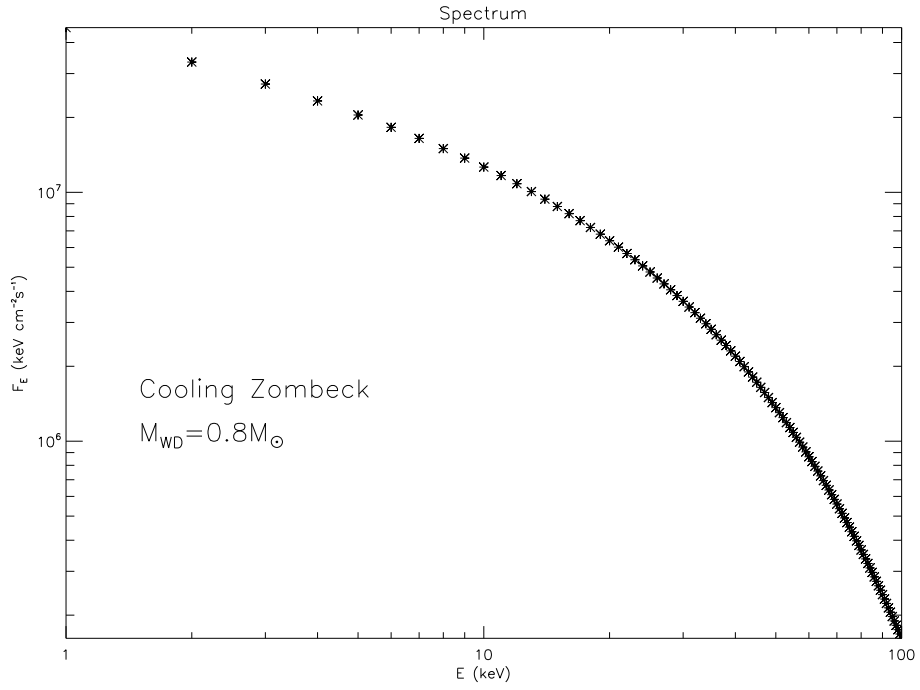


FIGURE 3.17: Calculated spectrum from a post shock region with bremsstrahlung cooling approximation of Zombeck and a mass of $0.8$ $M_\odot$; plotted in units of $\mathrm{keV cm^{-2} s^{-1}}$.

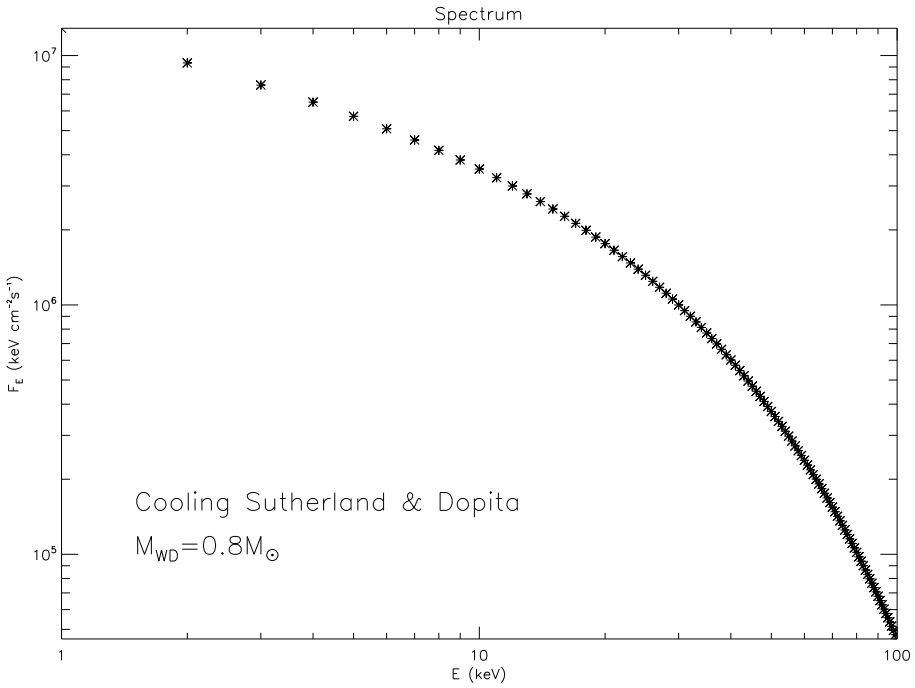


FIGURE 3.18: Calculated spectrum from a post shock region with the results of the cooling function obtained by Sutherland & Dopita and a mass of $0.8\ M_\odot$.

With the aim of comparing the spectrum obtained with each cooling function, the Figure 3.19 summarizes the two spectra.

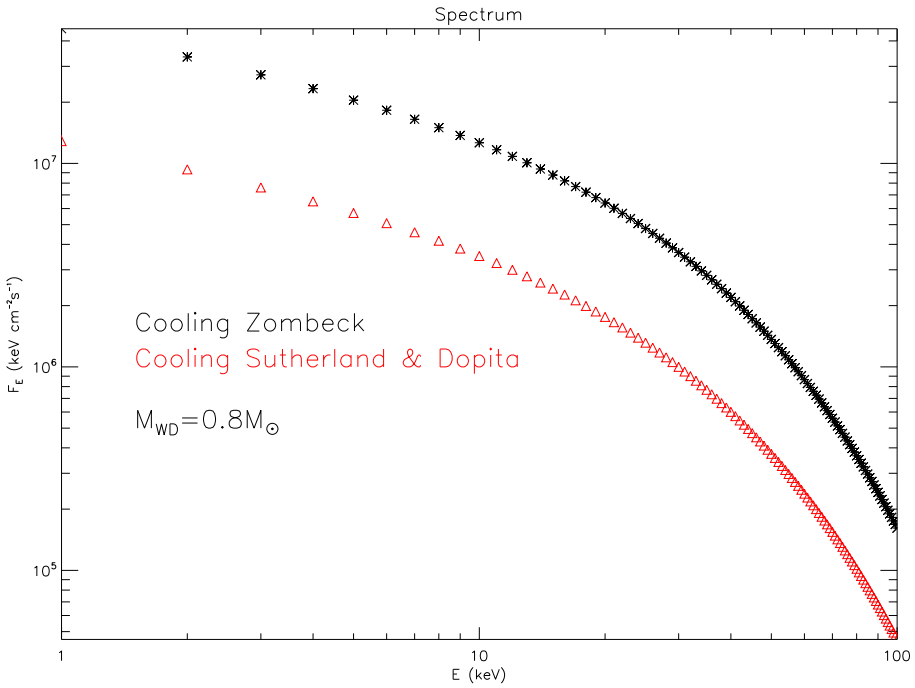


FIGURE 3.19: Calculated spectra from a post shock region with bremsstrahlung cooling functions of Zombeck (*(black)*) and Sutherland & Dopita (*(red)*) and a mass of $0.8\ M_\odot$.

As presented in Section §3.2, the shock height computed with the cooling function of Zombeck is higher, $z_{0_{(zck)}} = 1.164\ \mathrm{R_{WD}}$, than the obtained with the cooling function of Sutherland & Dopita, $z_{0_{(S\&D)}} = 1.059\ \mathrm{R_{WD}}$. Thus the amount of flux emited in the shock region is larger when the shock region is also larger as is observed in Figure 3.19.

### Influence of mass

A set of total spectra for four different white dwarfs, $M_{WD} = (0.6,\ 0.8,\ 1.0 \text{ and } 1.2)\ \mathrm{M_\odot}$, and cooling Zombeck and Sutherland & Dopita (Figures 3.20 and 3.21) is obtained. The accretion rate is fixed for all the computed spectra models at $\dot{M} = 4.3 \times 10^{-8}\ \mathrm{M_\odot/yr}$.

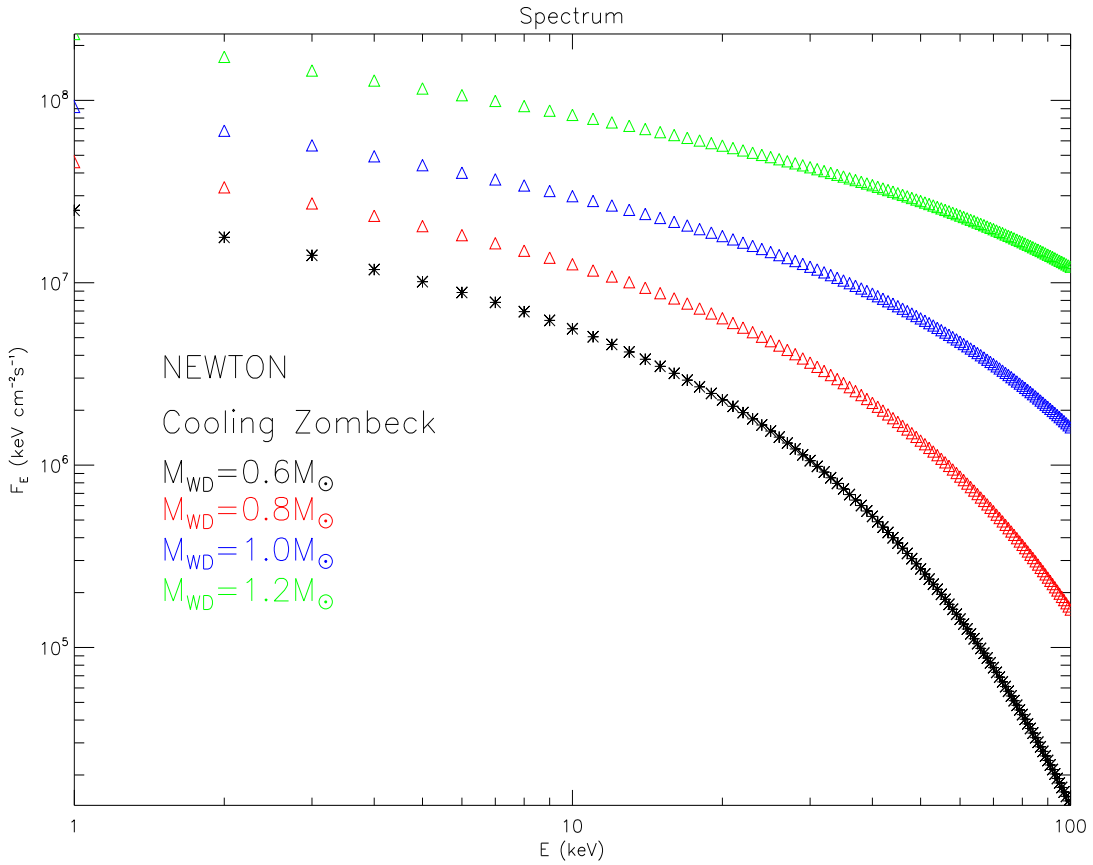


FIGURE 3.20: Comparison of model spectra with bremsstrahlung cooling approximation of Zombeck computed for four white dwarf masses: $0.6\ \mathrm{M_\odot}$ (*black asteriks*), $0.8\ \mathrm{M_\odot}$ (*red triangles*), $1.0\ \mathrm{M_\odot}$ (*blue triangles*) and $1.2\ \mathrm{M_\odot}$ (*green triangles*).

Because more massive white dwarfs have smaller radii, the corresponding shock temperatures are higher. A higher shock temperature implies a hotter post shock region, and hence a harder X-ray spectrum is observed as it is appreciated in Figures 3.20 and 3.21.

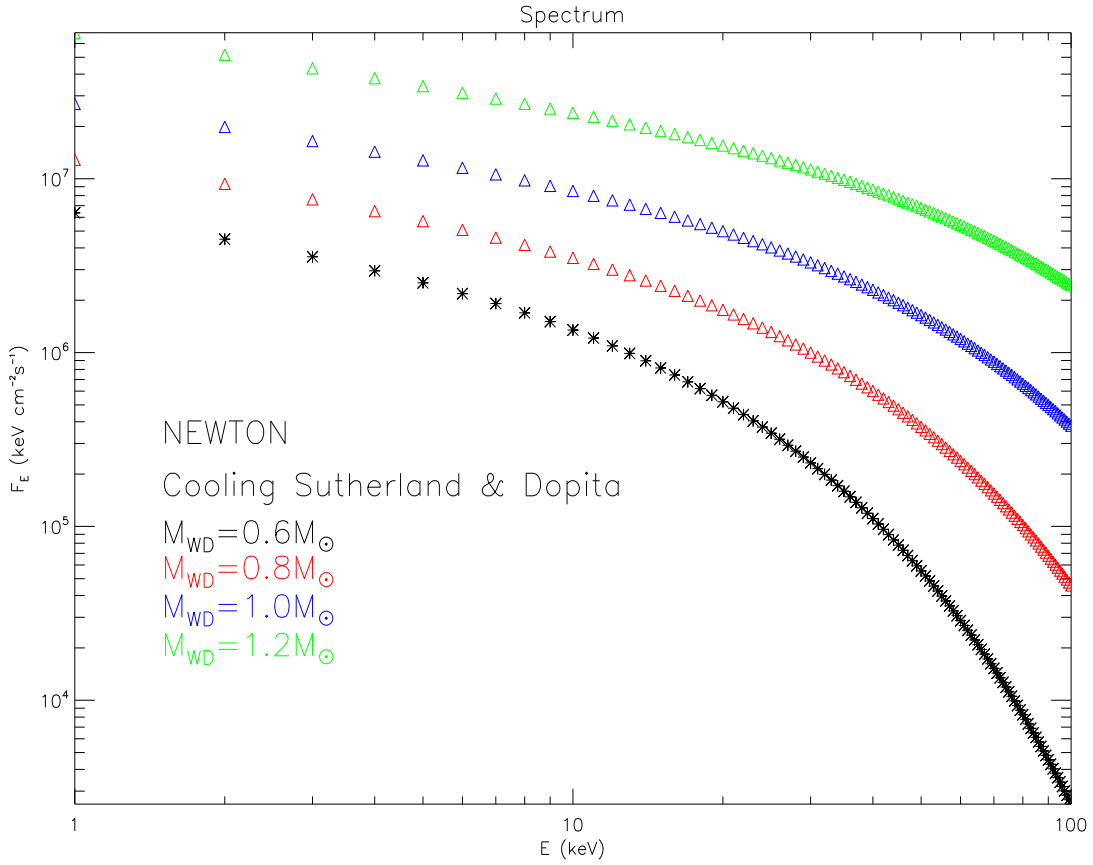


FIGURE 3.21: Comparison of model spectra with the results of the cooling function obtained by Sutherland & Dopita computed for four white dwarf masses: $0.6\ \mathrm{M}_{\odot}$ (*black asteriks*), $0.8\ \mathrm{M}_{\odot}$ (*red triangles*), $1.0\ \mathrm{M}_{\odot}$ (*blue triangles*) and $1.2\ \mathrm{M}_{\odot}$ (*green triangles*).

The local mass accretion rate changes from $a \approx 0.2\ \mathrm{g\ s^{-1}cm^{-2}}$ for the lightest white dwarf to $a \approx 10\ \mathrm{g\ s^{-1}cm^{-2}}$ for the heaviest white dwarf in accordance with the decreasing white dwarf radius.
For less massive white dwarf the maximum of the spectrum is obtained at lower energies, $\sim 5\ \mathrm{keV}$, with a sharp drop towards higher energies. The maximum of the spectrum is shifted to higher energy values as the mass increases. For a white dwarf of $1.0\mathrm{M}_{\odot}$ the maximun flux is emitted at about $50\ \mathrm{keV}$.

In addition, to compare both cooling functions, Figure 3.22 shows the spectra for different masses of white dwarfs and an accretion rate of $\dot{M} = 4.3 \times 10^{-8}\ \mathrm{M}_{\odot}/\mathrm{yr}$. *Asterisk* corresponds to spectra computed with the cooling function of Zombeck, while the *crosses* are the spectra for different masses using the tabulated cooling of Sutherland & Dopita, respectively.

As in Figure 3.19, since the emission region of Zombeck is higher than the obtained with Sutherland & Dopita, the total bremsstrahlung spectra for different masses are higher for cooling Zombeck and, like before, it is also possible appreciate that the maximum of the

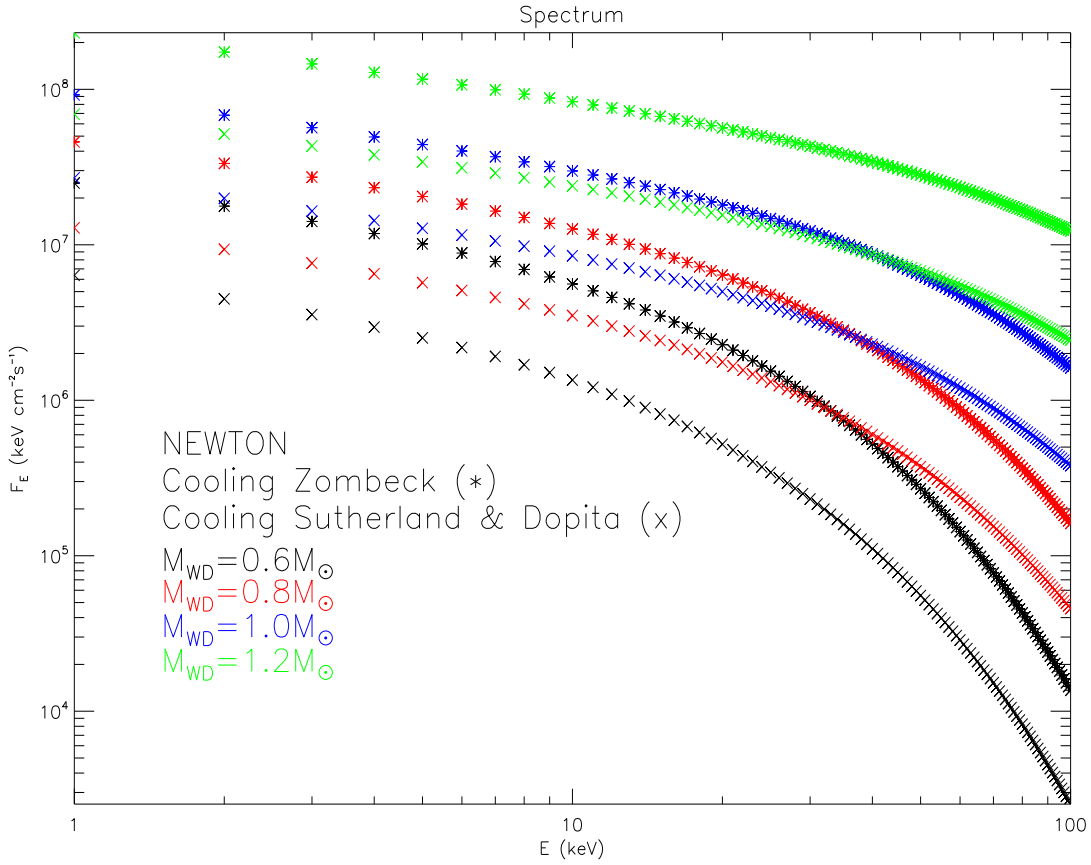


FIGURE 3.22: Comparison of model spectra with cooling Zombeck and Sutherland & Dopita computed for four white dwarf masses: 0.6 $M_\odot$ (*black asteriks*), 0.8 $M_\odot$ (*red triangles*), 1.0 $M_\odot$ (*blue triangles*) and 1.2 $M_\odot$ (*green triangles*).

spectrum is obtained at lower energies with a sharp drop towards higher energies.

**Influence of the accretion rate**

Since the local mass accretion rate significantly alters the profiles of the density and temperature distributions, as discussed in Section §3.2, the X-ray spectra is calculated with the density and temperature distributions obtained there, and it is found that the X-ray spectra also depend on the specific accretion rate. Thus, the X-ray spectra have been determined for four different accretion rates $\dot{M} = (1.0 \times 10^{-10}, 1.0 \times 10^{-9}, 1.0 \times 10^{-8}, \text{ and } 1.0 \times 10^{-7})\mathrm{M}_\odot/\mathrm{yr}$ and a white dwarf mass of 1.0 $M_\odot$. The corresponding values of local mass accretion rate for a $M_{WD} = 1.0\ \mathrm{M}_\odot$ can be appreciated in Table 3.3. Figure 3.23 and 3.24 show the spectra for a total bremsstrahlung emissivity with the cooling approximation of Zombeck and cooling function obtained by Sutherland & Dopita, respectively.

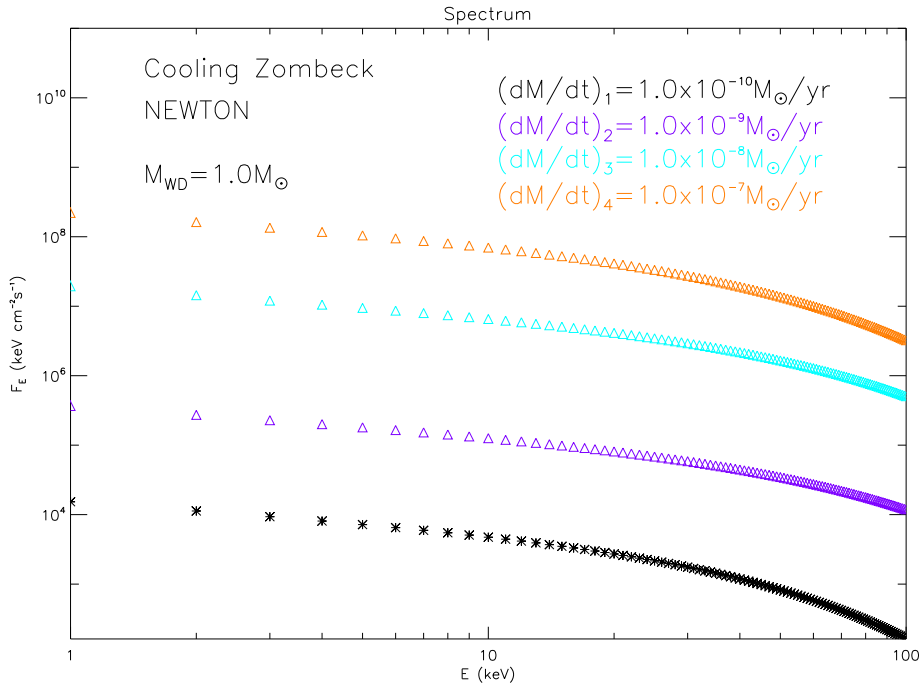


FIGURE 3.23: Spectrum for different values of accretion rate: $\dot{M} = 1 \times 10^{-7}\mathrm{M}_\odot/\mathrm{yr}$ (*orange*), $\dot{M} = 1 \times 10^{-8}\mathrm{M}_\odot/\mathrm{yr}$ (*cyan*), $\dot{M} = 1 \times 10^{-9}\mathrm{M}_\odot/\mathrm{yr}$ (*purple*) and $\dot{M} = 1 \times 10^{-10}\mathrm{M}_\odot/\mathrm{yr}$ (*black*) and bremsstrahlung cooling approximation of Zombeck.

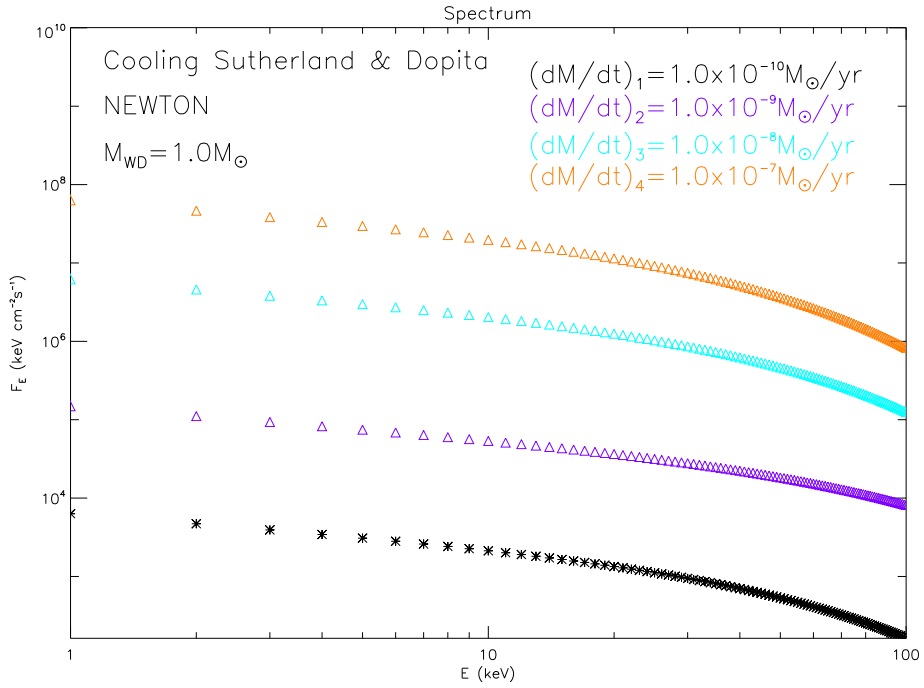


FIGURE 3.24: Spectrum for different values of accretion rate: $\dot{M} = 1 \times 10^{-7}\mathrm{M}_\odot/\mathrm{yr}$ (*orange*), $\dot{M} = 1 \times 10^{-8}\mathrm{M}_\odot/\mathrm{yr}$ (*cyan*), $\dot{M} = 1 \times 10^{-9}\mathrm{M}_\odot/\mathrm{yr}$ (*purple*) and $\dot{M} = 1 \times 10^{-10}\mathrm{M}_\odot/\mathrm{yr}$ (*black*) and with the results of the cooling function obtained by Sutherland & Dopita.

In order to compare between both cooling types (Zombeck + Sutherland & Dopita), Figure 3.25 shows directly the spectrum for a white dwarf mass of $M_{WD} = 1.0\ \mathrm{M}_{\odot}$ and different values of accretion rates $\dot{M} = (1.0 \times 10^{-10}, 1.0 \times 10^{-9}, 1.0 \times 10^{-8}, \text{ and } 1.0 \times 10^{-7})\ \mathrm{M}_{\odot}/\mathrm{yr}$ obtained from each of them.

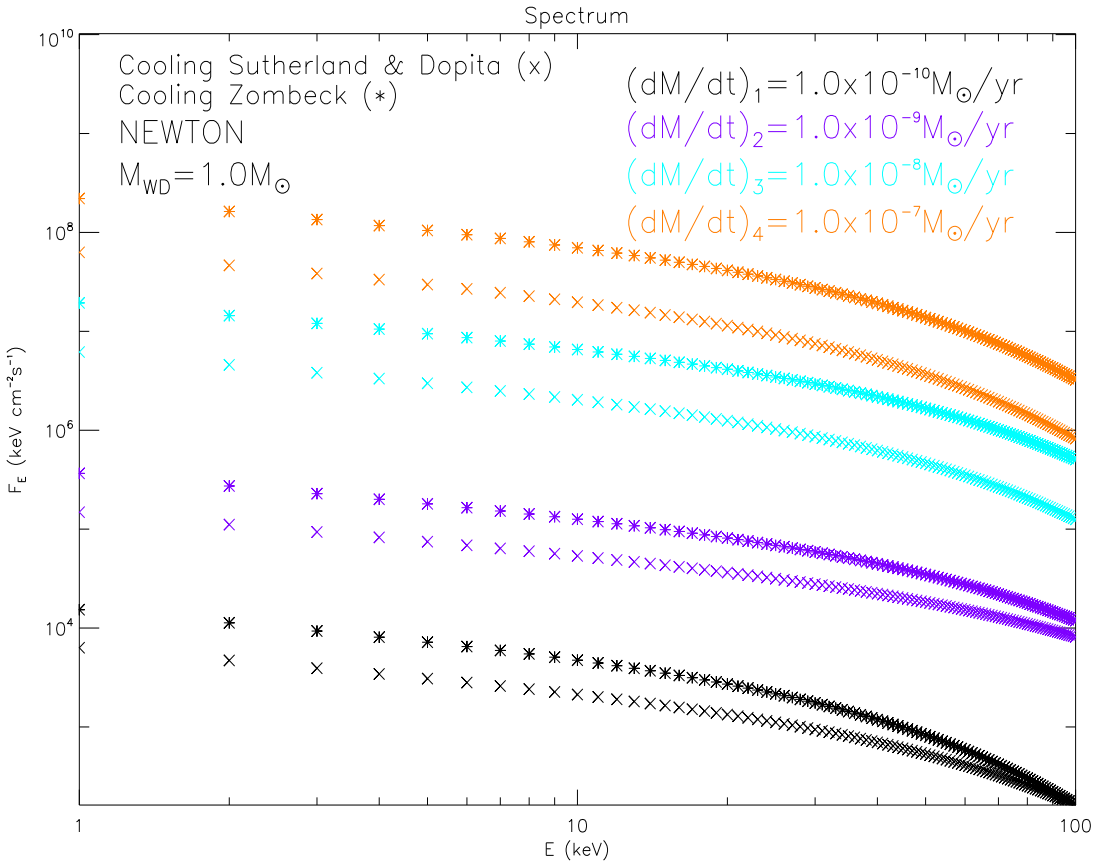


FIGURE 3.25: Spectrum for different values of accretion rate: $\dot{M} = 1 \times 10^{-7}\mathrm{M}_{\odot}/\mathrm{yr}$ (*orange*), $\dot{M} = 1 \times 10^{-8}\mathrm{M}_{\odot}/\mathrm{yr}$ (*cyan*), $\dot{M} = 1 \times 10^{-9}\mathrm{M}_{\odot}/\mathrm{yr}$ (*purple*) and $\dot{M} = 1 \times 10^{-10}\mathrm{M}_{\odot}/\mathrm{yr}$ (*black*) and bremsstrahlung cooling approximation of Zombeck (*asterisks*) and the results of the cooling function obtained by Sutherland & Dopita (*crosses*).

From Table 3.3 it is possible to appreciate that when the accretion rate, $\dot{M}$, is small the specific accretion rate, $a$, is small. Since the temperature in the post shock accretion region reduces the X-ray spectra soften. For instance, the continuum radiated by bremsstrahlung generally reduces as $a$ decreases, which is prominent above $10\ \mathrm{keV}$ because the accretion column becomes cooler and the maximum temperature downs. In contrast, if the accretion rate increase, the local mass accretion rate is higher and the temperature in the shock region increase causing a harder X-ray spectrum as it is demostrated in Figures 3.23, 3.24 and 3.25.

### 3.3.1 Spectral comparisons among different models

Spectra calculated with models of Aizu and Frank are obtained with the aim to compare with the model presented in this work. Spectrum for a white dwarf mass of $M_{WD} =$

$0.8\ \mathrm{M}_\odot$ with $\dot{M} = 4.3 \times 10^{-8}\ \mathrm{M}_\odot/\mathrm{yr}$ is presented in Figure 3.26. Purple points correspond to the present model with the results of the cooling function obtained by Sutherland & Dopita; black points are the spectra calculated with the cooling approximation of Zombeck; orange points are the calculated spectrum with Aizu's model; and cyan points correspond to the analytical approximation of Frank under constant pressure.

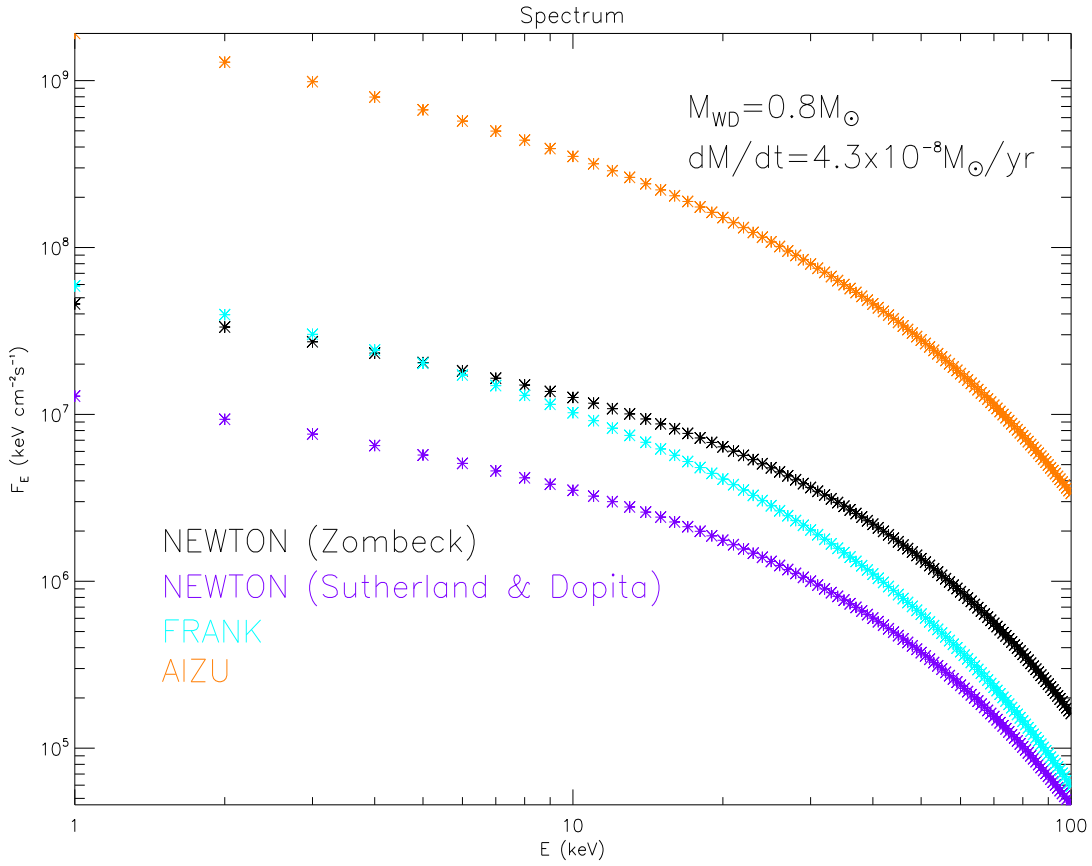


FIGURE 3.26: Spectrum for a WD of mass $M_{WD} = 0.8\ \mathrm{M}_\odot$ for different models.

Figure 3.26 shows that Aizu spectra is higher than the spectra obtained with the model of Frank and the model presented here, calculated for both cooling functions. Being the flux computed with the cooling function of Sutherland & Dopita is the lowest. Since the same accretion rate has been considered for all models, the determining parameter in the spectra calculation is the shock height and therefore the thickness of the emission region.

It is expected that for higher temperatures, the emitted flux would be higher. From the profiles obtained in Section §3.2, it can be seen that the maximum temperature of Aizu is higher than other models, which explains that it has the higher emitted flux. After this, the higher shock temperature is derived by our model using the Sutherland & Dopita cooling. However, the flux emitted derived by this model is not the second largest. This emphasizes the importance of the calculation of the height of the shock since the model calculated with the cooling of Sutherland & Doipta determines a lower shock height than

those obtained with the other models as can be seen in Table 3.4.

Although Frank's model has been calculated with the same shock height obtained with the model with cooling of Zombeck and the model of Frank has lower temperature maximum than model with cooling approximation of Zombeck, the model of Frank reaches a flux higher at low energies than the model of Zombeck. But, at high energies the flux emitted from Frank's model is lower.

### 3.3.2 FITS table model

In order to fit the model presented in Section §2.2 to X-ray observations, the spectra obtained for different white dwarfs masses and a fixed local mass accretion rate have been integrated it into the X-ray spectral fitting package, *XSPEC*, (Arnaud, 1996).

Using the described method in Sections §2.2 and §3.3, spectra have been obtained for solar abundances and for different masses of white dwarfs from $0.6\mathrm{M}_{\odot}$ to $1.4\mathrm{M}_{\odot}$ with a step of $0.1\ \mathrm{M}_{\odot}$ and $\ 1.4)\mathrm{M}_{\odot}$ and an accretion rate $\dot{M} = 4.3 \times 10^{-8}\mathrm{M}_{\odot}/\mathrm{yr}$.

Tables with the calculated spectra have been created with *IDL programming language* from an ASCII file with the information of flux and energies where the energy interval is from $0.1\ \mathrm{keV}$ to $100\ \mathrm{keV}$ with steps of $0.1\ \mathrm{keV}$ and for both cooling functions, Zombeck and Sutherland & Dopita, following the requirements of XSPEC for additive table models (for details see Appendix C).

A table model, in XSPEC, is a very simple way of fitting with user-defined models and is available for a particular class of models. These are models that can be defined by a grid of spectra, with the elements of the grid covering the range of values of the parameters of the model. For instance, for a one-parameter model, a set of model spectra can be tabulated for different values of the parameter, $P1$, $P2$, $P3$, etc. The model for a given value of $P$ is calculted by interpolating on the grid model spectrum. The generalization to more parameters works in the obvious way.
As with standard models, the model spectra should be in terms of flux-per-bins and not flux-per-keV. Any set of energy bins can be used, and XSPEC interpolate the model spectra onto the appropriate energy bins for the detectors in use. It is therefore a good idea to choose energy bins such that the spectrum is well-sampled over the range of interest. The file structure for these models is a FITS format[1].

[1]The FITS file structure for models in XSPEC is described at: http://heasarc.gsfc.nasa.gov/docs/heasarc/ofwg/docs/general/ogip_92_009/ogip_92_009.html
Additional information at:
http://www.darts.isas.ac.jp/pub/legacy.gsfc.nasa.gov/software/lheasoft/lheasoft6.3/headas-6.3.2/ftools/spectral/tables/
ftp://legacy.gsfc.nasa.gov/fits_info/fits_formats/docs/

Figure 3.27 shows the spectra for different masses using the bremsstrahlung cooling approximation of Zombeck. The aditive table model is called `ipzk.fits`.

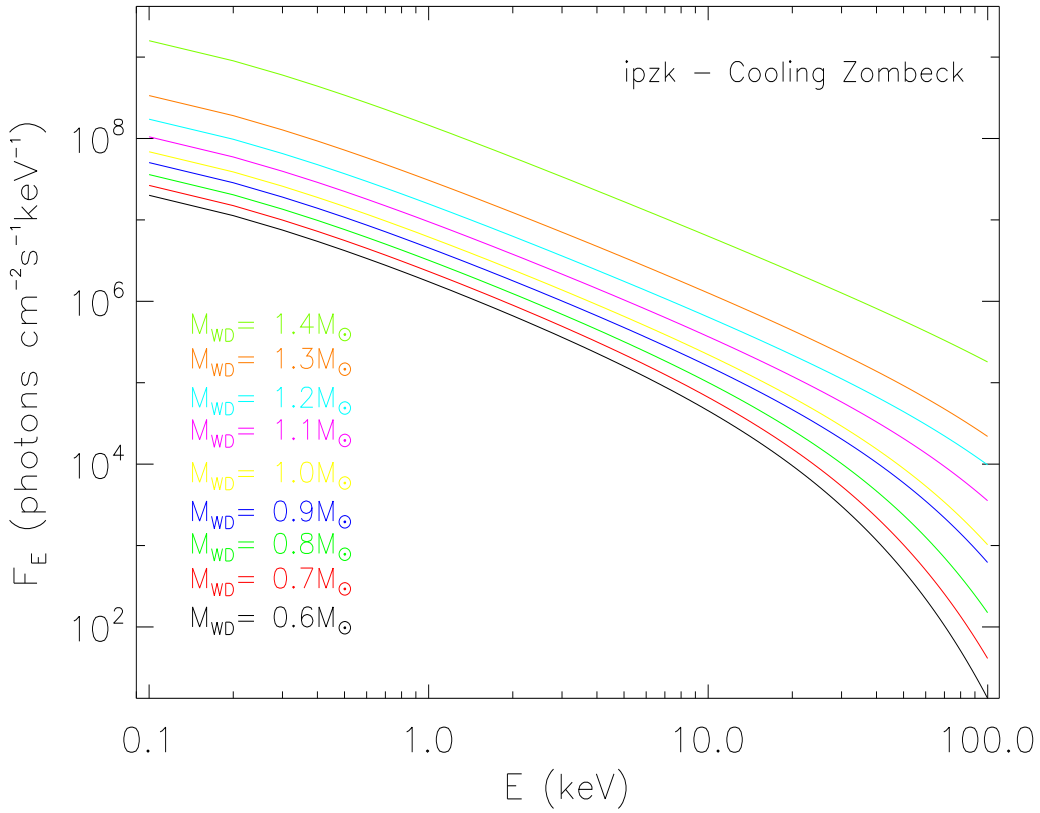


FIGURE 3.27: Spectra obtained from the FITS table model, ipzk.fits, calculated using the cooling approximation of Zombeck for all the interval of white dwarf masses.

As in Figure 3.28, spectra have been obtained with the results of the cooling function determined by Sutherland & Dopita, `ipsd.fits`.

Recently, Suleimanov et al. (2016) presented a new set of Intermediate Polar model spectra that quantitatively account for the finite size of the magnetosphere. The models are calculated for a set of magnetospheric radii, expressed in units of white dwarf radii, assuming a relatively high local mass accretion rate and also ignore cyclotron cooling.

The local mass accretion rate is fixed to $a = 1\ \mathrm{g\,s^{-1}cm^{-2}}$ for all the computed spectral models. A set of post.shock region model spectra have been computed for the white dwarf mass $M_{WD}$, and the relative magnetospheric radius $R_m/R$. The grid was computed for 56 values of white dwarf mass from $0.3$ to $1.4\ \mathrm{M_\odot}$ with a step of $0.02\ \mathrm{M_\odot}$, i.e. 2296 models in total. Every post shock region model has been computed for a fixed mass accretion rate $\dot{M} = 10^{16}\ \mathrm{g\,s^{-1}}$.

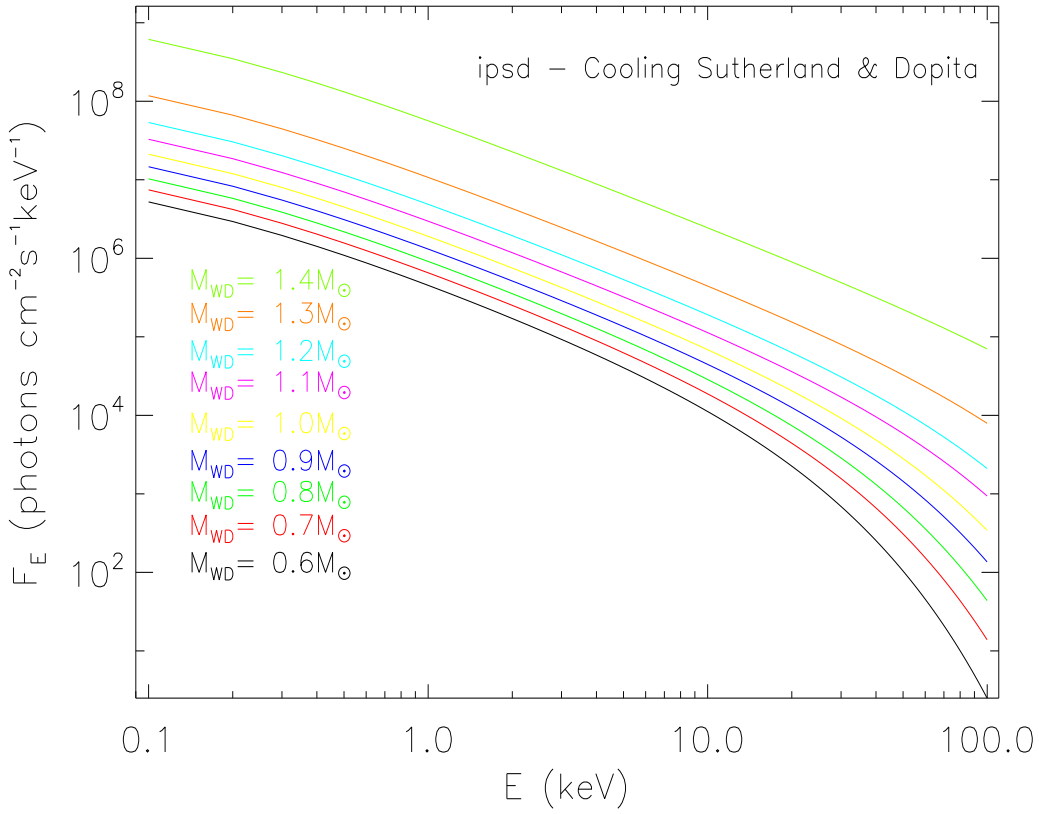


FIGURE 3.28: Spectra obtained from the FITS table model, ipsd.fits, calculated using the cooling function results of Sutherland & Dopita for all the interval of white dwarf masses.

In previous work, Suleimanov, Revnivtsev, & Ritter (2005), used the cooling function $\Lambda_N$ computed by Sutherland & Dopita (1993). But in Suleimanov et al. (2016), they used a cooling function computed by the code APEC (Smith et al., 2001) using the database AtomDB[2] for a solar chemical composition. The grid has been distributed as an XSPEC additive table model like `ipolar.fits`[3] and publicly available to the scientific community.

The tabulated model of Suleimanov et al. (2016) for different masses of white dwarf $M_{WD} = (0.6, 0.7, ..., 1.4)M_\odot$ and magnetospheric radius $R_m/R = 1000$, which represent the pseudo-infinity magnetospheric radius, has been plotted in Figure 3.29 with an accretion rate $\dot{M} = 1.6 \times 10^{-9} M_\odot/yr$.

[2] http://www.atomdb.org/
[3] https://heasarc.gsfc.nasa.gov/xanadu/xspec/models/ipolar.html

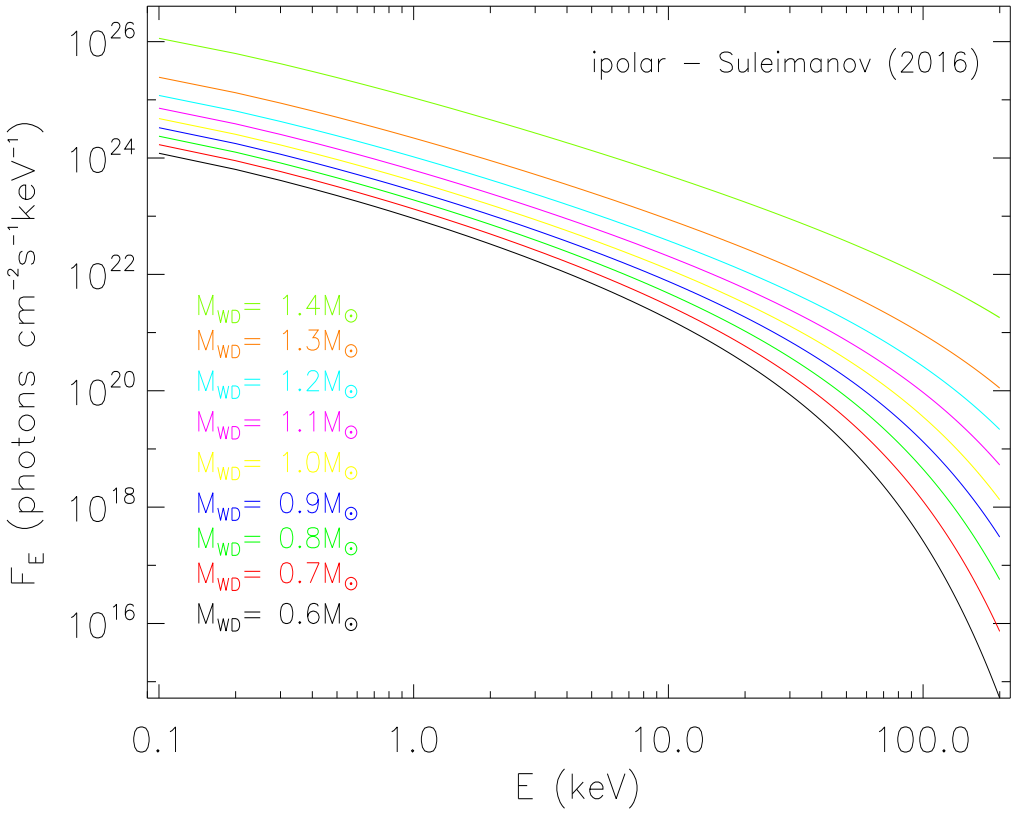


FIGURE 3.29: Spectra obtained from the FITS table model, ipolar.fits, for a magnetospheric radius $R_m/R = 1000$.

The comparison between the spectra tabulated models of Suleimanov et al. (2016) (black) and those derived with our model using the cooling Zombeck [`ipzk.fits`] (blue) and cooling Sutherland & Dopita [`ipsd.fits`] (green) for diferent masses is shown in Figure 3.30. They have been computed from a solar chemical composition using an accretion rates of $\dot{M} = 1.6 \times 10^{-9} M_\odot/yr$ and $\dot{M} = 4.3 \times 10^{-8} M_\odot/yr$ for Suleimanov's and our models, respectively.

Although the accretion rate used by Suleimanov et al. (2016) is lower, $1.6 \times 10^{-9}$ $M_\odot$/yr, than the accretion rate used in this work, $4.3 \times 10^{-8}$ $M_\odot$/yr, the flux obtained is higher than those derived with our models independiently of the cooling used. This result is not well understood, since at a higher accretion rate, means that the temperature is higher and therefore the flow emitted increases. It is likely that this difference between the models is partly due to the cooling function used by of them.

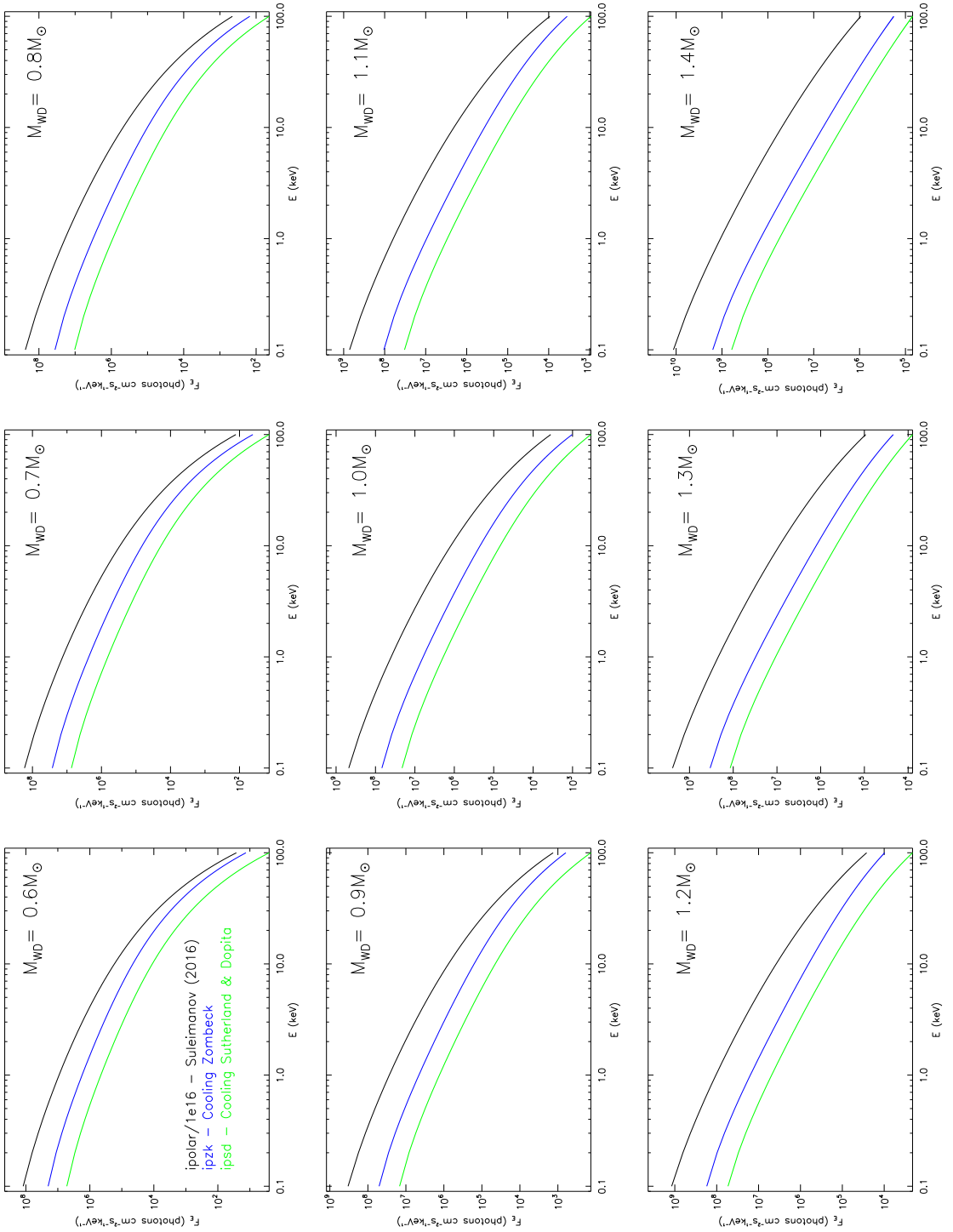


FIGURE 3.30: Spectra for different models and masses of white dwarfs.

# 4

# NOVA OPH 1998 (V2487 OPH)

In this chapter, the tabulated model in Section § 3.3.2 is applied to *XMM-Newton* and *INTEGRAL* observations of Nova Ophiuchi 1998 (V2487 Oph).
A photoelectric absorption column density, phabs in *XSPEC*, have been added to the thermal bremsstrahlung model in order to fit the observations. Also, a blackbody spectrum, bbody, have been used with the aim to fit the soft part of the spectra of the Nova Oph 1998. Since fluorescent Fe K$\alpha$ line at $6.4$ keV have been identified, (Hernanz & Sala, 2002) sometimes is introduced in the spectral analysis through a Gaussian. At the same time, the energy band below $0.3$ keV for the *XMM-Newton* observations have been exclude because of inadequate instrumental response. Finally, as the shock temperature depends on the mass of the white dwarf, the X-ray spectra is used to determine the mass of the white dwarf.

## 4.1 Introduction of Nova Oph 98 (V2487 Oph)

V2487 Oph was optically discovered in outburst on 1998 June 15.561 UT (Nakano et al., 1998) with a visual magnitude of $9.5$ and was confirmed as a nova by spectral observations on 1998 June 18 (Filippenko et al., 1998). It was a very fast nova, with $t_2 \approx 6.3$ days and $t_3 \approx 9.5$ days[1] (Liller & Jones (1999a); Liller & Jones (1999b)).
From observations of the near-IR lines OI $\lambda 8446$ and $\lambda 11287$, Lynch et al. (2000) obtained a color excess $E(B-V) = 0.38 \pm 0.08$, and thus a visual extinction $A_V = 1.16 \pm 0.24$ mag. Using an empirical relation to determine the absolute visual magnitude between $t_2$ and $M_V^{max}$, they calculated the absolute visual magnitude $M_V^{max} = -8.8$ and estimated an

[1] $t_2$ and $t_3$ are defined as the elapsed time to decreases of 2 and 3 magnitudes in its visual luminosity, respectively.

unusually large distance of $d = 27 \pm 3$ kpc. Given the galactic coordinates of the source, $6.60, +7.77$, this would situate V2487 Oph above the galactic plane and out of the disk, an unlikely position for this class of object.
As this nova was a very fast nova, it is possible that the real maximum of its magnitude had been missed and that the true absolute visual magnitude had been brighter. Extrapolating the visual light curve back in time to the pre-discovery data using the expression in Harris et al. (1999), the magnitude can be estimated to be in the range $6.8 - 9.5$ mag, and the final distance obtained is to range between $8$ and $27$ kpc (Hernanz & Sala, 2002).

Pagnotta, Schaefer, & Xiao (2008) reported, from the Harvard College Observatory archival photograph collection, the discovery of a previously unknown eruption of the nova. V2487 Oph was previously classified as a classical nova, but Pagnotta, Schaefer, & Xiao (2008) identified it as a probable recurrent nova based on its large expansion velocities and the presence of high excitation lines in the outburst spectrum. They noted that V2487 Oph had a magnitude in the $B$-filter of $10.27 \pm 0.11$ on 1900 June 20, near its peak magnitude of $9.5$ observed during the outburst in 1998 (see also Pagnotta et al. (2009)). Afterwards they identified V2487 Oph as a strong galactic recurrent nova candidate because of its low outburst amplitude, the very fast decline rate, the high expansion velocity, and the presence of high-excitation lines in its outburst spectrum. In 2002, Hachisu et al. (2002) already was suggested the same idea because the rapid decline and the presence of a plateau phase in the optical nova's light curve, which represent common features for the U Sco subclass of recurrent novae. They reproduced the V2487 Oph light curve shape of the 1998 outburst, and identified the nova as a good candidate for a recurrent nova and a type Ia Supernova progenitor. Further, more authors (e.g. Strope, Schaefer, & Henden (2010); Schaefer (2010)) have studied the V2487 Oph optical light curve in deep, and confirmed the connection with a probable recurrent nature for the source.

### 4.1.1 High energy observations

V2487 Oph has been observed as a high energy source through the detection of different X-rays satellites like the X-ray Multi-Mirror Mission, *XMM-Newton*, the INTErnational Gamma-Ray Astrophysics Laboratory, *INTEGRAL*, and the Rossi X-ray Timing Explorer, *RXTE*.

Nova Oph 1998 has been detected with the *XMM-Newton* satellite at five epoch: $2.7$, $3.2$, $3.7$, $4.3$ and $8.8$ years after outburst. Details of the X-ray observations with *XMM-Newton* and analysis are discussed below. Also was detected with the *INTEGRAL/IBIS* satellite in the $20 - 100$ keV range (Barlow et al., 2006) and later, it was detected with *RXTE/PCA* (Butters et al., 2011).

These observations in X-rays show that Nova Oph 1998 exhibits characteristics of Intermediate Polar and indicate that the white dwarf should be magnetic. In addition, the

shape of the optical curve seem to indicate that the white dwarf in this nova is quite massive, which is in agreement with the discovery that Nova Oph 1998 is a recurrent nova (Pagnotta et al., 2009); only novae with very massive white dwarfs can erupt as frequently as recurrent novae, which have recurrence periods smaller than $\sim 100$ years, i.e., more than one recorded outburst.

The first study of the X-ray data was performed by Hernanz & Sala (2002) who analyzed the first two *XMM-Newton* observations of V2487 Oph performed in 2001; first and second observation, 2.7 and 3.2 years after outburst, respectively. Figure 4.1 shows the observed spectra of V2487 Oph with The European Photon Imaging Camera *EPIC MOS1*, *MOS2* and *PN* data of the second observation. Continuous lines show the models that best fit the data from the three instruments simultaneously. The lower panel displays the residuals between the models and the data in units of sigma. The reduced $\chi^2$ of the fit is $\chi^2_\nu = 1.18$.

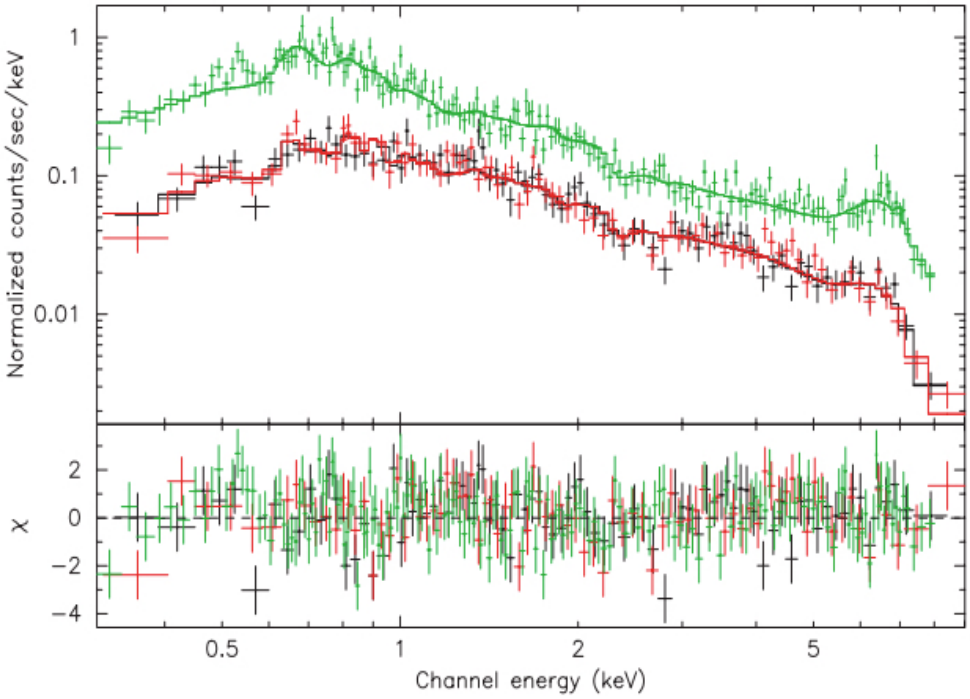


FIGURE 4.1: Observed spectra of V2487 Oph, *EPIC MOS1*, *MOS2*, and *PN* data (second observation, done on February 25 2001, 1178 days after outburst). The lower panel displays the residuals between the models and the data in units of $\sigma$ (Image from Hernanz & Sala (2002).

V2487 Oph did not appeared as a supersoft X-ray source, which emission is due to residual H-burning on top of the white dwarf but showed a flat continuum shape extending up to 12 keV. Moreover an excess emission at 6.4 keV corresponding to the neutral Fe K$\alpha$ fluorescence phenomenon was also detected, mostly due to reflection of high energy photons produced in the accretion process in a CV-like system. This revealed the recovery of

the accretion process as soon as $\sim 2.7$ years (less than 1000 days) after the nova outburst. In addition, positional correlation with the X-ray source $1RXS\ J173200.0-1934$ detected by the *RASS* (*ROSAT* All-Sky Survey) in 1990 was established, making of V2487 Oph the first classical nova observed before and after the outburst in X-rays.

Sala (2004b) (see also Sala (2004a) for details) analyzed the first three observations of *XMM-Newton*, 2.7, 3.2 and 3.7 years after outburst. The X-ray spectra detected with the *EPIC* cameras are shown in Figures 4.2, 4.3 and 4.4.

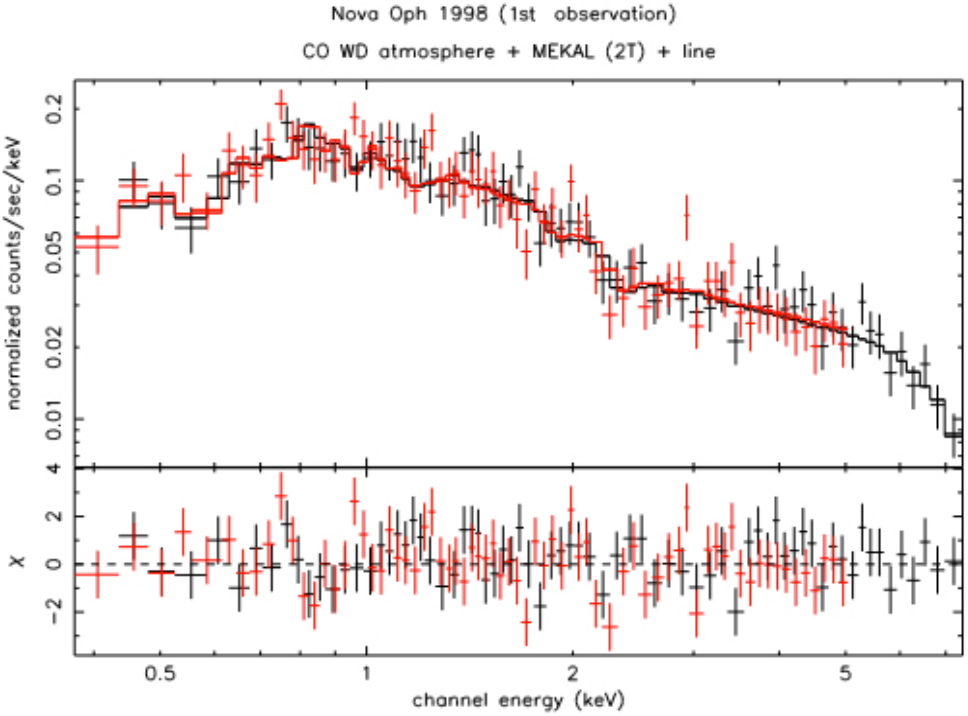


FIGURE 4.2: V2487 Oph observed spectra 2.7 years after the outburst from the two *EPIC MOS* cameras, *MOS1* (black), *MOS2* (red) and best fit model. The lower panel displays the residuals (data minus folded model) in terms of sigmas, with error bars of size one. (Image from Sala (2004a)).

In all observations the nova was detected as a bright X-ray source. The spectrum is dominated by thermal plasma emission and was modeled by a two-temperature MEKAL model (Mewe, Gronenschild, & van den Oord (1985); Mewe, Lemen, & Oord (1986)). The $\chi^2_\nu$ for the best fit model obtained for the first, second and third observation are 1.07, 1.13 and 1.24, respectively. The best fit thermal plasma model has a cool component, at $0.2-3$ keV, and a hot component, with temperatures above $\sim 64$ keV for the second and third observations, and above $\sim 10$ keV in the first one. The plasma spectrum at these high temperatures is very flat, and the temperature was not well constrained. In the case of the first observation, data from the *PN* camera was missing, and the parameters of the model were in general less constrained than in the second and third observations.

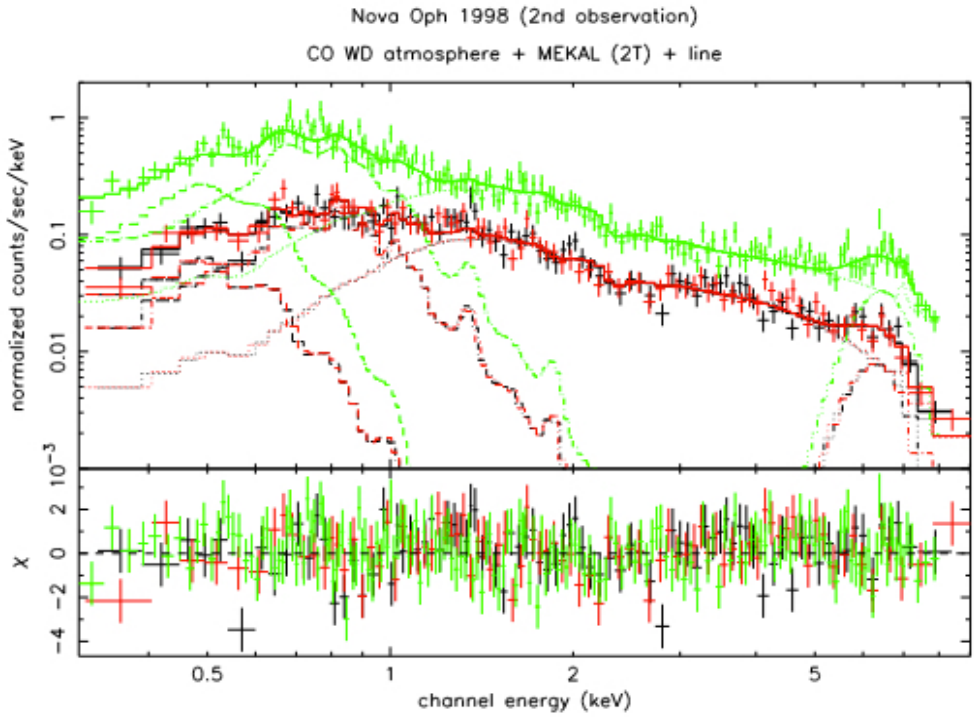


FIGURE 4.3: Observed spectra of V2487 Oph 3.2 years after outburst and best fit model. Data from the three *EPIC* cameras are shown: *MOS1* (black), *MOS2* (red), and *PN* data (green, with higher count rate), as well as the contribution of each component of the best-fit model (from left to right, white dwarf atmosphere, low temeprature MEKAL, high temeprature MEKAL and Gaussian emission line). The lower panel displays the residuals in terms of sigmas. (Image from Sala (2004a)).

In all observations, with the two-component model, the data showed an excess around $\sim 6.4 - 6.5$ keV and for this reason and additional Gaussian line centered at this energy and with a width $\sigma = 0.6$ keV counted for this excess. However, the two-temperature thermal plasma model not explain well the soft part of the spectrum, which was well fitted with a white dwarf atmosphere model (from MacDonald & Vennes (1991)), absorbed by a hydrogen column density of $N_H = 4 \times 10^{21}$ cm$^{-2}$ that is slightly larger than the average interstellar absorption in the direction of the source, $2.1 \times 10^{21}$cm$^{-2}$, (Dickey & Lockman, 1990). The best fit was obtained with effective temperatures between 64 and 74 eV and a bolometric luminosity $\sim 10^{35}$ erg s$^{-1}$, assuming a distance of 10 kpc, which implies a radius of the emitting region of $3 \times 10^7$ cm for the first observation and of $\sim 1.6 \times 10^7$ cm in the second and third ones. This is clearly smaller than the whole white dwarf surface, indicating that it must be associated to a hot emitting region of the star. Although the spectral model that fits the data was the same in the three observations, the total observed flux decreases with time.

For Sala (2004a), the fact that the emission line at $\sim 6.4 - 6.5$ keV must be simulated with an additional Gaussian line added to the MEKAL model, which already included the iron lines of the thermal plasma, indicates that it must be powered by some extra mechanism. As a fluorescent line at 6.41 keV can be produced by cold, neutral iron, other fluorescent

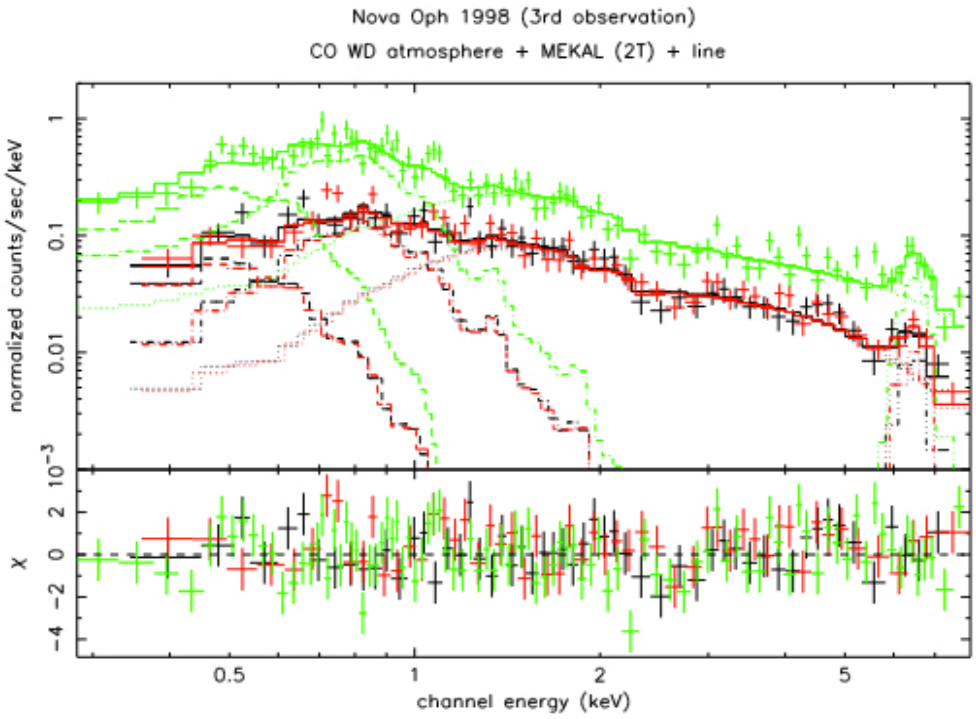


FIGURE 4.4: Observed spectra of V2487 Oph 3.7 years after outburst and best fit model. The lower panel displays the residuals in terms of sigmas. Data from the three *EPIC* cameras are shown: *MOS1* (black), *MOS2* (red), and *PN* data (green, with higher count-rate) as well as the contribution of each component of the best fit model (from left to right, white dwarf atmosphere, low temperature MEKAL, high temperature MEKAL and Gaussian emission line). (Image from Sala (2004a)).

lines can be emitted at higher energies by iron at intermediate states of ionization (Hellier, Mukai, & Osborne, 1998). The main fluorescent K$\alpha$ line emitted by cold, neutral iron could thus explain the emission line observed for V2487 Oph (Hernanz & Sala, 2002), while the blend with the other fluorescent lines could explain the width of the line. This fluorescent Fe K$\alpha$ line can only be induced by reflection of the X-rays generated in the hot post-shock region of the accretion flow on neutral iron, i.e., on colder material of the disk or the white dwarf. A reflection effect requires therefore that accretion had been reestablished by the time of observations.

The kind of spectra found for V2487 Oph is similar to observed for the intermediate polars EX Hya and AO Pisc (Ishida, Mukai, & Osborne (1994)); Hellier et al. (1996); Fujimoto & Ishida (1997)). Nevertheless, those cataclysmic variables had thermal plasma spectra stepper than V2487 Oph, indicating cooler plasmas in the accretion stream. The high temperatures in the shocked plasma may be a consequence of accretion onto a massive white dwarf, which would agree with the mass determination of Hachisu et al. (2002), $M_{WD} = 1.35\ \mathrm{M}_{\odot}$, from the visual light curve and the numerical model described in Hachisu et al. (2002).
Also, the parameters of the soft component of the spectrum indicate that it can not be

associated to the emission from the whole white dwarf surface, i.e., it can not be produced by hydrogen burning on the star's envelope and just only a fraction of the white dwarf surface is emitting soft X-rays, as observed for V2487 Oph. The presence of this soft component, typical of magnetic cataclysmic variables, also supports the surprisingly fast recovery of the accretion process as soon as $\sim 2.7$ years (less than 1000 days) after the nova outburst (Hernanz & Sala, 2002).

Ferri & Hernanz (2007) showed more spectral features in the V2487 Oph spectra through the re-analysis of the XMM-Newton data already presented in Hernanz & Sala (2002) and Sala (2004a) and the first study of optical observations performed in 2002. At least two other thermal lines in the $6-7$ keV region of these spectra were found, which were ascribed to the emitting plasma beside the fluorescence feature (see also Ferri (2011) for details). Thanks to the longer exposition they could present the first X-ray timing analysis, besides photometric and spectroscopic data obtained by them in the optical banda at the Roque de los Muchachos Observatory.

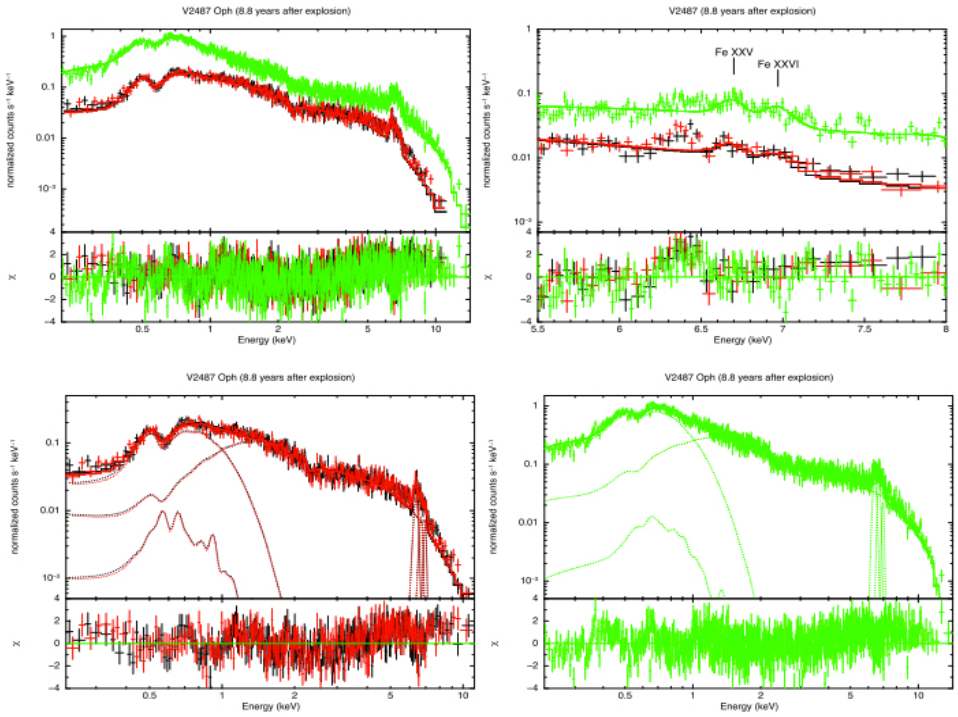


FIGURE 4.5: The *EPIC MOS1* (black), *MOS2* (red) and *PN* (green) data modelled with a black body component, a two-temperature MEKAL plasma model plus three Gaussian lines at $6.38\pm0.03$ keV, $6.70\pm0.03$ keV and $6.98^{+0.02}_{-0.06}$ keV (best fit model, left-upper panel), all with photoelectric absorption. Data in the $5-9$ keV energy range modelled with a MEKAL model at $kT \backsimeq 10$ keV on the right-upper panel is also presented, where the $6.68$ and $6.97$ keV thermal emission line (Fe XXV and Fe XXVI, respectively) can be noticed. Individual spectral components have been added (dashed lines) corresponding to *MOS1* and *MOS2* (left-lower panel) and *PN* (right-lower panel) data fitted with best fit model separately. In the lower part of each image the fit residuals in $\sigma$ units are presented (Image from Ferri (2011)).

Figure 4.5 shows the *MOS1*, *MOS2* and *PN* spectra data ($0.2 - 15$ keV) and the best-fit models, i.e. phabs $*$ [bbody + mekal + mekal + gauss + gauss + gauss], which is given by a discrete multi-temperature model composed by MEKAL (Mewe, Gronenschild, & van den Oord (1985); Mewe, Lemen, & Oord (1986)) components plus the black body contribution as the base for the model.

Nevertheless the method used to simulate the emission lines in order to obtain the best fit has been to model the continuum energy ranges $5.0 - 6.3$ and $7.1 - 10.0$ keV with the absorbed higher temperature MEKAL. Ferri (2011) fixed the continuum parameters, extended the fitted range to $5.0 - 10.0$ keV, and added a gaussian function to model the Fe lines complex and found that this part of the spectra could be modelled by three Gaussians considering each detector separately or altogether, corresponding to neutral, He-like and H-like K$\alpha$ iron emission. Thus Ferri (2011) constrained by fixing the line energies to 6.40, 6.68 and 6.97 keV, respectively, and forced the three lines to have the same width and peak energy in the whole spectrum.
Acceptable fits were achieved including two MEKAL components, a black body and interstellar absorption assuming that the absorption is uniform around the source, $N_H = 2.1 \times 10^{21}$ cm$^{-2}$, fixed to the value of Dickey & Lockman (1990). The parameters obtained by Ferri (2011) were $kT_{bbody} = 108^{+2}_{-5}$ eV, $kT_{min} = 0.2 \pm 0.1$ keV, at 1-$\sigma$ error, $kT_{max} \geq 77$ keV. Although this model gives a good $\chi^2_\nu = 1.4$, it does not provide a very good fit to the data. An emission at $6.38 \pm 0.03$ keV was also obtained corresponding to the Fe fluorescent line, $6.70 \pm 0.03$ keV for Fe XXV and $6.98^{+0.02}_{-0.06}$ keV for Fe XXVI K$\alpha$ iron line with equivalent widths ($EWs$) of 350, 210 and 100 eV, respectively (Hellier et al., 1996).
Also a partial covering absorption model, a black body plus a two-temperature optically thin thermal plasma, simulated with MEKAL, and only one gaussian line accounting for the Fe K$\alpha$ fluorescence line at 6.4 keV were include with the aim to improve the $\chi^2_\nu$. The model is given by phabs $*$ pcfabs $*$ (bbody + mekal + mekal + gauss).
Although the use of the partial covering absorber improves drastically the $\chi^2_\nu$, 1.2, this model shows residuals between 6.9 and 7 keV and it does not fit very well the Fe H-like emission line at 6.97 keV.

## 4.2 Observations and Analysis

### 4.2.1 XMM-Newton data

Table 4.1 contains the *XMM-Newton* detections of Nova Oph 1998. This nova was observed four times in the X-ray band during 2001 and 2002 with an interval of about 6 months between each two consecutive observations and a fifth observation in 2007. The counts rate and the total counts are calculated in the $0.2 - 10$ keV energy range for *MOS1* and *MOS2* and in the $0.2 - 12$ keV energy range for *PN*. The *PN* camera failed for 2001 February 25 observation, so that only the *MOS1* and *MOS2* data are available.

TABLE 4.1: Log of all the V2487 Oph 1998 detections with *XMM-Newton* satellite.

| Observation date | Days, years after outburst | Camera | Total (effective) exposure Time (s) | Total counts (cts) | Counts rate (cts/s) |
|---|---|---|---|---|---|
| Febr. 25, 2001 | 986 d, 2.7 yr | MOS1 | 7698 (7206) | 2162 | $0.30 \pm 0.01$ |
| | | MOS2 | 7700 (7238) | 2099 | $0.29 \pm 0.01$ |
| | | PN | - | - | - |
| Sept. 5, 2001 | 1178 d, 3.2 yr | MOS1 | 7598 (7494) | 2323 | $0.31 \pm 0.01$ |
| | | MOS2 | 7597 (7512) | 2329 | $0.31 \pm 0.01$ |
| | | PN | 5000 (5040) | 4563 | $1.05 \pm 0.01$ |
| Febr. 26, 2002 | 1352 d, 3.7 yr | MOS1 | 7032 (5699) | 1653 | $0.29 \pm 0.01$ |
| | | MOS2 | 7033 (5877) | 1763 | $0.30 \pm 0.01$ |
| | | PN | 4668 (4346) | 4563 | $1.05 \pm 0.02$ |
| Sept. 24, 2002 | 1559 d, 4.3 yr | MOS1 | 8278 (7549) | 2416 | $0.32 \pm 0.01$ |
| | | MOS2 | 8278 (7582) | 2502 | $0.33 \pm 0.01$ |
| | | PN | 6569 (5678) | 6189 | $1.05 \pm 0.01$ |
| Marc. 24, 2007 | 3212 d, 8.8 yr | MOS1 | 35289 (32984) | 12006 | $0.364 \pm 0.003$ |
| | | MOS2 | 35296 (32902) | 11779 | $0.358 \pm 0.003$ |
| | | PN | 33342 (30834) | 38759 | $1.242 \pm 0.006$ |

In this work, the study of the fourth and fifth observations[2], 4.3 and 8.8 years after outburst, of V2487 Oph carried out by the XMM-Newton satellite are presented. The *EPIC* cameras observed the nova for a total exposure time of 8280 with *MOS1* and *MOS2* and 6570 seconds with *PN* for the fourth observation; and 35290 seconds with *MOS1* and *MOS2* and 33340 seconds with *PN* for the fifth observation.

### 4.2.2 INTEGRAL data

In addition to the *XMM-Newton* observations, V2487 Oph was detected as a hard X-ray source in the *INTEGRAL IBIS/ISGRI* (Ubertini et al., 2003) soft gamma-ray Galactic Plane Survey, with an emission at $kT > 30$ keV (Barlow et al., 2006). Re-analyzing the data from 22 cataclysmic variables detected with the third *INTEGRAL/IBIS* survey Landi et al. (2009) confirmed previous indications about V2487 Oph. More recently V2487 Oph also appeared in the fourth *IBIS/ISGRI* soft Gamma-ray Survey Catalog (Bird et al., 2010).

Since V2487 Oph is in the plane of the mission, at least once per month was observed. The data reduction is courtesy of Stephane Paltani (private communication) and was reduced with the Offline Science Analysis, *OSA*, software version 8, following the standard reduction procedures (Goldwurm et al., 2003). *IBIS* spectra were extracted in 12 and 24 energy channels. However, it was necesssary added a step included in OSA 9, which consists in the detection and removal of pixels affected by the presence of glue in the mask. This glue is not completely transparent to X-rays, and the inclusion of these pixels leads to the presence of strong ghosts for the brightest sources. In this crowded area, this cleaning is absolutely mandatory.
The total good time is 2.5 Ms, while the efficiency-corrected exposure, taking into account vignetting, is 1.7 Ms. The data have been taken over 160 Ms, covering the *INTEGRAL* observations a bit more than 5 years. Revolutions go from 0046 to 0736. However, because of the large number of sources brighter than V2487 Oph in this area, it was necessary to select pointing where V2487 Oph was on the Eastern side, in order to avoid a too large number of bright sources in the Field of view, FOV, which makes the spectral extraction fail.

## 4.3 Spectral analysis

In order to obtain the basic parameters like the temperature of the black body, the interstellar absorption and the mass of the white dwarf and to obtain information about the soft and hard X-ray emission. The data was analysed with the software package *XSPEC* (Arnaud, 1996). For the analysis of the *EPIC* spectra, the tabulated models previously computed, `ipzk.fits` and `ipsd.fits`, have been used as an additive table model, ATABLE in *XSPEC*. The channels below 0.3 keV have been ignored because of inadequate

[2]ID observations: 0085582001 and 0401660101 corresponding to fourth and fifth observations, respectively; P.I.: Margarita Hernanz.

instrumental response.
A simple photoelectric absorption with Verner et al. (1996) cross sections and Lodders (2003) solar abundances is needed to simulate the effect of the hydrogen column density for the absorption component, PHABS in *XSPEC*. In our fit the interstellar absorption was set to the value obtained from the absorption calculated from the extinction derived by Lynch et al. (2000), from the color excess $E(B-V) = 0.38 \pm 0.08$. Through the empirical relationship between interstellar X-rays absorption and optical extinction, $N_H/E(B-V) = 5.9\times10^{21}$ mag$^{-1}$cm$^{-2}$, obtaining a value of $N_H = 2.2\times10^{21}$ cm$^{-2}$; which is consistent with the interstellar absorption $N_H = 2.1 \times 10^{21}$ cm$^{-2}$ (Dickey & Lockman, 1990). Also a black body component, BBODY available in *XSPEC*, have been used with the aim to fit the soft part of the spectrum of the Nova Oph 1998.
In some cases, Gaussian lines were added to the model to express the neutral, or low ionized, Fe K$\alpha$ emission line at 6.4 keV (Hernanz & Sala, 2002) and also the thermal plasma He-line Fe and H-line Fe emission detected by Ferri (2011).

The best fitting for both observations, 4th and 5th, of *XMM-Newton* and its combinations with *INTEGRAL* observations, in 12 and 24 energy channels, are presented below.

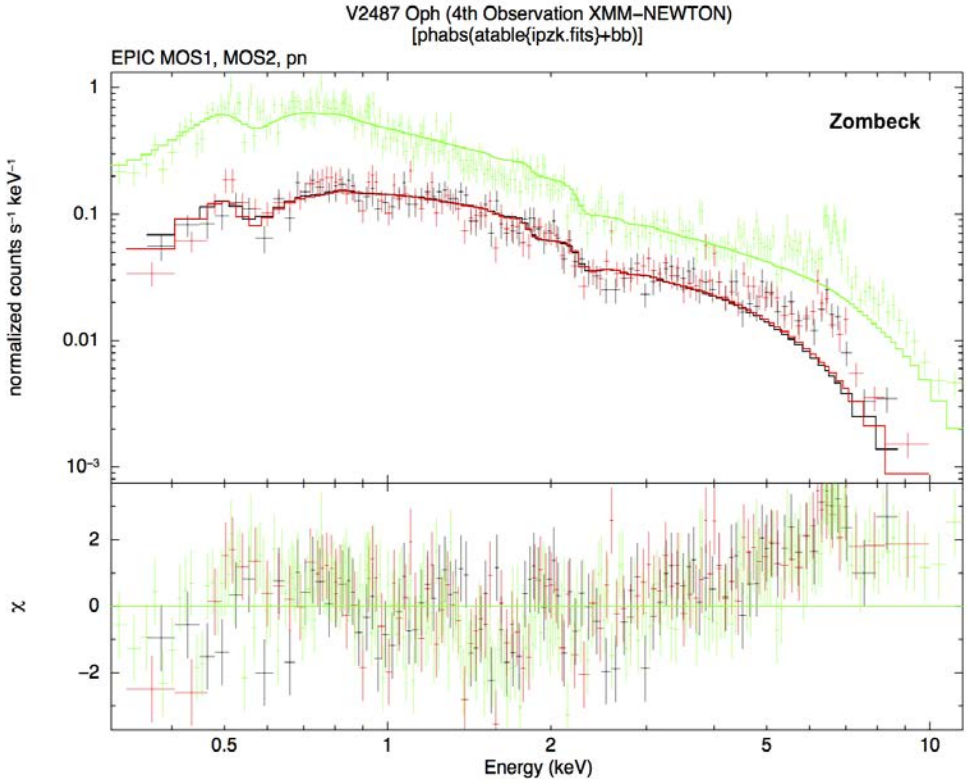


FIGURE 4.6: *XMM-Newton* 4th observation with *EPIC MOS1* (black), *MOS2* (red) and *PN* (green) using the cooling approximation of Zombeck. The black body component is $kT_{bbody} = 0.11$ keV, the white dwarf mass is obtained $M_{WD} = 1.4$ M$_\odot$ and the reduced chi-square is $\chi^2_\nu = 1.8$ for 463 degrees of freedom. The lower panel show the fit residuals in $\sigma$ units.

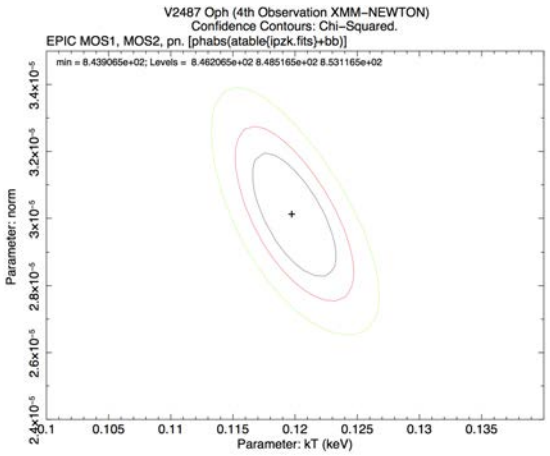


(A) Confidence contour for the black body temperature and the normalization.

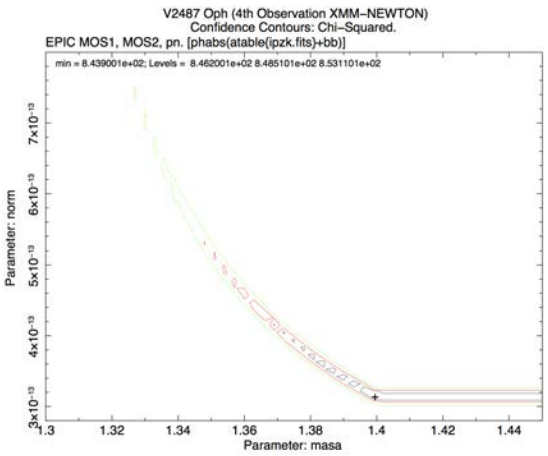


(B) Confidence contour for the mass of the white dwarf and the normalization.

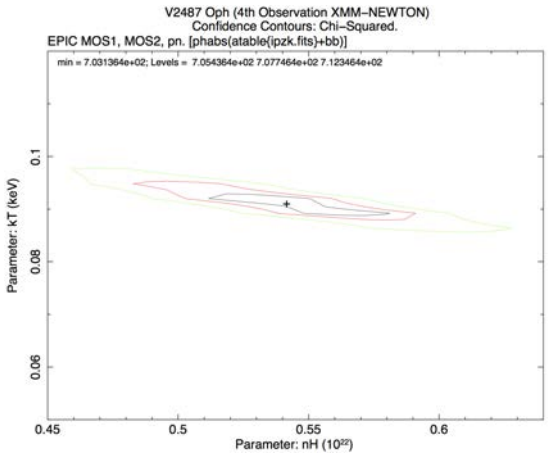


(C) Confidence contour for the black body temperature and $N_H$.

FIGURE 4.7: Confidence contours for the best fit model parameters. Inner, middle and outer circles represent $1\sigma$, $2\sigma$ and $3\sigma$ levels of confidence, respectively. The cross marks the best-fit position.

Figure 4.6 corresponds to the 4th observation with *XMM-Newton*, $4.3$ years after outburst, with *EPIC MOS1*, *MOS2* and *PN* cameras using the additive table model `ipzk.fits` obtained with the cooling expression of Zombeck. The best fit model is given by $[phabs * (atable\{ipzk.fits\}) + bbody]$ giving a $\chi^2_\nu = 1.8$. The interstellar absorption is fixed at $N_H = 2.2 \times 10^{21}$ cm$^{-2}$, however a higher absorption is obtained. The $kT_{bbody}$ calculated is $0.11$ keV, and the white dwarf mass is $M_{WD} = 1.4\,\mathrm{M}_\odot$. In order to evaluate the errors for every model component, confidence contours have been performed in Figures 4.7a, 4.7b and 4.7c.

As in Figure 4.6, fitting data have been obtained for the 4th observation but using the tabulated model `ipsd.fits` computed with the results of the cooling function obtained by Sutherland & Dopita. Figure 4.8 shows the best fit model obtaining a $\chi^2_\nu = 1.8$. The calculated values of $N_H$, $kT_{bbody}$ and $M_{WD}$ are similars to those obtained with the tabulated model with cooling approximation of Zombeck. In addition, the confidence contours,

Figures 4.9a to 4.9c, have been obtained in order to evaluate the errors of the different parameters of the models.

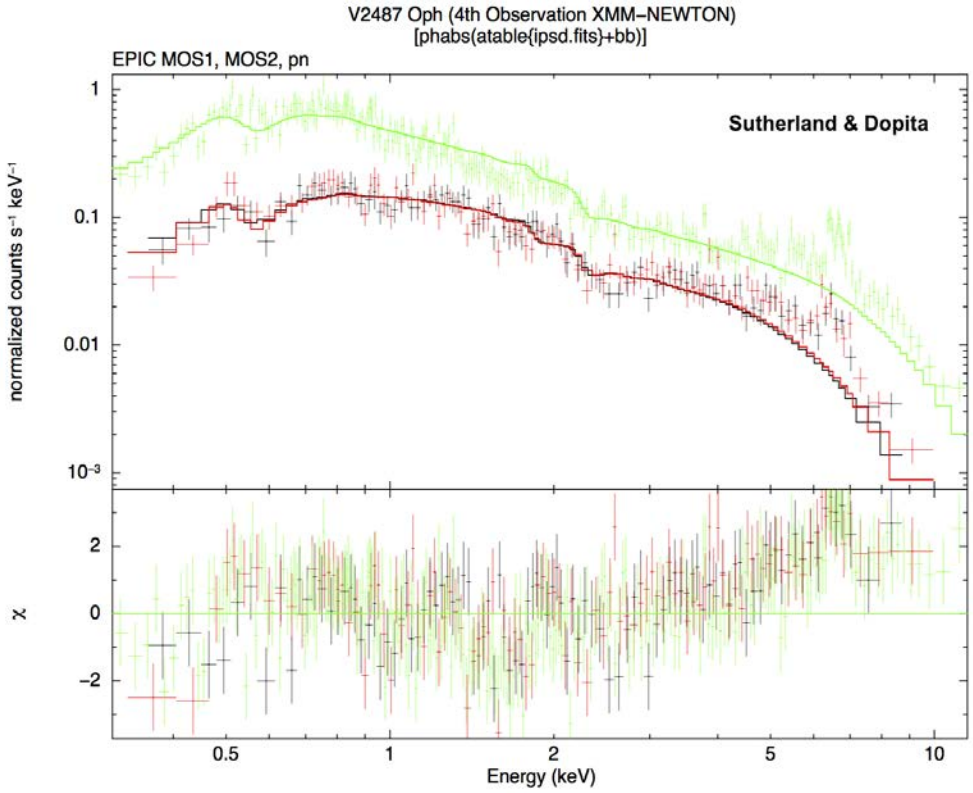


FIGURE 4.8: *XMM-Newton* 4th observation with *EPIC MOS1* (black), *MOS2* (red) and *PN* (green) using the cooling results of Sutherland & Dopita. The black body component is $kT_{bbody} = 0.11$ keV, the white dwarf mass is obtained $M_{WD} = 1.4\ \mathrm{M}_{\odot}$ and the reduced chi-square is $\chi^2_{\nu} = 1.8$ for 463 degrees of freedom. The lower panel show the fit residuals in $\sigma$ units.

The results obtained above suggest that an additional emission process should be involved beside bremsstrahlung in order to explain the whole X-rays line emission detected in the harder part of the spectra (Ferri, 2011).

Since our model does not include emission lines from the thermal plasma, we are not able to reproduce the entire emission lines using these models. The continuum shape of the data at harder energies, needs high temperature plasma values to obtain an acceptable fit for this region of the spectrum. However, because at that temperatures most of the atoms are ionized it prevents the production of emission line. To solve this problem, a Gaussian component is added to the spectrum to simulate the Fe complex line emission at higher energies. As high temperatures could produce iron K$\alpha$ lines from Fe XXV, or He-like at $6.68$ keV, and Fe XXVI, or H-like at $6.97$ keV also are included to the model with the fluorescent Fe K$\alpha$ line at $6.4$ keV.

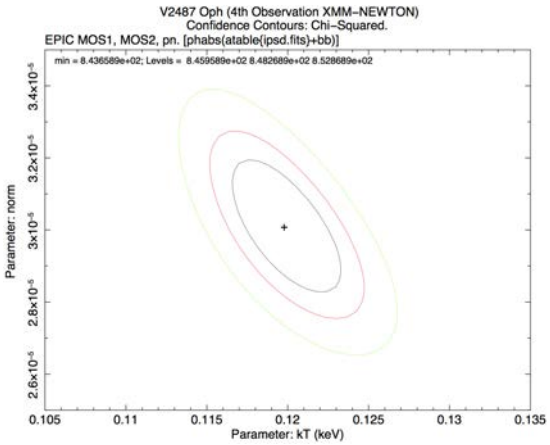


(A) Confidence contour for the black body temperature and the normalization.

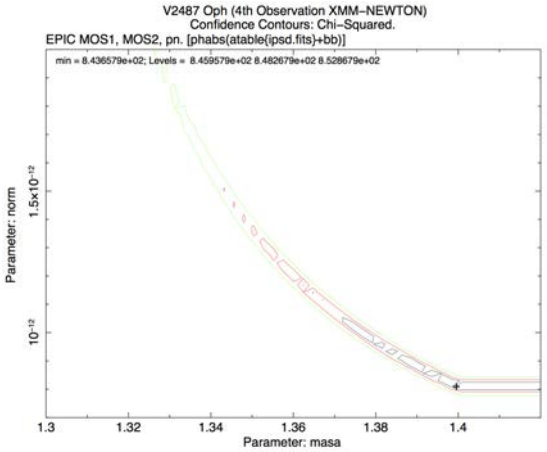


(B) Confidence contour for the mass of the white dwarf and the normalization.

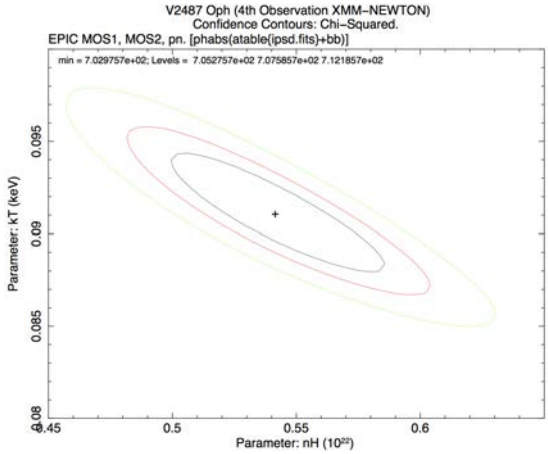


(C) Confidence contour for the black body temperature and $N_H$.

FIGURE 4.9: Confidence contours for the best fit model parameters. Inner, middle and outer circles represent $1\sigma$, $2\sigma$ and $3\sigma$ levels of confidence, respectively. The cross marks the best-fit position.

The new model is given by $[phabs*(atable\{ipzk.fits\})+bbody+3gauss]$. The absorption is initially $N_H = 2.2 \times 10^{21}$ cm$^{-2}$ but after fitting, the value obtained is higher, as in the last model, probably indicating that the source of the X-ray emission is more absorbed than by the interstellar medium alone and an intrinsic contribution from the binary system to the X-ray source is present. The black body temperature is $kT_{bbody} = 0.12$ keV and the white dwarf mass is computed as $M_{WD} = 1.39$ M$_\odot$. The $\chi^2_\nu$ is better than the obtained without considering the Fe lines and is $\chi^2_\nu = 1.3$. Figure 4.10 show the *EPIC* data with the new model and Figures 4.11a, 4.11b and 4.11c its corresponding confidence contours for the parameters of the model.

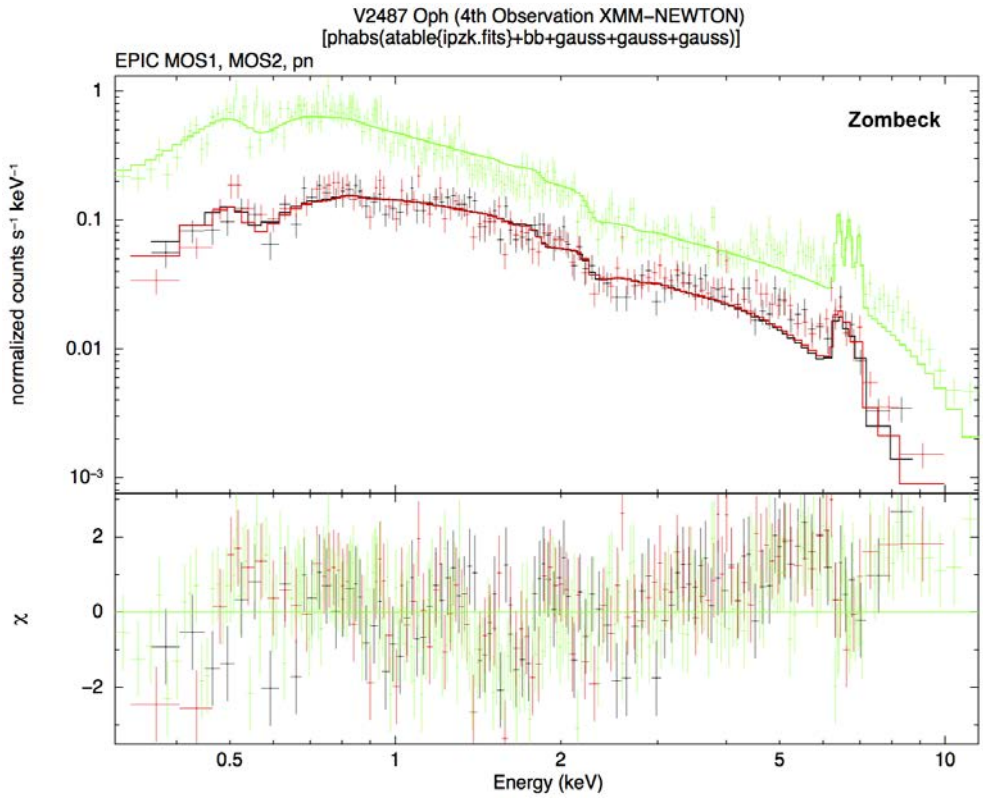


FIGURE 4.10: *XMM-Newton* 4th observation with *EPIC MOS1* (black), *MOS2* (red) and *PN* (green) using the cooling approximation of Zombeck. The black body component is $kT_{bbody} = 0.12$ keV, the white dwarf mass is obtained $M_{WD} = 1.39$ M$_\odot$ and the reduced chi-square is $\chi^2_\nu = 1.3$ for 460 degrees of freedom. The lower panel show the fit residuals in $\sigma$ units.

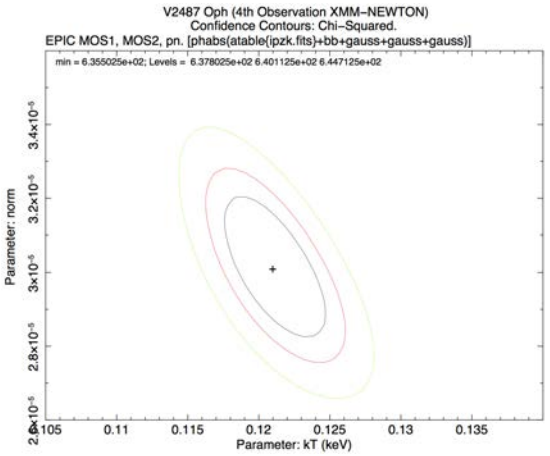


(A) Confidence contour for the black body temperature and the normalization.

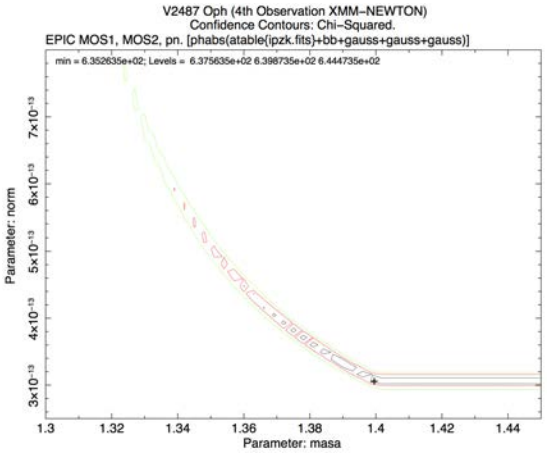


(B) Confidence contour for the mass of the white dwarf and the normalization.

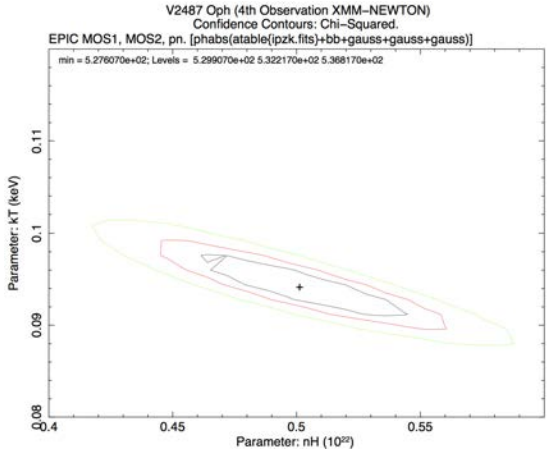


(C) Confidence contour for the black body temperature and $N_H$.

FIGURE 4.11: Confidence contours for the best fit model parameters. Inner, middle and outer circles represent $1\sigma$, $2\sigma$ and $3\sigma$ levels of confidence, respectively. The cross marks the best-fit position.

In addition to *XMM-Newton* observations, *INTEGRAL IBIS/ISGRI* spectra, extracted in 12 and 24 channels of energy, have been analyzed with the *EPIC* data. Figures 4.12 and 4.14 show the models that best fit the data from both satellites simultaneously. The model is the continuum bremsstrahlung model computed in this work and the interstellar absorption model, phabs, plus a black body spectra: $[phabs * (atable\{ipzk.fits\}) + bbody]$ and $[phabs * (atable\{ipsd.fits\}) + bbody]$ for tabulatd models `ipzk.fits` and `ipsd.fits`, respectively. Figures 4.13a, 4.13b, 4.13c, 4.15a, 4.15b and 4.15c are the corresponding confidence contours to evaluate the errors of the model parameters.

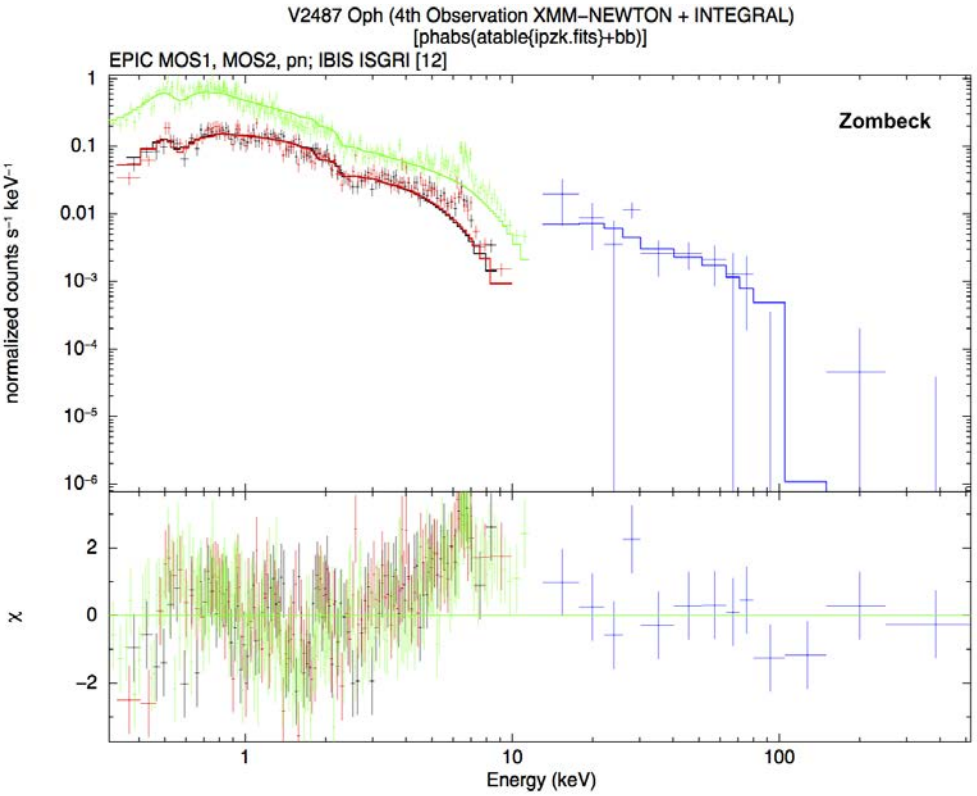


FIGURE 4.12: *XMM-Newton* 4th observation with *EPIC MOS1* (black), *MOS2* (red) and *PN* (green) and *INTEGRAL* observations *IBIS/ISGRI* (12 channels) (blue) using the tabulated model with cooling approximation of Zombeck. The black body component is $kT_{bbody} = 0.11$ keV, the white dwarf mass is obtained $M_{WD} = 1.39$ $M_\odot$ and the reduced chi-square is $\chi^2_\nu = 1.7$ for 476 degrees of freedom. The lower panel show the fit residuals in $\sigma$ units.

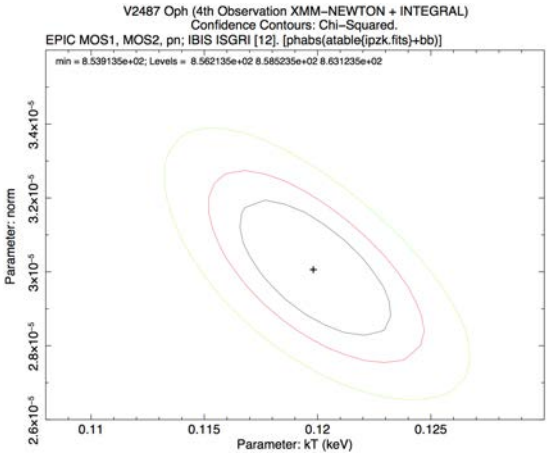


(A) Confidence contour for the black body temperature and the normalization.

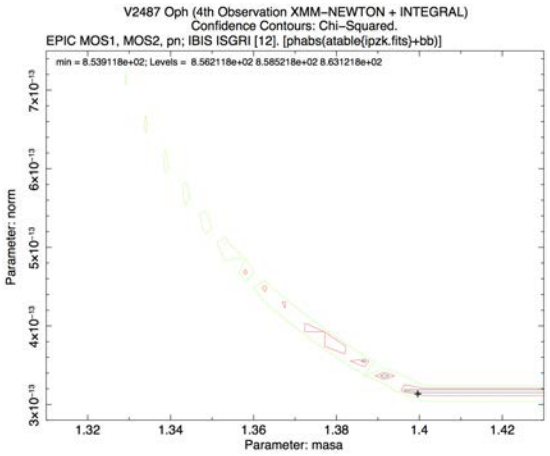


(B) Confidence contour for the mass of the white dwarf and the normalization.

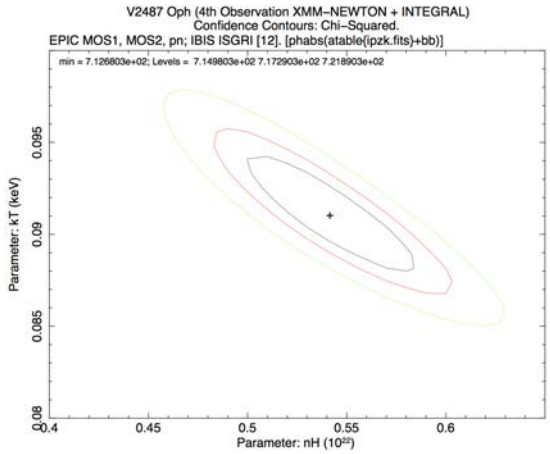


(C) Confidence contour for the black body temperature and $N_H$.

FIGURE 4.13: Confidence contours for the best fit model parameters. Inner, middle and outer circles represent $1\sigma$, $2\sigma$ and $3\sigma$ levels of confidence, respectively. The cross marks the best-fit position.

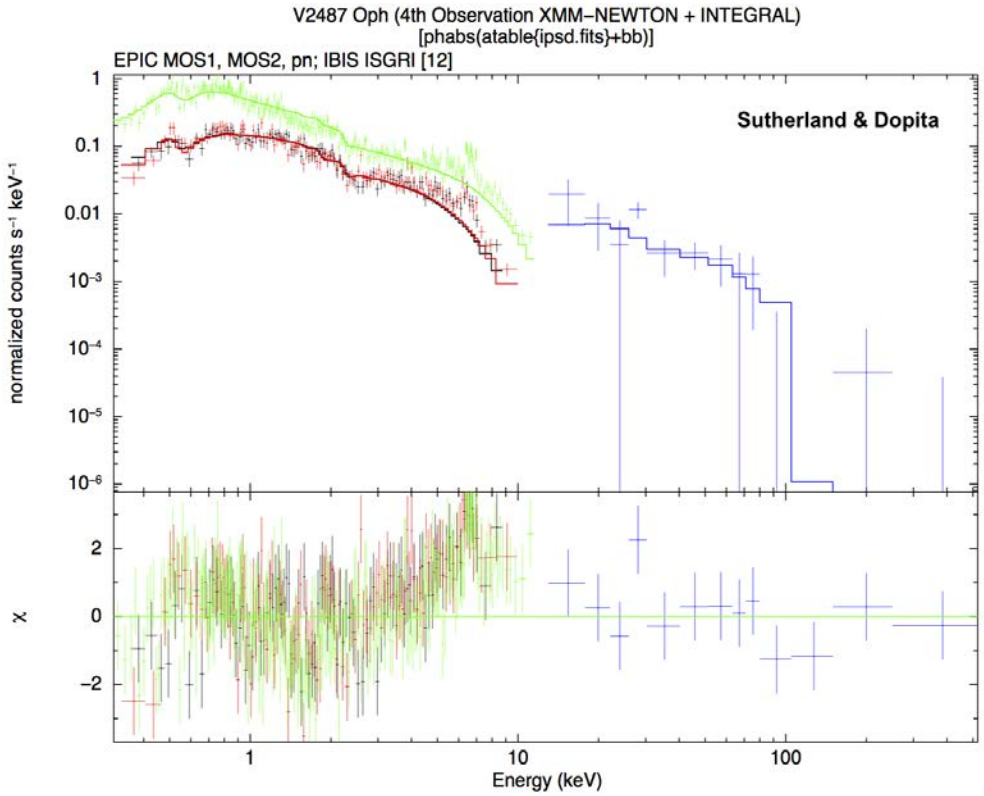


FIGURE 4.14: *XMM-Newton* 4th observation with *EPIC MOS1* (black), *MOS2* (red) and *PN* (green) and *INTEGRAL* observations *IBIS/ISGRI* (12 channels) (blue) using the tabulated model with cooling results of Sutherland & Dopita. The black body component is $kT_{bbody} = 0.11$ keV, the white dwarf mass is obtained $M_{WD} = 1.39\,\mathrm{M}_{\odot}$ and the reduced chi-square is $\chi^2_{\nu} = 1.7$ for 476 degrees of freedom. The lower panel show the fit residuals in $\sigma$ units.

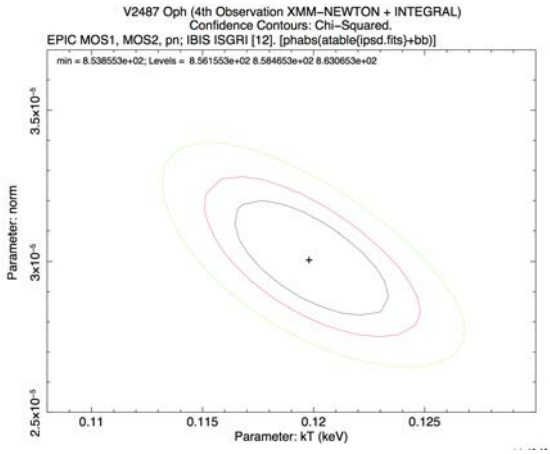


(A) Confidence contour for the black body temperature and the normalization.

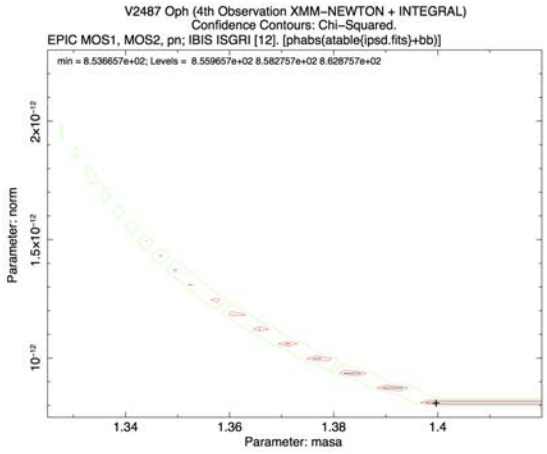


(B) Confidence contour for the mass of the white dwarf and the normalization.

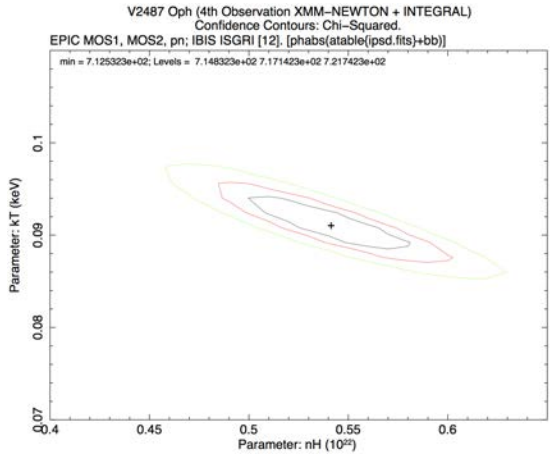


(C) Confidence contour for the black body temperature and $N_H$.

FIGURE 4.15: Confidence contours for the best fit model parameters. Inner, middle and outer circles represent $1\sigma$, $2\sigma$ and $3\sigma$ levels of confidence, respectively. The cross marks the best-fit position.

Figures 4.16 and 4.18 present the 5th observation with *XMM-Newton*, 8.8 years after outburst, and the *INTEGRAL* observations for the spectra extracted in 24 channels of energy. The model is the additive table model `ipzk.fits` or `ipsd.fits`, according to cooling approximation; with an interstellar absorption model and a gaussian line close to the value of the fluorescence Fe K$\alpha$ line, however, this gaussian line has not been set to a specific value. The interstellar absorption has been fixed initially as $N_H = 2.2 \times 10^{21}$ cm$^{-2}$ but, as in previous occasions, the absorption obtained is higher, $\sim 3.2 \times 10^{21}$ cm$^{-2}$, for both cases. The spectra display an iron emission line at $6.45$ keV corresponding to fluorescence Fe K$\alpha$. The chi-square obtained is $\chi^2_\nu = 1.27$ for both cases. The blackbody temperature, $kT_{bbody} = 0.10$ keV, is consistent with the expected value and the white dwarf mass is close to the Chandrasekhar limit $1.39$ M$_\odot$. The corresponding confidence contours are presented in Figures 4.17a, 4.17b and 4.17c for the tabulated model with the bremmstrahlung approximation of Zombeck and, in Figures 4.19a, 4.19b and 4.19c for the results of the cooling function of Sutherland & Dopita.

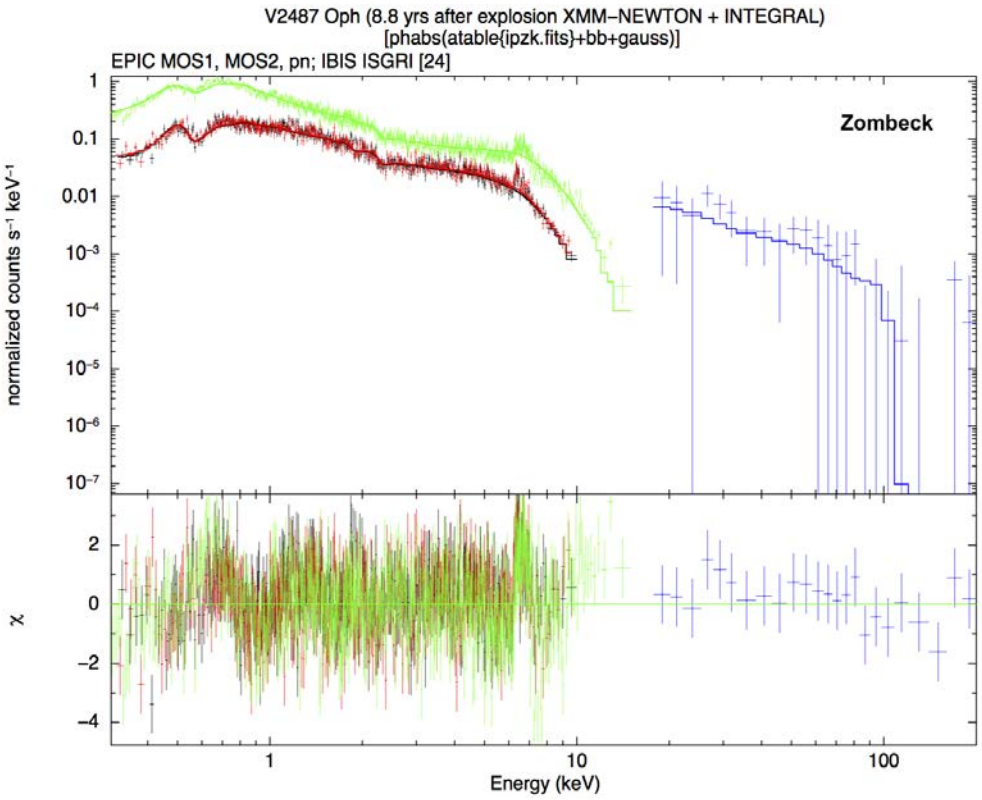


FIGURE 4.16: *XMM-Newton* 5th observation with *EPIC MOS1* (black), *MOS2* (red) and *PN* (green) and *INTEGRAL* observations *IBIS/ISGRI* (24 channels) (blue) using the tabulated model with cooling results of Zombeck. The black body component is $kT_{bbody} = 0.10$ keV, the white dwarf mass is obtained $M_{WD} = 1.39$ M$_\odot$ and the reduced chi-square is $\chi^2_\nu = 1.27$ for 1588 degrees of freedom. The lower panel show the fit residuals in $\sigma$ units.

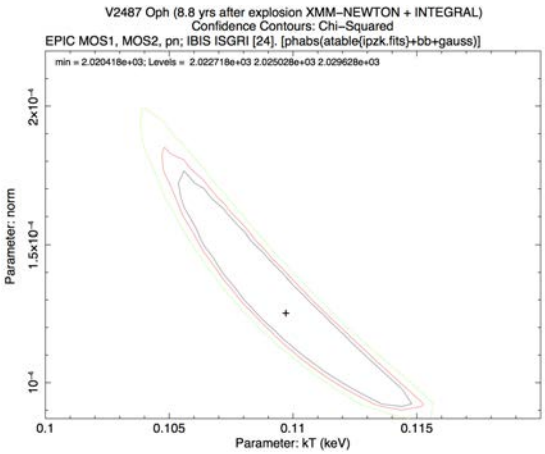


(A) Confidence contour for the black body temperature and the normalization.

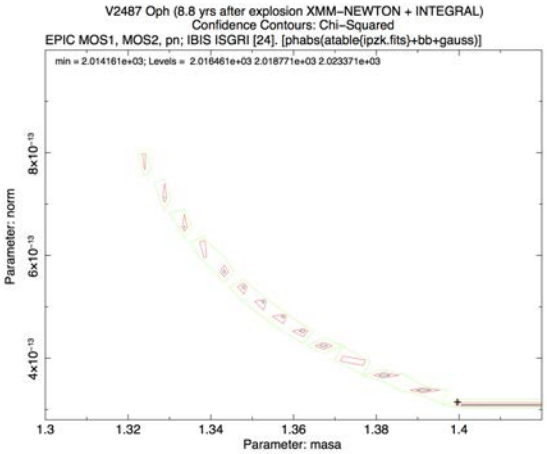


(B) Confidence contour for the mass of the white dwarf and the normalization.

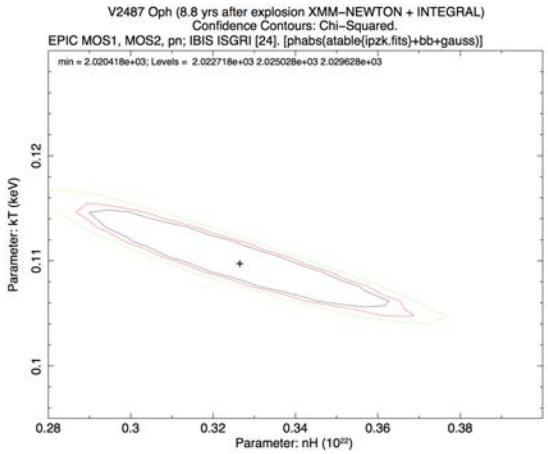


(C) Confidence contour for the black body temperature and $N_H$.

FIGURE 4.17: Confidence contours for the best fit model parameters. Inner, middle and outer circles represent $1\sigma$, $2\sigma$ and $3\sigma$ levels of confidence, respectively. The cross marks the best-fit position.

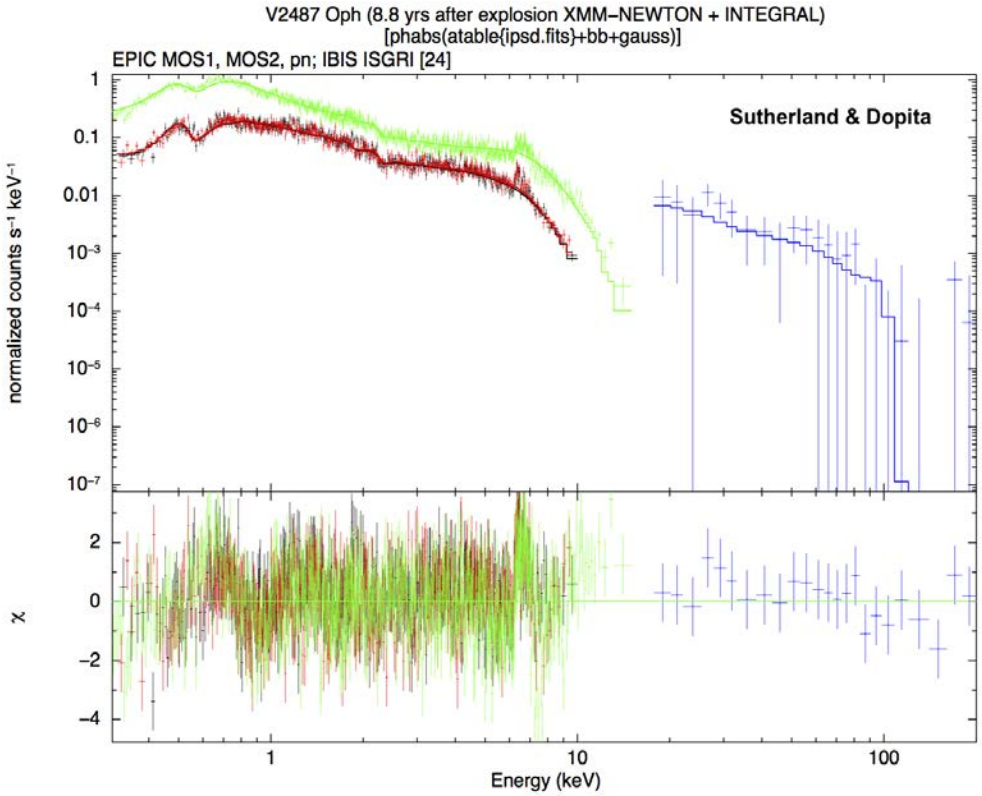


FIGURE 4.18: *XMM-Newton* 5th observation with *EPIC MOS1* (black), *MOS2* (red) and *PN* (green) and *INTEGRAL* observations *IBIS/ISGRI* (24 channels) (blue) using the tabulated model with cooling results of Sutherland & Dopita. The black body component is $kT_{bbody} = 0.10$ keV, the white dwarf mass is obtained $M_{WD} = 1.39\ \mathrm{M}_{\odot}$ and the reduced chi-square is $\chi^2_{\nu} = 1.27$ for 1588 degrees of freedom. The lower panel show the fit residuals in $\sigma$ units.

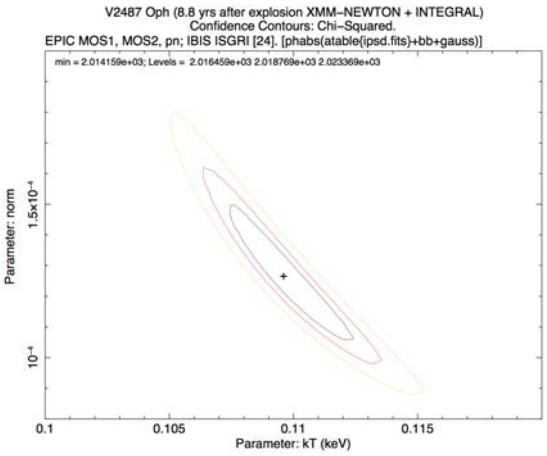


(A) Confidence contour for the black body temperature and the normalization.

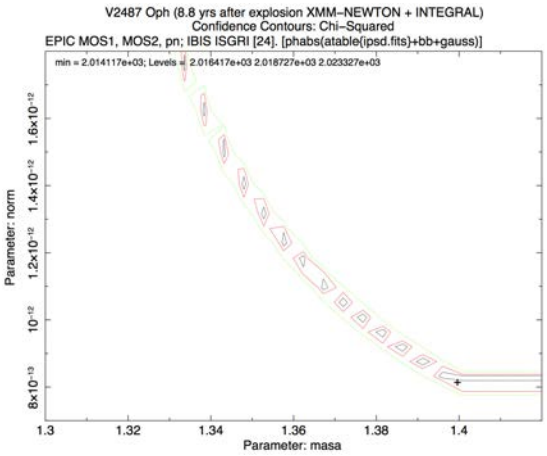


(B) Confidence contour for the mass of the white dwarf and the normalization.

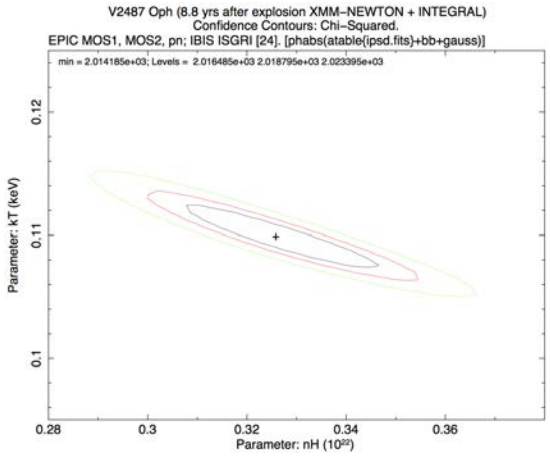


(C) Confidence contour for the black body temperature and $N_H$.

FIGURE 4.19: Confidence contours for the best fit model parameters. Inner, middle and outer circles represent $1\sigma$, $2\sigma$ and $3\sigma$ levels of confidence, respectively. The cross marks the best-fit position.

In order to improve the fit, we have also included three Gaussian lines, corresponding to the iron emission lines; at $6.4$ keV corresponding to fluorescence Fe K$\alpha$, and thermal plasma He-like and H-like emission. The new model is given by $[phabs*(atable\{ipzk.fits\})+bbody+3gauss]$ for the tabulated model with the bremsstrahlung approximation of Zombeck and $[phabs*(atable\{ipsd.fits\})+bbody+3gauss]$ for the model with the cooling function given by Sutherland & Dopita. figures 4.20 and 4.22 shows the *XMM-Newton-EPIC* and *INTEGRAL-IBIS* observations for the Nova Oph 1998 and the fitted models. The iron lines have been fixed to $6.4$, $6.68$ and $6.97$ keV. Also, the interstellar absorption has been fixed to $N_H = 2.2 \times 10^{21}$ cm$^{-2}$. The black body temperature, in both cases, is $kT_{bbody} = 0.11$ keV but the $\chi^2_\nu$ is higher, $1.8$ for 1589 degrees of freedom, than the obtained before. Probably because the differences in the absorption. Figures 4.21a, 4.21b and 4.21c are the confidence contours for the fitted models with cooling approximation of Zombeck and Figures 4.23a, 4.23b and 4.23c are the confidence contours for the cooling results of Sutherland & Dopita.

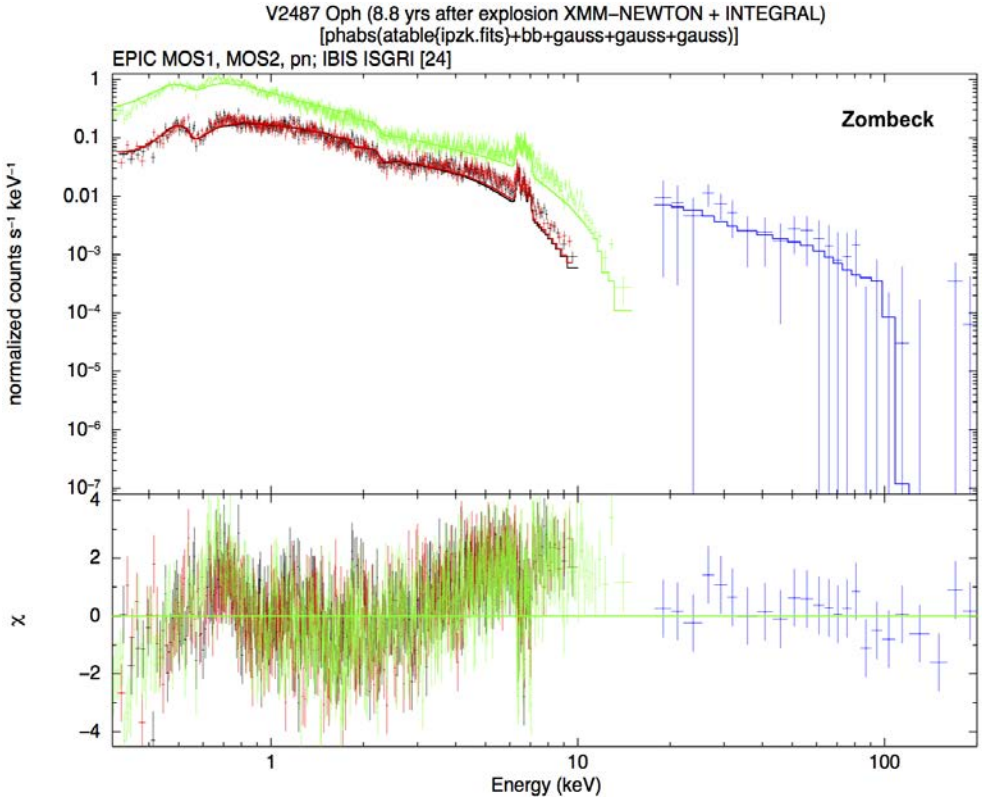


FIGURE 4.20: *XMM-Newton* 5th observation with *EPIC MOS1* (black), *MOS2* (red) and *PN* (green) and *INTEGRAL* observations *IBIS/ISGRI* (24 channels) (blue) using the tabulated model with cooling approximation of Zombeck. The black body component is $kT_{bbody} = 0.11$ keV, the white dwarf mass is obtained $M_{WD} = 1.4$ M$_\odot$ and the reduced chi-square is $\chi^2_\nu = 1.8$ for 1589 degrees of freedom. The lower panel show the fit residuals in $\sigma$ units.

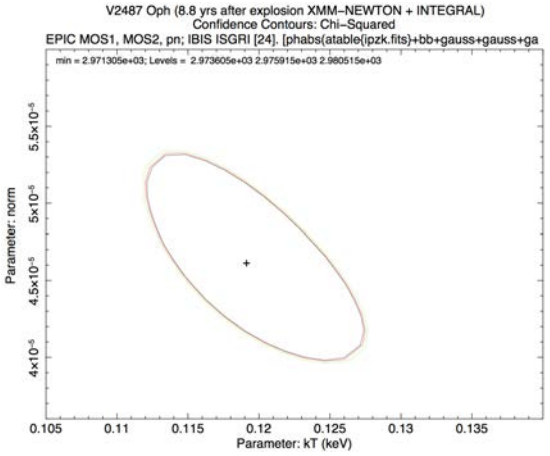


(A) Confidence contour for the black body temperature and the normalization.

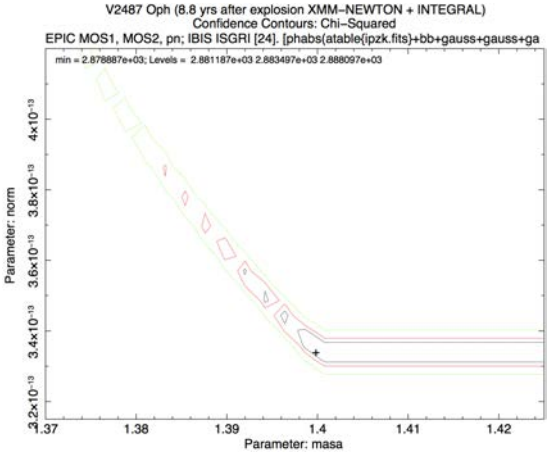


(B) Confidence contour for the mass of the white dwarf and the normalization.

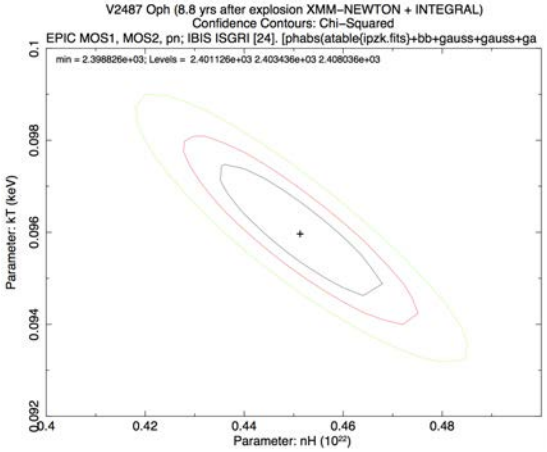


(C) Confidence contour for the black body temperature and $N_H$.

FIGURE 4.21: Confidence contours for cooling Zombeck. The contours shown are for one, two and three sigma. The cross marks the best-fit position.

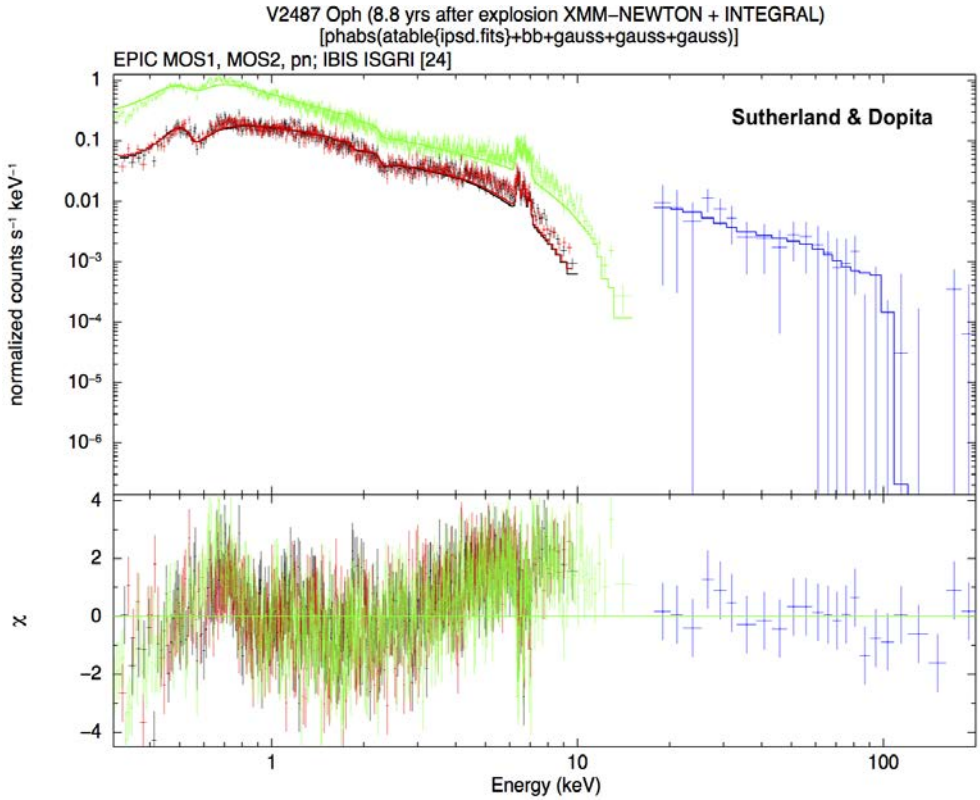


FIGURE 4.22: *XMM-Newton* 5th observation with *EPIC MOS1* (black), *MOS2* (red) and *PN* (green) and *INTEGRAL* observations *IBIS/ISGRI* (24 channels) (blue) using the tabulated model with cooling results of Sutherland & Dopita. The black body component is $kT_{bbody} = 0.11$ keV, the white dwarf mass is obtained $M_{WD} = 1.4\ \mathrm{M}_{\odot}$ and the reduced chi-square is $\chi^2_{\nu} = 1.8$ for 1589 degrees of freedom. The lower panel show the fit residuals in $\sigma$ units.

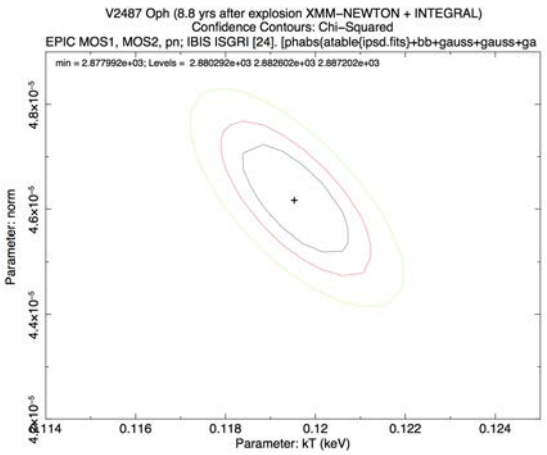


(A) Confidence contour for the black body temperature and the normalization.

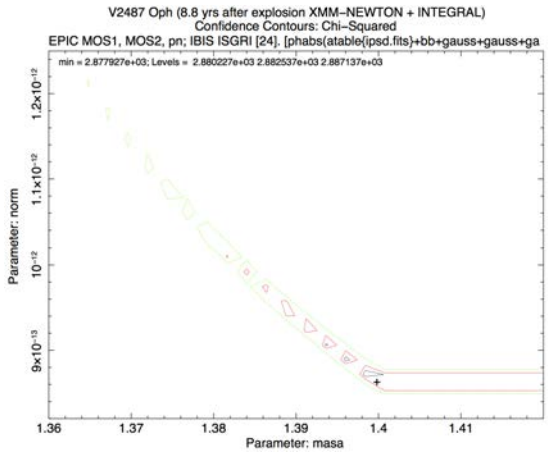


(B) Confidence contour for the mass of the white dwarf and the normalization.

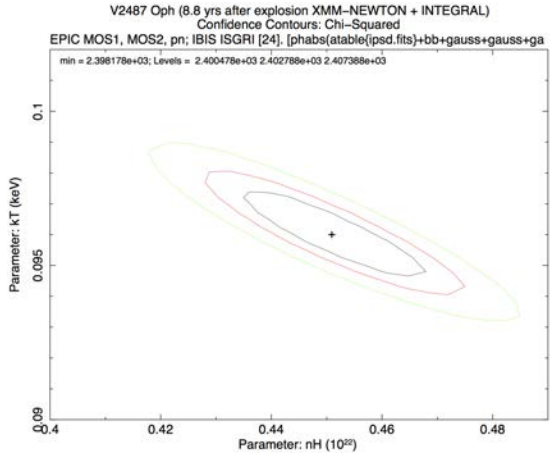


(C) Confidence contour for the black body temperature and $N_H$.

FIGURE 4.23: Confidence contours for cooling Sutherland & Dopita. The contours shown are for one, two and three sigma. The cross marks the best-fit position.

## 4.4 White dwarf mass estimation

The white dwarf mass is a fundamental parameter in cataclysmic binary. It not only governs the dynamics of the orbital motion and the accretion flow, but also is a main parameter characterizing the emission of the accretion region. Moreover, it plays a fundamental role in the binary evolution, and accurate mass distributions of certain sub-classes can help in constraining the accretion history.

As mentioned before, one method to obtain the mass of the white dwarf in magnetic cataclysmic variables is through their hard X-ray spectra. In order to derive the white mass estimated we fitted the model presented in this work to the *XMM-Newton-EPIC* and *INTEGRAL-IBIS* data of the Nova Oph 1998. Since the X-ray spectrum depends primarily on the white mass, using the tabulated model we are able to determine directly an estimate,and its uncertainty, of the white dwarf mass.

From the fitting of the models, the white dwarf mass is estimated between $M_{WD} = 1.39$ $M_\odot$ and $M_{WD} = 1.40$ $M_\odot$ which is a higher value than the estimated by Hachisu et al. (2002), $M_{WD} = 1.35$ $M_\odot$. However, it is consistent with what was expected for this white dwarf.
In order to determine the error in the estimation of the mass, confidence contours have been obtained.

As shown in Figures 4.7b, 4.9b, 4.11b and similars, the estimate of the error mass does not seem to be good. However, since this anomaly was present in all mass confidence contours, we explored what was happening with the calculation of the mass error. For this, synthetic spectra were created from the tabulated models (only the case of the Zombeck cooling approximation was used). Two spectra were created, one for a white dwarf of mass $M_{WD} = 1.15$ $M_\odot$ and another for a mass of $M_{WD} = 1.40$ $M_\odot$. The second value of the mass of the white dwarf was chosen because it is a similar value (in some cases, even equal) to the value obtained for V2487 Oph.
Since the method used for determining the "best-fit" model in *XSPEC* is defined as:

$$\chi^2 = \sum \frac{(C(I) - C_p(I))^2}{(\sigma(I))^2} \tag{4.1}$$

where $\sigma(I)$ is the error. A poissonian noise has been added to the synthetic spectra.

Once the synthetic spectra were created, the tabulated model `ipzk.fits` and an absorption model, PHABS ($N_H = 0$), were fitted to the synthetic observations[3]. Figure 4.24 shows the syntethic spectrum for a white dwarf mass of $1.15$ $M_\odot$ and poissonian noise.

The best fit model for the synthetic spectrum for a white dwarf mass of $M_{WD} = 1.15$ $M_\odot$ gives a mass of $1.14756$ $M_\odot$, which is very close to the real value. The confidence contour for the white dwarf mass and its normalization is shown in Figure 4.25.

[3] [phabs ∗ (atable{ipzk.fits})]

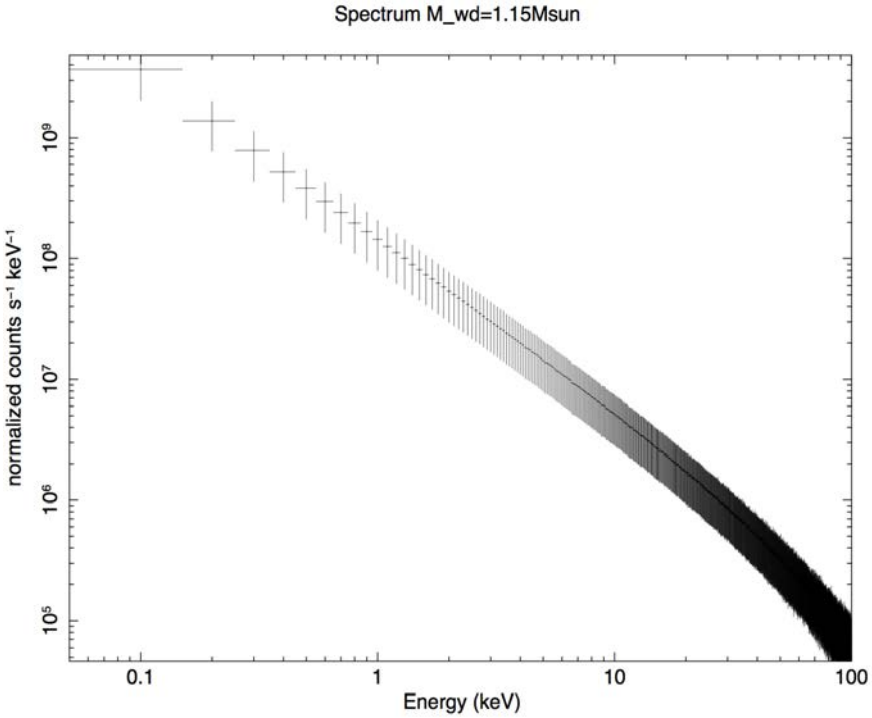


FIGURE 4.24: Synthetic spectrum for a white dwarf mass of $1.15M_{\odot}$ and poissonian noise.

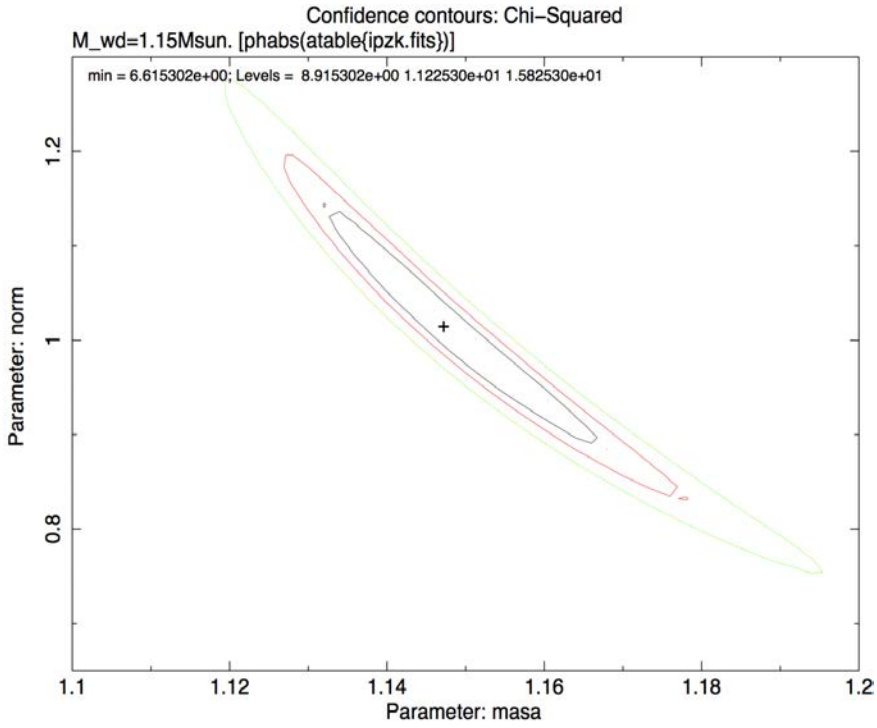


FIGURE 4.25: Confidence contour for synthetic spectrum of $M_{WD} = 1.15M_{\odot}$ (Figure 4.24). The contours shown are for one, two and three sigma. The cross marks the best-fit position.

As in Figure 4.24 and 4.25. The spectrum and confidence contour for the mass are shown for a white mass dwarf of $M_{WD} = 1.4M_{\odot}$ whose value is the upper limit of white dwarf

mass of the model.

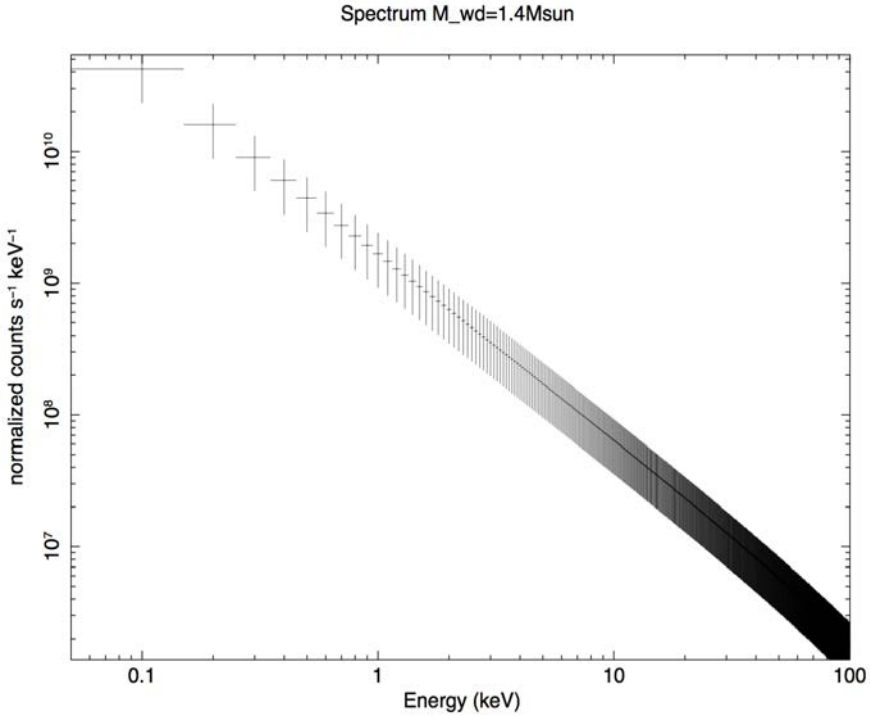


FIGURE 4.26: Synthetic spectrum for a white dwarf mass of $1.4M_{\odot}$ and poissonian noise.

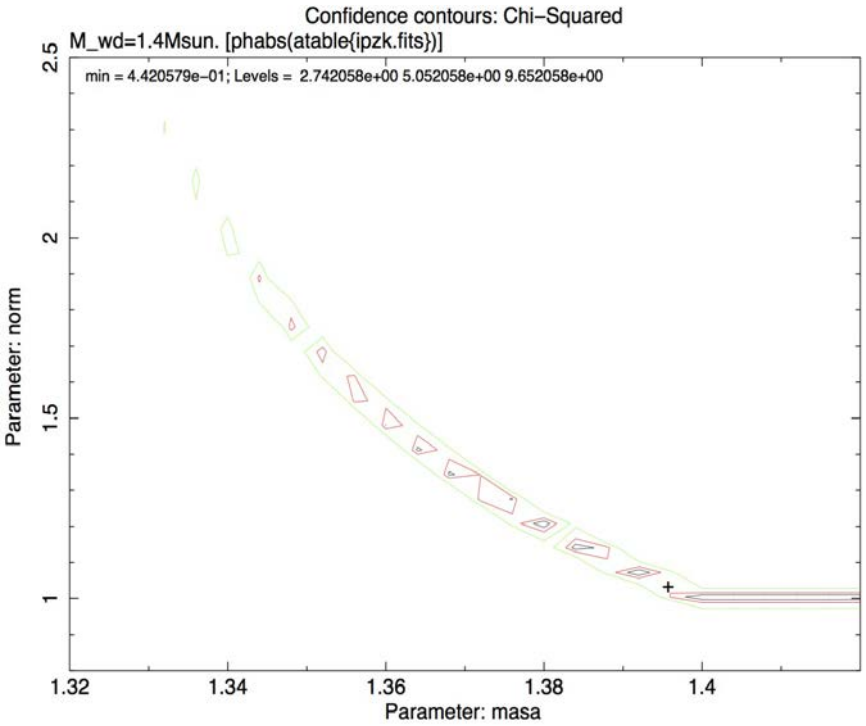


FIGURE 4.27: Confidence contour for synthetic spectrum of $M_{WD} = 1.4M_{\odot}$ (Figure 4.26). The contours shown are for one, two and three sigma. The cross marks the best-fit position.

The value obtained for the mass is $M_{WD} = 1.39603 M_{\odot}$, which is in agreement with the value of the mass, $M_{WD} = 1.4 M_{\odot}$. However, the confidence contours present the same anomaly as those obtained for the nova V2487 Oph, this indicates that this anomaly present in the contours is due to the fact that *XSPEC* can not adequately calculate the error of the mass of the white dwarf, since the value obtained for the masses is one of the limits (upper or lower) of the model. Nevertheless, despite this anomaly in the contours, the value obtained for the mass of the white dwarf is correct. This allows us to conclude that the value obtained from the masses of the white dwarf of V2487 Oph is correct, despite the contours that are obtained.

# 5

# CONCLUSIONS

In this thesis, we have investigated the emission region of accreting white dwarfs by the numerical solution of the hydrodynamical differential equations. Based on the calculated post shock accretion column structure involving the change of the accretion rate, and usgin different approximations for bremsstrahlung cooling emission, we present a spectral model of the accretion column. Furthermore, we have applied the model to the *XMM-Newton* and *INTEGRAL* observations of the Nova Oph 1998.

The hydrodynamic calculations presented in this thesis have allowed us to characterize the emission region through its main physical quantities, temperature, density, pressure and velocity and also to obtain the position of the shock. These physical quantities have been obtained for *(1)* different masses and *(2)* different accretion rates and have been compared with other approximations computed by different authors. We also improve the computational method with the aim to improve the determination of the shock height. By the boundary condition, the velocity is close to zero in the white dwarf surface increasing from there off. It reaches the largest value in the shock position. In the same way, the temperature reachs its maximum value at the shock. On the contrary, the density increases as we approach to the white dwarf surface as well as the pressure.
In order to determine the influence of the mass of the white dwarf the profiles of the physical quantities have been obtained for different white dwarf masses. For higher masses, the gas velocity at the shock becomes higher, and therefore the gas density falls for a given accretion rate. This causes a decrease in the plasma cooling rate, yielding higher shock heights.
In the same way, the influcence of the accretion rate have been examined. Calculations

with different accretion rates have been performed. The emission region extends upwards with a lower local mass accretion rate, $a$, i.e., the height of the shock is evidently proportional to $a^{-1}$. When the local mass accretion rate is sufficiently high, the density increases towards the white dwarf surface. Moreover, the temperature shows a peak in the middle of the emission region. At low enough local mass accretion rate, the temperature increase as local mass accretion rate increase. But, for a higher $a$, the temperature starts to decrease inward the white dwarf surface.

Since the emitted flux depends on the temperature and density, it is possible to obtain the spectrum from these quantities. Because more massive white dwarfs have smaller radii, the corresponding shock temperatures are higher and a higher temperature implies a hotter emission region, and hence a harder X-ray spectrum is observed. For less massive white dwarfs the maximum of the spectrum is obtained at lower energies. Since the local mass accretion rate alters the temperature and density profiles, the X-ray spectra also depend on the specific accretion rate. The continuum radiated by bremsstrahlung generally reduces as $a$ decreases, because the accretion column becomes cooler and the maximum temperature downs.

The model was applied to X-ray observations of Nova Oph 1998. As already was demostrated by Hernanz & Sala (2002), the accretion have been reestablished on the cataclysmic variable less than 100 days after outburst. Since the cataclysmic variable hosting the nova was also detected before the outburst by *ROSAT* All Sky Survey, V2487 Oph is the first nova detected in X-rays before and after the outburst and supports the cataclysmic variable scenario for classical novae (Hernanz & Sala, 2002).

Observations in X-rays show that V2487 Oph exhibits characteristics of Intermediate Polars and indicated that the white dwarf should be magnetic. As the spectrum is dominated by thermal plasma emission, a thermal bremsstrahlung continuum was applied with an absorption model and plus a black body component. As indicated Hernanz & Sala (2002) and Ferri & Hernanz (2007), the spectra display an emission at $6.4$ keV corresponding to the Fe fluorescent line and thermal plasma He-like and H-like emission at $6.68$ keV and $6.97$ keV, respectively.
Hachisu et al. (2002) through optical studies of the light curve, indicate that the white dwarf of this nova is quite massive, $M_{WD} = 1.35$ M$_\odot$, which is in agreement with the recurrent nature of V2487 Oph and with the white dwarf mass obtained from the X-ray spectra in this work: $M_{WD} = (1.39 - 1.40)$M$_\odot$. Although the mass of the white dwarf has been determined with good precision, it would be advisable to include emission lines to the model in order to improve the fit. In additon, it has been indicated the possibility of including a more modern cooling function, for example, computed by the code *APEC* (Smith et al., 2001) using the database *AtomDB*[1] (Foster et al. (2011); Foster et al. (2012)).

[1] http://www.atomdb.org/

# BIBLIOGRAPHY


Aizu K. 1973, *X-Ray Emission Region of a White Dwarf with Accretion*, Progress of Theoretical Physics, **49,**(4), 1184–1194. ISSN: 0033-068X. DOI: 10.1143/PTP.49.1184. URL: http://adsabs.harvard.edu/abs/1973PThPh..49.1184A.

Anzolin G. 2008, *Two new intermediate polars with a soft X-ray component*, *A&A*, **489,** 1243–1254. DOI: 10.1051/0004-6361:200810402. arXiv: 0808.1499.

Anzolin G. 2009, *Broad-band properties of the hard X-ray cataclysmic variables IGR J00234+6141 and 1RXS J213344.1+510725*, *A&A*, **501,** 1047–1058. DOI: 10.1051/0004-6361/200911816. arXiv: 0905.1080 [astro-ph.SR].

Arnaud K. A. 1996, *XSPEC: The First Ten Years*, *Astronomical Data Analysis Software and Systems V*, *A.S.P. Conference Series*. Ed. by J. Jacoby, G.H. and Barnes. **101,** p. 17–20. URL: http://adsabs.harvard.edu/abs/1996ASPC..101...17A.

Barlow E. J. 2006, *20-100 keV properties of cataclysmic variables detected in the INTEGRAL/IBIS survey*, *MNRAS*, **372,** 224–232. DOI: 10.1111/j.1365-2966.2006.10836.x. eprint: astro-ph/0607473.

Beardmore A. P. Osborne J. P. And Hellier C, 2000, *The multi-temperature X-ray spectrum of the intermediate polar V1223 Sagittarii*, Monthly Notices of the Royal Astronomical Society, **315,**(2), 307–315. ISSN: 0035-8711. DOI: 10.1046/j.1365-8711.2000.03477.x. URL: http://adsabs.harvard.edu/abs/2000MNRAS.315..307B.

Bernardini F. 2014, *Swift J2218.4+1925: a new hard-X-ray-selected polar observed with XMM-Newton*, *MNRAS*, **445,** 1403–1411. DOI: 10.1093/mnras/stu1819. arXiv: 1409.2257 [astro-ph.HE].

Bird A. J. 2010, *The Fourth IBIS/ISGRI Soft Gamma-ray Survey Catalog*, *Astrophys. J. Suppl.*, **186,** 1–9. DOI: 10.1088/0067-0049/186/1/1. arXiv: 0910.1704 [astro-ph.HE].

Brunschweiger J. 2009, *Intermediate polars in the Swift/BAT survey: Spectra and white dwarf masses*, Astronomy & Astrophysics, **127,**(1), 8. ISSN: 00046361. DOI: 10.1051/0004-6361/200811285. arXiv: arXiv:0901.3562v1. URL: http://arxiv.org/abs/0901.3562.

Burwitz V. 1996, *A new soft intermediate polar: RX J0512.2-3241 in Columba*, *A&A*, **310,** L25–L28.

Butters O. W. 2011, *RXTE and XMM observations of intermediate polar candidates*, *A&A*, **526,** A77, A77. DOI: 10.1051/0004-6361/201015848. arXiv: 1011.5762 [astro-ph.SR].

Canalle J. B. G. 2005, *Accretion in dipole magnetic fields: flow structure and X-ray emission of accreting white dwarfs*, Astronomy and Astrophysics, **440,** 185–198. DOI: 10.1051/0004-6361:20052706. URL: http://adsabs.harvard.edu/abs/2005A{\%}26A...440..185C.

Cash J, and Karp A. 1990, *A variable order Runge-Kutta method for initial value problems with rapidly varying right-hand sides*, ACM Trans. Math. Softw., **16,**(3), 201–222. ISSN: 00983500. DOI: 10.1145/79505.79507. URL: http://www.elegio.it/mc2/rk/doc/p201-cash-karp.pdf.

Chandrasekhar S. 1931, *The maximum mass of ideal white dwarfs*, Journal of Astrophysics and Astronomy, **74,** 81. DOI: 10.1086/143324. URL: http://adsabs.harvard.edu/abs/1931ApJ....74...81C.

Chanmugam G, Langer S. H. And Shaviv G. 1985, *Time-dependent accretion onto magnetic white dwarfs-Effects of cyclotron emission*, The Astrophysical Journal, **299,** L87–L91. DOI: 10.1086/184586. URL: http://adsabs.harvard.edu/full/1985ApJ...299L..87C.

Chevalier R. A. And Imamura J. N. 1982, *Linear analysis of an oscillatory instability of radiative shock waves*, The Astrophysical Journal, **261,** 543. ISSN: 0004-637X. DOI: 10.1086/160364. URL: http://adsabs.harvard.edu/abs/1982ApJ...261..543Chttp://adsabs.harvard.edu/doi/10.1086/160364.

Cropper M. 1990, *The Polars*, Space Science Reviews, **54,**(0038-6308), 195–295. DOI: 10.1007/BF00177799. URL: http://adsabs.harvard.edu/abs/1990SSRv...54..195C.

Cropper M. Ramsay G. And Wu K. 1998, *White dwarf masses in magnetic cataclysmic variables: multi-temperature fits to Ginga data*, Monthly Notices of the Royal Astronomical Society, **293,**(3), 222–232. ISSN: 0035-8711. DOI: 10.1046/j.1365-8711.1998.00610.x. URL: http://doi.wiley.com/10.1046/j.1365-8711.1998.00610.x.

Cropper M. 1999, *Effects of Gravity on the Structure of Postshock Accretion Flows in Magnetic Cataclysmic Variables*, Monthly Notices of the Royal Astronomical Society, **306,** 684–690. ISSN: 00358711. DOI: 10.1046/j.1365-8711.1999.02570.x. arXiv: 9902355 [astro-ph]. URL: http://arxiv.org/abs/astro-ph/9902355.

de Martino D. 2004, *BeppoSAX observations of soft X-ray intermediate polars*, *A&A*, **415,** 1009–1019. DOI: 10.1051/0004-6361:20034160. eprint: astro-ph/0311557.

de Martino D. 2008, *1RXS J173021.5-055933: a cataclysmic variable with a fast-spinning magnetic white dwarf*, *A&A*, **481,** 149–159. DOI: 10.1051/0004-6361:20078368. arXiv: 0801.3649.

Dickey J. M. And Lockman F. J. 1990, *H I in the Galaxy*, *Annu. Rev. Astron. Astrophys.*, **28,** 215–261. DOI: 10.1146/annurev.aa.28.090190.001243.

Evans P. A. And Hellier C. 2007, *Why Do Some Intermediate Polars Show Soft X-Ray Emission? A Survey of XMM-Newton Spectra*, *Astrophys. J.*, **663,** 1277–1284. DOI: 10.1086/518552. arXiv: 0704.1388.

Ezuka H. And Ishida M. 1999, *Iron Line Diagnostics of the Postshock Hot Plasma in MagneticCataclysmic Variables Observed with ASCA*, The Astrophysical Journal Supplement Series, **120,**(1), 277–298. ISSN: 00670049. DOI: 10.1086/313181. URL: http://adsabs.harvard.edu/abs/1999ApJS..120..277E.

Fabian A. C. Pringle J. E. And Rees M. J. 1976, *X-ray emission from accretion on to white dwarfs.*, Monthly Notices of the Royal Astronomical Society, **175,** 43–60. URL: http://adsabs.harvard.edu/abs/1976MNRAS.175...43F.

Falanga M, Bonnet-Bidaud J. And Suleimanov V, 2005, *INTEGRAL broadband X-ray spectrum of the intermediate polar V709 Cassiopeiae*, Astronomy and Astrophysics, **444,**(2), 561–564. ISSN: 0004-6361. DOI: 10.1051/0004-6361:20054002. URL: http://adsabs.harvard.edu/abs/2005A{\%}26A...444..561F.

Ferri C. 2011, *X-ray emission from accreting white dwarfs in post-outburst novae*, PhD thesis. Universitat de Barcelona, 175.

Ferri C. And Hernanz M. 2007, *V2487 Oph 1998 : a Magnetic Classical Nova ?*, *15th European Workshop on White Dwarfs ASP Conference Series*. Ed. by R Napiwotzki & M.R. Burleigh. **372,** p. 8–11. URL: http://adsabs.harvard.edu/abs/2007ASPC..372..519F.

Filippenko A. V. 1998, *Nova Ophiuchi 1998*, , **6943,**

Foster A. R. 2011, *AtomDB v2 . 0 : Atomic Data for X-ray Astrophysics*, *2010 NASA Laboratory Astrophysics Workshop*. Gaitlinburg, TN: Schultz, David R., p. C2. URL: http://adsabs.harvard.edu/abs/2011nlaw.confC...2F.

Foster A. R. 2012, *Updated Atomic Data and Calculations for X-Ray Spectroscopy*, The Astrophysical Journal, **756,**(2), 128. ISSN: 0004-637X. DOI: 10.1088/0004-637X/756/2/128. URL: http://stacks.iop.org/0004-637X/756/i=2/a=128?key=crossref.b434017b11a0ec2fe162108dbb76f744.

Frank J. King A. And Raine D. 1992, *Accretion power in astrophysics*.

Frank J. King A. And Raine D. 2002, *Accretion Power in Astrophysics: Third Edition*. Third Edit. **39,** Cambridge University Press, 398. ISBN: 0521620538. URL: http://adsabs.harvard.edu/abs/2002apa..book.....F.

Frank J. And King R. A. 1984, *Column accretion onto white dwarfs - Non-local electron transport and the soft X-ray excess*, Astronomy and Astrophysics, **134,** 328–332. URL: http://adsabs.harvard.edu/abs/1984A{\%}26A...134..328F.

Frank, J. King, A. R. and Lasota J. P. 1983, *Column accretion on to white dwarfs*, Monthly Notices of the Royal Astronomical Society, **202,**(0035-8711), 183–199. DOI: 10.1093/mnras/202.1.183. URL: http://adsabs.harvard.edu/abs/1983MNRAS.202..183F.

Fujimoto R. And Ishida M. 1997, *Mass Determination of the White Dwarf in Magnetic Cataclysmic Variables*, *X-Ray Imaging and Spectroscopy of Cosmic Hot Plasmas*. Ed. by F. Makino & K. Mitsuda, p. 561.

Fujimoto R. And Ishida M. 1997, *XRay Spectroscopic Observations of EX Hydrae and Mass Determination of the White Dwarf*, The Astrophysical Journal, **474,**(2), 774–781. ISSN: 0004-637X. DOI: 10.1086/303483. URL: http://stacks.iop.org/0004-637X/474/i=2/a=774.

Girish V. And Singh K. P. 2012, *X-ray observations of INTEGRAL discovered cataclysmic variable IGR J17195-4100*, *MNRAS*, **427,** 458–467. DOI: 10.1111/j.1365-2966.2012.21916.x. arXiv: 1208.3425 [astro-ph.HE].

Goldwurm A. 2003, *The INTEGRAL/IBIS scientific data analysis*, *A&A*, **411,** L223–L229. DOI: 10.1051/0004-6361:20031395. eprint: astro-ph/0311172.

Haberl F. Motch C. And Zickgraf F.-J. 2002, *X-ray and optical observations of 1RXS J154814.5-452845: A new intermediate polar with soft X-ray emission*, *A&A*, **387,** 201–214. DOI: 10.1051/0004-6361:20020347. eprint: astro-ph/0203227.

Haberl F. 1994, *Discovery of the new intermediate polar RX J0558.0+5353*, *A&A*, **291,** 171–180.

Hachisu I. 2002, *V2487 Ophiuchi: A strong candidate for a recurrent nova and a progenitor of Type Ia supernova*, *The Physics of Cataclysmic Variables and Related Objects*, *ASP Conference Series*. Ed. by B. T. Gnsicke, K. Beuermann, & K. Reinsch. **261,** San Francisco, p. 629. URL: http://adsabs.harvard.edu/abs/2002ASPC..261..629H.

Harris M. J. 1999, *Transient Gamma Ray Spectrometer Observations of Gamma-Ray Lines from Novae. I. Limits on the Positron Annihilation Line in Five Individual Novae*, *Astrophys. J.*, **522,** 424–432. DOI: 10.1086/307625. eprint: astro-ph/0004164.

Hayakawa A. And Hoshi R. 1976, *Extended X-Ray Emission Region of an Accreting White Dwarf*, Progress of Theoretical Physics, **55,**(4), 1320–1321. ISSN: 0033-068X. DOI: 10.1143/PTP.55.1320. URL: https://academic.oup.com/ptp/article-lookup/doi/10.1143/PTP.55.1320http://adsabs.harvard.edu/abs/1976PThPh..55.1320H.

Hayakawa S. Matsuoka M. And Sugimoto D. 1966, *Galactic X-Rays*, Space Science Reviews, **5,** 109–163. DOI: 10.1007/BF00179217. URL: http://adsabs.harvard.edu/abs/1966SSRv....5..109H.

Hayashi T. 2014, PhD thesis. Tokyo Metropolitan University, 155.

Hayashi T. And Ishida M. 2014a, *A new comprehensive X-ray spectral model from the post-shock accretion column in intermediate polars*, Monthly Notices of the Royal Astronomical Society, **438,**(3), 2267–2277. ISSN: 00358711. DOI: 10.1093/mnras/stt2342.

— 2014. b, *Application of the new comprehensive X-ray spectral model to the two brightest intermediate polars ex hydrae and V1223 sagittarii*, Monthly Notices of the Royal Astronomical Society, **441,**(4), 3718–3723. ISSN: 13652966. DOI: 10.1093/mnras/stu766.

Hellier C. Mukai K. And Osborne J. P. 1998, *Iron Kalpha linewidths in magnetic cataclysmic variables*, *MNRAS*, **297,** 526–530. DOI: 10.1046/j.1365-8711.1998.01557.x. eprint: astro-ph/9802040.

Hellier C. 1996, *The X-ray spectrum of the intermediate polar AO Piscium*, Monthly Notices of the Royal Astronomical Society, **280,** 877–887. DOI: 10.1093/mnras/280.3.877. URL: http://adsabs.harvard.edu/abs/1996MNRAS.280..877H.

Hellier C. 1996, *The intermediate polars, Cataclysmic variables and related objects. Astrophysics and Space Science Library; Proceedings of the 158th colloquium of the International Astronomical Union (IAU)*. Ed. by A. Evans & Janet H. Wood. **208,** Keele: Kluwer Academic Publishers, p. 143. DOI: 10.1007/978-94-009-0325-8_44. URL: http://adsabs.harvard.edu/abs/1996ASSL..208..143H.

Hellier C. And Mukai K. 2004, *On the iron K(alfa) complex in magnetic cataclysmic variables*, Monthly Notices of the Royal Astronomical Society, **352,**(3), 1037–1040. ISSN: 00358711. DOI: 10.1111/j.1365-2966.2004.07995.x.

Hernanz M. And Sala G. 2002, *A Classical Nova, V2487 Oph 1998, Seen in X-rays Before and After Its Explosion*, Science, **298,**(5592), 393–395. ISSN: 00368075. DOI: 10.1126/science.298.5592.393. URL: http://www.sciencemag.org/cgi/doi/10.1126/science.298.5592.393.

Hoshi R. 1973, *X-Ray Emission from White Dwarfs in Close Binary Systems*, Progress of Theoretical Physics, **49,**(3), 776–789. DOI: 10.1143/PTP.49.776. URL: http://adsabs.harvard.edu/abs/1973PThPh..49..776H.

Imamura J. N. 1981, *The Ultraviolet and X-Ray Spectra of Accreting Degenerate Dwarfs.*, PhD thesis. INDIANA UNIVERSITY.

Imamura J. N. And Durisen R. H. 1983, *X-ray spectra and light curves of accreting magnetic degenerate dwarfs*, The Astrophysical Journal, **268,** 291–308. DOI: 10.1086/160954. URL: http://adsabs.harvard.edu/abs/1983ApJ...268..291I.

Imamura J. N. 1987, *X-ray and ultraviolet radiation from accreting white dwarfs. IV - Two-temperature treatment with electron thermal conduction*, The Astrophysical Journal, **313,** 298–319. DOI: 10.1086/164969. URL: http://adsabs.harvard.edu/abs/1987ApJ...313..298I.

Imamura J. N. 1996, *The Stability Properties of Two-Temperature White Dwarf Radiative Shock Waves*, The Astrophysical Journal, **458,** 327–337. DOI: 10.1086/176815. URL: http://adsabs.harvard.edu/abs/1996ApJ...458..327I.

Ishida M. 1991, PhD thesis. PhD thesis,Univ. Tokyo, (1991).

Ishida M. And Fujimoto R. 1995, *Diagnostics of the Postshock Hot Plasma with ASCA - I, Cape Workshop on Magnetic cataclysmic variables; Astronomical Society of the Pacific Conference Series*. **85,** p. 132. URL: http://adsabs.harvard.edu/abs/1995ASPC...85..132I.

Ishida M. Mukai K. And Osborne J. P. 1994, *Observation of EX Hydrae with ASCA*, , **46,** L81–L85.

Katz J. I. 1977, *X-rays from spherical accretion onto degenerate dwarfs*, The Astrophysical Journal, **215,** 265–275. DOI: 10.1086/155355. URL: http://adsabs.harvard.edu/abs/1977ApJ...215..265K.

King A. R. And Lasota J. P. 1979, *Accretion on to highly magnetized white dwarfs*, Monthly Notices of the Royal Astronomical Society, **188,**(3), 653–668. ISSN: 0035-8711. DOI: 10.1093/mnras/188.3.653. URL: http://mnras.oxfordjournals.org/content/188/3/653.shorthttps://academic.oup.com/mnras/article-lookup/doi/10.1093/mnras/188.3.653.

Knigge C. Baraffe I. And Patterson J. 2011, *The Evolution of Cataclysmic Variables as Revealed by Their Donor Stars, Astrophys. J. Suppl.*, **194,** 28, 28. DOI: 10.1088/0067-0049/194/2/28. arXiv: 1102.2440 [astro-ph.SR].

Kylafis N. D. And Lamb D. Q. 1979, *X-ray and UV radiation from accreting nonmagnetic degenerate dwarfs,* The Astrophysical Journal Letters, **228,** L105–L110. DOI: 10.1086/182913. URL: http://adsabs.harvard.edu/abs/1979ApJ...228L.105K.

Lamb D. Q. And Masters A. R. 1979, *X and UV radiation from accreting magnetic degenerate dwarfs, Astrophys. J. Lett.*, **234,** L117–L122. DOI: 10.1086/183121.

Landi R. 2009, *INTEGRAL/IBIS and Swift/XRT observations of hard cataclysmic variables, MNRAS*, **392,** 630–640. DOI: 10.1111/j.1365-2966.2008.14086.x. arXiv: 0810.1844.

Langer S. H. Chanmugam C. And Shaviv G. 1982, *Time-dependent accretion onto magnetized white dwarfs,* The Astrophysical Journal, **258,** 289–305. ISSN: 0004-637X. DOI: 10.1086/160079. URL: http://adsabs.harvard.edu/abs/1982ApJ...258..289L.

Langer S. H. Chanmugam G, and Shaviv G, 1981, *Thermal instability in accretion flows onto degenerate stars,* The Astrophysical Journal, **245,** L23. ISSN: 0004-637X. DOI: 10.1086/183514. URL: http://adsabs.harvard.edu/doi/10.1086/183514.

Liller W. And Jones A. 1999a, *Light Curves for Nova Mus 1998 and Nova Oph 1998,* Information Bulletin on Variable Stars, **4774,**

Liller W. And Jones A. F. 1999b, *Light Curves for Nova Sgr 1998 and Nova Sco 1998,* Information Bulletin on Variable Stars, **4664,**

Lodders K. 2003, *Solar System Abundances and Condensation Temperatures of the Elements, Astrophys. J.*, **591,** 1220–1247. DOI: 10.1086/375492.

Lynch D. K. 2000, *0.8-2.5 Micron Spectroscopy of Nova Ophiuchi 1998, Astrophys. J.*, **541,** 791–801. DOI: 10.1086/309453.

Lynden-Bell D. And Pringle J. E. 1974, *The evolution of viscous discs and the origin of the nebular variables., MNRAS*, **168,** 603–637. DOI: 10.1093/mnras/168.3.603.

MacDonald J. And Vennes S. 1991, *Thermal X-ray emission from classical novae in optical decline,* The Astrophysical Journal, **373,** L51–L54. ISSN: 0004-637X. DOI: 10.1086/186049. URL: http://adsabs.harvard.edu/abs/1991ApJ...373L..51Mhttp://adsabs.harvard.edu/doi/10.1086/186049.

Mason K. O. Rosen S. R. And Hellier C. 1988, *The accretion geometry of intermediate polars (DQ HER stars),* Advances in Space Research, **8,** 293–303. DOI: 10.1016/0273-1177(88)90419-X.

Mason K. O. 1992, *A new, EUV-bright intermediate polar discovered in the ROSAT Wide Field Camera all-sky survey, MNRAS*, **258,** 749–758. DOI: 10.1093/mnras/258.4.749.

Matt G. 1999, *X-ray spectroscopy of magnetic CVs, Annapolis Workshop on Magnetic Cataclysmic Variables*. Ed. by C. Hellier & K. Mukai. **157,** Astronomical Society of the Pacific Conference Series, p. 299.

Mewe R. Gronenschild E. H. B. M. And van den Oord G. H. J. 1985, *Calculated X-radiation from optically thin plasmas. V*, , **62,** 197–254.

Mewe R, Lemen J. R. And Oord G. H. J. 1986, *Calculated X-radiation from optically thin plasmas. VI - Improved calculations for continuum emission and approximation formulae for nonrelativistic average Gaunt factors,* Astronomy & Astrophysics Supplement Series, **65,** 511–536. ISSN: 0365-0138. URL: http://adsabs.harvard.edu/abs/1986A{\&}AS...65..511M.

Motch C. 1996, *New cataclysmic variables from the ROSAT All-Sky Survey., A&A*, **307,** 459–469.

Mukai K. 1997, *The X-Ray Eclipse of the Dwarf Nova HT Cassiopeiae: Results from ASCA and ROSAT HRI Observations, Astrophys. J.*, **475,** 812–822. DOI: 10.1086/303571.

Nakano S. 1998, *Possible Nova in Ophiuchus,* , **6941,**

Narayan R. And Popham R. 1993, *Hard X-rays from accretion disk boundary layers, Nature*, **362,** 820–822. DOI: 10.1038/362820a0.

Nauenberg M. 1972, *Analytic Approximations to the Mass-Radius Relation and Energy of Zero-Temperature Stars,* The Astrophysical Journal, **175,** 417–430. ISSN: 0004-637X. DOI: 10.1086/151568. URL: http://adsabs.harvard.edu/doi/10.1086/151568.

Pagnotta A. Schaefer B. E. And Xiao L. 2008, *V2487 Ophiuchi,* , **8951,**

Pagnotta A. 2009, *Discovery of a Second Nova Eruption of V2487 Ophiuchi, Astr. J.*, **138,** 1230–1234. DOI: 10.1088/0004-6256/138/5/1230. arXiv: 0908.2143 [astro-ph.HE].

Pandel D. 2005, *X-Ray Observations of the Boundary Layer in Dwarf Novae at Low Accretion Rates, Astrophys. J.*, **626,** 396–410. DOI: 10.1086/429983. eprint: astro-ph/0503114.

Patterson J. 1994, *The DQ Herculis stars,* , **106,** 209–238. DOI: 10.1086/133375.

Press W. H. 2003, *Numerical recipes in Fortran 77*. Second Edi. Press Syndicate of the University of Cambridge, 1003. ISBN: 052143064X.

Ramsay G. And Cropper M. 2004, *The energy balance of polars revisited, MNRAS*, **347,** 497–507. DOI: 10.1111/j.1365-2966.2004.07220.x. eprint: astro-ph/0309527.

Ramsay G, 1998, *A comparison of white dwarf mass estimators using the intermediate polar XY Ari,* Monthly Notices of the Royal Astronomical Society, **297,**(4), 1269–1273. ISSN: 0035-8711. DOI: 10.1046/j.1365-8711.1998.01609.x. URL: https://academic.oup.com/mnras/article-lookup/doi/10.1046/j.1365-8711.1998.01609.xhttp://adsabs.harvard.edu/abs/1998MNRAS.297.1269R.

Ramsay G. 2009, *2XMMiJ225036.9+573154 - a new eclipsing AMHer binary discovered using XMM-Newton, MNRAS*, **395,** 416–421. DOI: 10.1111/j.1365-2966.2009.14528.x. arXiv: 0901.3095 [astro-ph.GA].

Ramsay G. 2000, *Determining the mass of the accreting white dwarf in magnetic cataclysmic variables using RXTE data,* Monthly Notices of the Royal Astronomical Society, **314,**(2), 403–408. ISSN: 0035-8711. DOI: 10.1046/j.1365-8711.2000.03239.x. arXiv: 9912420 [astro-ph]. URL: http://arxiv.org/abs/astro-ph/9912420https://academic.oup.com/mnras/article-lookup/doi/10.1046/j.1365-8711.2000.03239.x.

Rana V. R. 2006, *Study of Fe Kα lines in Nonmagnetic Cataclysmic Variables Using Chandra HEG Data, Astrophys. J.*, **642,** 1042–1050. DOI: 10.1086/500316. eprint: astro-ph/0512274.

Revnivtsev M. G. 2004, *Broadband X-ray Spectrum of the Intermediate Polar V2400 Oph,* Astronomy Letters, **30,**(11), 772–778. ISSN: 1063-7737. URL: http://adsabs.harvard.edu/abs/2004AstL...30..772R.

Ritter H. 2010, *Formation and evolution of cataclysmic variables .*, , **81,** 849.

Sala G. 2004a, *X-ray emission from classical novae,* PhD thesis. Universitat de Barcelona, 252.

— 2004. b, *XRay Emission from Classical Novae,* Publications of the Astronomical Society of the Pacific, **116,**(826), 1154–1154. ISSN: 0004-6280. DOI: 10.1086/427071. URL: http://adsabs.harvard.edu/abs/2004PASP..116.1154Shttp://iopscience.iop.org/article/10.1086/427071.

Saxton C. J. 1999, *Stability properties of radiative accretion shocks with multiple cooling processes.*, PhD thesis. PhD thesis, Univ. Sydney, Australia , (1999).

Saxton C. J. 1998, *Oscillatory instability of radiative shocks with multiple cooling processes,* Monthly Notices of the Royal Astronomical Society, **299,**(3), 862–876. ISSN: 0035-8711. DOI: 10.1046/j.1365-8711.1998.01839.x. URL: https://academic.oup.com/mnras/article-lookup/doi/10.1046/j.1365-8711.1998.01839.x.

Saxton C. J. And Wu K. 1999, *Perturbative analysis of two-temperature radiative shocks with multiple cooling processes,* Monthly Notices of the Royal Astronomical Society, **310,**(3), 677–692. ISSN: 0035-8711. DOI: 10.1046/j.1365-8711.1999.02967.x. arXiv: 9909502v1 [arXiv:astro-ph]. URL: https://academic.oup.com/mnras/article-lookup/doi/10.1046/j.1365-8711.1999.02967.x.

Saxton C. J. 2005, *Two-temperature accretion flows in magnetic cataclysmic variables: structures of post-shock emission regions and X-ray spectroscopy,* Monthly Notices of the Royal Astronomical Society, **360,**(3), 1091–1104. ISSN: 0035-8711. DOI: 10.1111/j.1365-2966.2005.09103.x. URL: http://adsabs.harvard.edu/abs/2005MNRAS.360.1091S.

Saxton C. J. 2007, *X-ray emissions from two-temperature accretion flows within a dipole magnetic funnel,* Monthly Notices of the Royal Astronomical Society, **379,** 779–790. ISSN: 0035-8711. DOI: 10.1111/j.1365-2966.2007.11958.x. URL: http://adsabs.harvard.edu/abs/2007MNRAS.379..779S.

Schaefer B. E. 2010, *Comprehensive Photometric Histories of All Known Galactic Recurrent Novae, Astrophys. J. Suppl.*, **187,** 275–373. DOI: 10.1088/0067-0049/187/2/275. arXiv: 0912.4426 [astro-ph.SR].

Smith R. K. 2001, *Collisional Plasma Models with APEC/APED: Emission-Line Diagnostics of Hydrogen-like and Helium-like Ions,* The Astrophysical Journal, **556,**(2), L91–L95. ISSN: 0004637X. DOI: 10.1086/322992. arXiv: 0106478 [astro-ph]. URL: http://adsabs.harvard.edu.ezp-prod1.hul.harvard.edu/abs/2001ApJ...556L..91S{\%}5Cnhttp://iopscience.iop.org/1538-4357/556/2/L91/fulltext/.

Staude A. 2008, *The changing accretion states of the intermediate polar MU Camelopardalis*, *A&A*, **486,** 899–909. DOI: 10.1051/0004-6361:20067013. arXiv: 0806.0793.

Strope R. J. Schaefer B. E. And Henden A. A. 2010, *Catalog of 93 Nova Light Curves: Classification and Properties*, *Astr. J.*, **140,** 34–62. DOI: 10.1088/0004-6256/140/1/34. arXiv: 1004.3698 [astro-ph.SR].

Suleimanov V. Revnivtsev M. And Ritter H. 2005, *RXTE broadband X-ray spectra of intermediate polars and white dwarf mass estimates*, Astronomy and Astrophysics, **435,**(1), 191–199. ISSN: 0004-6361. DOI: 10.1051/0004-6361:20041283. arXiv: 0405236v1 [arXiv:astro-ph]. URL: http://cdsads.u-strasbg.fr/abs/2005A{\&}A...435..191Shttp://www.edpsciences.org/10.1051/0004-6361:20041283.

Suleimanov V. 2016, *GK Persei and EX Hydrae: Intermediate polars with small magnetospheres*, Astronomy & Astrophysics, **591,** A35. ISSN: 0004-6361. DOI: 10.1051/0004-6361/201628301. arXiv: 1604.00232. URL: http://arxiv.org/abs/1604.00232http://www.aanda.org/10.1051/0004-6361/201628301.

Sutherland R. S. And Dopita M. A. 1993, *Cooling functions for low-density astrophysical plasmas*, The Astrophysical Journal Supplement Series, **88,** 253. ISSN: 0067-0049. DOI: 10.1086/191823. URL: http://adsabs.harvard.edu/doi/10.1086/191823.

Ubertini P. 2003, *IBIS: The Imager on-board INTEGRAL*, *A&A*, **411,** L131–L139. DOI: 10.1051/0004-6361:20031224.

Verner D. A. 1996, *Atomic Data for Astrophysics. II. New Analytic FITS for Photoionization Cross Sections of Atoms and Ions*, *Astrophys. J.*, **465,** 487. DOI: 10.1086/177435. eprint: astro-ph/9601009.

Vogel J. 2008, *The serendipituous discovery of a short-period eclipsing polar in 2XMMp*, *A&A*, **485,** 787–795. DOI: 10.1051/0004-6361:20079341. arXiv: 0804.3946.

Wada T.-a. 1980, *X-Ray and Infrared Emissions from Accreting Magnetic White Dwarfs: A Model for AM Herculis*, Progress of Theoretical Physics, **64,**(6), 1986–1994. ISSN: 0033-068X. DOI: 10.1143/PTP.64.1986. URL: http://adsabs.harvard.edu/abs/1980PThPh..64.1986Whttps://academic.oup.com/ptp/article-lookup/doi/10.1143/PTP.64.1986.

Warner B. 1995, *Cataclysmic variable stars.*, Cambridge Astrophysics Series, **28,**

Woelk, U. and Beuermann K. 1996, *Stationary radiation hydrodynamics of accreting magnetic white dwarfs.*, Astronomy and Astrophysics, **306,** 232–240. URL: http://adsabs.harvard.edu/abs/1996A{\%}26A...306..232W.

Wolff M. T. Gardner J. H. And Wood K. S. 1989, *On the stability of degenerate dwarf radiative shocks - New one- and two-temperature calculations*, The Astrophysical Journal, **346,** 833. ISSN: 0004-637X. DOI: 10.1086/168064. URL: http://adsabs.harvard.edu/abs/1989ApJ...346..833Whttp://adsabs.harvard.edu/doi/10.1086/168064.

Wu K. Chanmugam G. And Shaviv G. 1995, *X-rays from Magnetic CVs and White Dwarf Mass Determination*, *Magnetic Cataclysmic Variables. Cape Workshop on Magnetic cataclysmic variables; Astronomical Society of the Pacific Conference Series*. Ed. by D. A. H.

Buckely & Brian Warner. **85,** Cape Town: Astronomical Society of the Pacific, p. 436. URL: http://adsabs.harvard.edu/abs/1995ASPC...85..436W.

Wu K. 1994, *Structure of inhomogeneous accretion shocks,* Proceedings of the Astronomical Society of Australia, **11,** 61–64. ISSN: 00669997. URL: http://adsabs.harvard.edu/abs/1994PASAu..11...61W.

Wu K. Chanmugam G. And Shaviv G. 1994, *Structure of steady state accretion shocks with several cooling functions: Closed integral-form solution,* The Astrophysical Journal, **426,** 664. ISSN: 0004637X. DOI: 10.1086/174103. URL: http://adsabs.harvard.edu/doi/10.1086/174103.

Wu K. And Cropper M. 2001, *The lower boundary of the accretion column in magnetic cataclysmic variables,* Monthly Notices of the Royal Astronomical Society, **326,**(2), 686–694. ISSN: 00358711. DOI: 10.1046/j.1365-8711.2001.04640.x. arXiv: 0105140 [astro-ph].

Wu, Kinwah and Wickramasinghe D. T. 1992, *Three-dimensional structured shocks in AM Herculis-type systems. II - Cyclotron emission from ridge-shaped emission regions,* Monthly Notices of the Royal Astronomical Society, **256,** 329–338. DOI: 10.1093/mnras/256.2.329. URL: http://adsabs.harvard.edu/abs/1992MNRAS.256..329W.

Yuasa T, 2010, *White dwarf masses in intermediate polars observed with the Suzaku satellite,* Astronomy and Astrophysics, **520,** A25. ISSN: 0004-6361. DOI: 10.1051/0004-6361/201014542. URL: http://www.aanda.org/10.1051/0004-6361/201014542.

Zombeck M. V. 1982, *Hot plasma Emission, Handbook of Space Astronomy and Astrophysics*. Cambridge University Press, p. 326. ISBN: 0-521-24194-4.

# A

# GENERAL HYDRODYNAMICS FORMULATION

An accretion flow is governed entirely by conservation laws: the conservation of mass, the conservation of momentum and the conservation of energy. These conservation laws can be written in the form of partial differential equations as well as in the form of integral equations. Both forms, will prove to be useful for the numerical methods and are described as follow.

## A.1 Mass Conservation

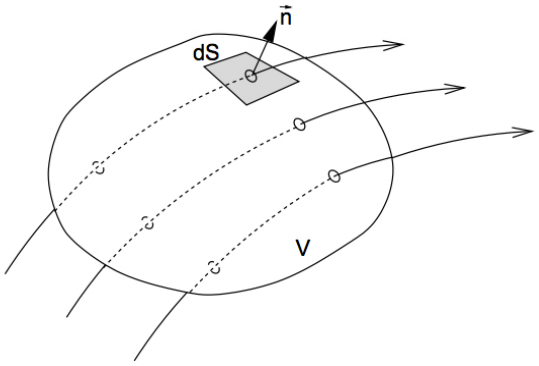


FIGURE A.1: Flow through a volume $V$ with surface $\partial V = S$.

Consider an arbitrary volume $V$ in the space in which the gas flow takes place. Its surface is denoted as $\partial V = S$ with the normal unit vector at each location on the surface denoted as $\vec{n}$ and differential surface element as $dS$ (Figure A.1). Let $\rho$ be the fluid density into the

volume $V$ where there are no masses sources of sinks. Then, by mass conservation

$$\frac{D}{Dt}\iiint_V \rho dV = 0 \tag{A.1}$$

from kinetic transport theorem[1] this equation can be expressed as

$$\iiint_V \frac{\partial \rho}{\partial t} dV + \iint_S \rho \vec{v} \cdot \vec{n} dS = 0 \tag{A.2}$$

and using the Gauss' theorem

$$\iiint_V \vec{\nabla} \cdot G dV = \iint_S G \cdot \vec{n} dS \tag{A.3}$$

the surface integral is written as a volume integral in the way

$$\iint_S \rho \vec{v} \cdot \vec{n} dS = \iiint_V \vec{\nabla} \cdot (\rho \vec{v}) dV \tag{A.4}$$

Since all volume integrals are in an arbitrary volume, the mass conservation law, also called *continuity equation*, is

$$\frac{\partial \rho}{\partial t} + \vec{\nabla}(\rho \vec{v}) = 0 \tag{A.5}$$

## A.2 Momentum Conservation

Applying the second Newton's law in a volume containing a fluid it is possible to obtain

$$\frac{D}{Dt}\iiint_V \rho \vec{v} dV = \sum \vec{F} \tag{A.6}$$

There are two types of forces which can act on a fluid.

- *Surface forces*, also called short-range forces, have a molecular origin and decrease rapidly with the distance between the interacting elements. They are appreciable only if the fluid elements are in contact, therefore exist only in the boundary. Surface forces over area unit is called stress $\vec{S}$ which depends on time, location, and orientation of the surface element. The total surface force acting on the fluid is $\iint_S \vec{S} dA$. The pressure and friction are examples of short-range forces.
- *Body forces*, also known as long-range forces, have an origin far away for the zone of interest. Their strength change very slowly, and act uniformly on all parts of the fluid. The sum of long-range forces, denotes as $\vec{f}$, is proportional to the volume of the fluid. The total body forces acting on the volume is $\iint\iint_V \vec{f} dV$. The gavity is an example of long-range forces.

[1] Being $G(\vec{r}, t)$ some fluid property per unit volume, then $\frac{D}{Dt}\iiint_V G dV = \iiint_V \frac{\partial G}{\partial t} dV + \iint_S G \vec{v} \vec{n} dS$

therefore, the second Newton's law is expressed as

$$\frac{D}{Dt}\iiint_V \rho\vec{v}dV = \iint_S \vec{S}dA + \iiint_V \vec{f}dV \tag{A.7}$$

using the kinetic transport theorem, the left-hand side becomes

$$\frac{D}{Dt}\iiint_V \rho\vec{v}dV = \iiint_V \rho\frac{D}{Dt}\vec{v}dV \tag{A.8}$$

the first term in the rigth-hand side can be expressed as an volume integral using the Gauss' theorem in the form

$$\iint_S \vec{S}dA = \iiint_V \vec{\nabla}\hat{\sigma}dV \tag{A.9}$$

where $\hat{\sigma}$ is an square array called stress tensor. According to the Cauchy's theorem, $\sigma_{ij}$, describes the stress components on any surface. (see Figure A.2).

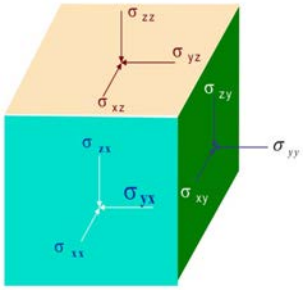


FIGURE A.2: Components in the surface.

Since now all terms are expressed as volume integrals, the momentun equation can be written as

$$\rho\frac{D}{Dt}\vec{v} = \vec{\nabla}\hat{\sigma} + \vec{f} \tag{A.10}$$

applying the kinetic transport theorem, the first term can be expressed as

$$\rho\frac{D}{Dt}\vec{v} = \rho\left(\frac{\partial}{\partial t}\vec{v} + (\vec{v}\vec{\nabla})\vec{v}\right) \tag{A.11}$$

thus, the momentun conservation equation is

$$\rho\left(\frac{\partial}{\partial t}\vec{v} + (\vec{v}\vec{\nabla})\vec{v}\right) = \vec{\nabla}\hat{\sigma} + \vec{f} \tag{A.12}$$

Let assume now that the only surface force acting in the fluid is the hydrostatic pressure $P$. According to the Pascal's principle, in a fluid at rest the pressure is uniformly transmitted in all directions and in all portions of the fluid. Therefore, the pressure is isotropic and $\hat{\sigma}$ only has diagonal components. Moreover, all of them have the same value $P$. Thus, the stress tensor has the form $\hat{\sigma} = -P\hat{I}$ where the minus sign is adopted by convention.

Therefore the momentun equation (likewise known as *Euler's equation*) is written as

$$\rho\left(\frac{\partial\vec{v}}{\partial t}+(\vec{v}\vec{\nabla})\vec{v}\right)=\vec{f}-\vec{\nabla}P \tag{A.13}$$

## A.3 Energy Conservation

Energy exists in many forms. Consider the two most basic ones: mechanical and thermal energy. $e$ is the internal (thermal) energy per unit of mass due to microscopic motion and $v^2/2$ the kinetic energy per unit of mass due to macroscopic motion. According to the first thermodynamics law, the energy conservation requires

$$\frac{D}{Dt}\iiint_V \rho\left(e+\frac{v^2}{2}\right)dV=-\iint_S\vec{Q}\cdot\vec{n}dS-\iint_S\vec{F}_{rad}\cdot\vec{n}dS+\iiint_V\vec{f}\cdot\vec{v}dV+\iint_S\vec{S}\cdot\vec{v}dS \tag{A.14}$$

using the kinetic transport theorem, the left hand side term, which accounts for the rate of increment of energy in $V$ can be written as

$$\iiint_V\frac{D}{Dt}\rho\left(e+\frac{v^2}{2}\right)dV \tag{A.15}$$

and using the Gauss theorem the first term on the rigth hand side, which is the rate of heat flux into $V$, can be expressed as

$$-\iint_S\vec{Q}\cdot\vec{n}dS=-\iiint_V\vec{\nabla}\cdot\vec{Q}dV \tag{A.16}$$

In the same way, the second term, which represents the rate of radiation flux into $V$ can be written as

$$-\iint_S\vec{F}_{rad}\cdot\vec{n}dS=-\iiint_V\vec{\nabla}\cdot\vec{F}_{rad}dV \tag{A.17}$$

the last two terms on the rigth hand side are the rate of work produced by body and surface forces, respectively. The last term can be rewritten as

$$\iint_S\vec{S}\vec{v}dS=\iint_S(\hat{\sigma}\vec{n})\vec{v}dS=\iint_S(\hat{\sigma}\vec{v})\vec{n}dS=\iiint_V\vec{\nabla}(\hat{\sigma}\vec{v})dv \tag{A.18}$$

Since now all terms are expressed as volume integrals over an arbitrary volume, Equation (A.14) is in the form

$$\frac{D}{Dt}\rho\left(e+\frac{v^2}{2}\right)=-\vec{\nabla}\vec{Q}-\vec{\nabla}\vec{F}_{rad}+\vec{f}\vec{v}+\vec{\nabla}(\hat{\sigma}\vec{v}) \tag{A.19}$$

applying the kinetic transport theorem, the first term can be expressed as

$$\frac{D}{Dt}\rho\left(e+\frac{v^2}{2}\right)=\frac{\partial}{\partial t}\left(\rho e+\frac{1}{2}\rho v^2\right)+\vec{\nabla}\left(\rho e+\frac{1}{2}\rho v^2\right)\vec{v} \tag{A.20}$$

considering that the only surface force is the hydrostatic pressure, the energy conservation equation can be expressed as

$$\frac{\partial}{\partial t}\left(\rho e + \frac{1}{2}\rho v^2\right) + \vec{\nabla}\left(\rho e + \frac{1}{2}\rho v^2\right)\vec{v} = -\vec{\nabla}\vec{Q} - \vec{\nabla}\vec{F}_{rad} + \vec{f}\vec{v} + \vec{\nabla}(P\vec{v}) \tag{A.21}$$

since $\nabla(P\vec{v}) = P\nabla\vec{v} + \vec{v}\vec{\nabla}P$ and $\nabla\vec{v} = 0$ and moving the pressure term to the left hand side, the resulted equation is

$$\frac{\partial}{\partial t}\left(\rho e + \frac{1}{2}\rho v^2\right) + \vec{\nabla}\left(\rho e + \frac{1}{2}\rho v^2 + P\right)\vec{v} = -\vec{\nabla}\vec{Q} - \vec{\nabla}\vec{F}_{rad} + \vec{f}\vec{v} \tag{A.22}$$

# B

# COMPUTATIONAL METHOD

The solution of the hydrodynamic equations is reduced to solving an initial value problem of ordinary differential equations. This can be performed with the so-called shooting method via Newton-Raphson. The equations are integrated numerically using an embedded Runge–Kutta method. Integration proceeds between the shock point and the white dwarf surface. Each trial starts from an assumed shock height $z = z_0$, where the initial parameters are set according to the strong shock limit of the Rankine-Hugoniot relation. The lower limit of the calculation, $z = R_{WD}$, is specified by the WD mass-radius relation. At the WD surface, another boundary condition of the bulk gas speed $v = 0$ is imposed to fulfill the soft-landing assumption.

## B.1 Embedded Runge-Kutta Method

Problems involving ordinary differential equations (ODEs) can always be reduced to the study of sets of first-order differential equations. For example the second-order equation

$$\frac{d^2y}{dx^2} + q(x)\frac{dy}{dx} = r(x) \tag{B.1}$$

can be rewritten as two first-order equations

$$\begin{aligned} \frac{dy}{dx} &= z(x) \\ \frac{dz}{dx} &= r(x) - q(x)z(x) \end{aligned} \tag{B.2}$$

where $z$ is a new variable.

The generic problem in ordinary differential equations is thus reduced to the study of a set of N coupled first-order differential equations for the functions $y_i$,

$$\frac{dy_i(x)}{dx} = f_i(x, y_1, ..., y_N) \quad i = 1, ..., N \tag{B.3}$$

the embedded Runge-Kutta formulas provide a method to solve numerically the system with a stepsize adjustment algorithm based on a fifth-order Runge-Kutta method.
For a given stepsize $h$, the Runge-Kutta method advances the solution from $x_n$ to $x_{n+1} = x_n + h$, evaluating the functions $f_i$ once at the initial point of the interval, once at a trial end point, and twice or more time at trial midpoints, the number of these midpoints depending on the order of the Runge-Kutta method (in the case of fourth-order Runge-Kutta there are two midpoints).
The embedded Runge-Kutta method is based on the use of six function evaluations combined in two different ways that give a fifth-order and a fourth-order Runge-Kutta methods. The stepsize is adjusted using the difference between the two solutions of $y(x + h)$ as an estimation of the truncation error.
The general form of a fifth-order Runge-Kutta formula is

$$\begin{aligned} k_1 &= hf(x_n, y_n) \\ k_2 &= hf(x_n + a_2 h, y_n + b_{21} k_1) \\ &\cdots \\ k_6 &= hf(x_n + a_6 h, y_n + b_{61} k_1 + \cdots + b_{65} k_5) \\ y_{n+1} &= y_n + c_1 k_1 + c_2 k_2 + c_3 k_3 + c_4 k_4 + c_5 k_5 + c_6 k_6 + O(h^6) \end{aligned} \tag{B.4}$$

The embedded fourth-order formula is

$$y^*_{n+1} = y_n + c^*_1 k_1 + c^*_2 k_2 + c^*_3 k_3 + c^*_4 k_4 + c^*_5 k_5 + c^*_6 k_6 + O(h^5) \tag{B.5}$$

and the estimated truncation error is

$$\Delta = y_{n+1} - y^*_{n+1} = \sum_{i=1}^{6} (c_i - c^*_i) k_i \tag{B.6}$$

where $a_i$, $b_{ij}$, $c_i$ and $c^*_i$ are the Cask-Karp parameters for embedded Runge-Kutta method (Cash & Karp, 1990), and $y_n$ indicates the value of the vector of dependent variables, $y = (y_1, ..., y_N)$ at the $n$ step of the integration.
The stepsize control is imposed demanding $\Delta$ to be smaller than a given accuracy value at each step. It is convenient to set the accuracy value for each element of the vector $\Delta$ indenpendently, using a vector argument, `yscal(1:N)`, and a tolerance level called `eps`, so that $\Delta(i) =$ `eps` $\times$ `yscal(i)`. In this work, `yscal(i)` has been setted as `yscal(i)` $=|$ `y(i)` $| + |$ `h*dydx(i)` $|$
Once the desired accuracy $\Delta$ is determined, some relation between $\Delta$ and the stepsize $h$ is needed to impose this control. As seen from Eqs. (B.4-B.6), $\Delta$ scales as $h^5$. If we

denote by $h_1$ a stepsize that gives an error $\Delta_1$, the stepsize $h_0$ that would give the desired accuracy $\Delta_0$ can be estimated as

$$h_0 = h_1 \left| \frac{\Delta_0}{\Delta_1} \right|^{\frac{1}{5}} \tag{B.7}$$

If the accuracy of the previous step, $\Delta_1$, is larger than the desired accuracy, the same step will be recalculated using the new step $h_1$; otherwise, if $\Delta_0$ is good enough, $h_0$ will be the stepsize used in the next integration step.
In this work the routines *rkqs* and *rkck* from Press et al. (2003), which apply the embedded Runge-Kutta method, have been used.

- **Subroutine:** `rkqs`, `odeint`

  **rkqs:** Subroutine that performs a single step of fifth-order Runge-Kutta integration, with monitoring of local truncation error and corresponding step-size adjustment. The routine `rkqs` call the routine `rkck` to take a Cash-Karp Runge-Kutta step.

  **odeint:** Is the driver routine for `rkqs`, which provides Runge-Kutta integration over large intervals with adaptative step-size control. It stores intermediate results in a common block called `path`. Also records the number of function evaluations used, how many steps were successful, and how many were "bad".

- **Uses:** `rkck`, `derivs`

  **rkck:** Subroutine that given values for $n$ variables $y$ and their derivates $dydx$ known at $x$, use the fifth-order Cash-Karp Runge-Kutta method to advance the solution over an interval $h$ and return the incremented variables as `yout`. Also return an estimate of the local truncation error in `yout` using the embedded fourth-order method.

  **derivs:** The subroutine `derivs` computes the derivates $dydx$ at $x$, and supplies the information to the ODE integrator.

- **Inputs:**

  **a)** The dependent variable vector `y(1:n)` and its derivate `dydx(1:n)` at the starting value of the independent variable $x$: In our case, the dependent variables are `P0` and `v0` and the independent variable is $z'$ (`x` in the program).

  **b)** The stepsize `htry`: this vector is calculated from the given values of `h1`, `x1` and `x2`. `h1` is the first stepsize assumed and `x1` and `x2` are the lower and upper limits of integration respectively, from `x1=0` to `x2=z0-R`.

  **c)** The accuracy `eps`.

  **d)** The vector `yscal(1:n)`: is calculated in `odeint` from the given values of `h` and `dydx` (`dP/dz'`; `dv/dz'`).

- **Outputs:** `x` and `y`. In our case: `x` corresponds to $z'$, `y(1)` to $P(z')$ and `y(2)` to $v(z')$.

## B.2 The Shooting method

The shooting method is a numerical method for solving a two point boundary value problem.
A two point boundary value problem is a system of ordinary differential equations with solution and derivative values specified at more than one point. Most commonly, the solution and derivatives are specified at two points (boundaries) —usually the starting and ending values of the integration—.
Given a set of $N$ coupled first-order ordinary differential equations, satisfying $n_1$ boundary conditions at the starting point $x_1$, and a remaining set of $n_2 = N - n_1$ boundary conditions at the final point $x_2$. The differential equations are:

$$\frac{dy_i(x)}{dx} = g_i(x, y_1, y_2, ..., y_N) \qquad i = 1, 2, ..., N \tag{B.8}$$

At $x_1$, the solution is supposed to satisfy

$$B_{1j}(x_1, y_1, y_2, ..., y_N) = 0 \qquad j = 1, ..., n_1 \tag{B.9}$$

and at $x_2$, it is supposed to satisfy

$$B_{2j}(x_2, y_1, y_2, ..., y_N) = 0 \qquad k = 1, ..., n_2 \tag{B.10}$$

The shooting method choose values for all of the dependent variables at one boundary. These values must be consistent with any boundary conditions for that boundary, but otherwise are arranged to depend on arbitrary free parameters whose values are initially random guess. The ODEs are integrated by initial value methods, arriving at the other boundary (and/or any interior points with boundary conditions specified).
In general, there are discrepancies from the desired boundary values. Now, there is a multidimensional root-finding problem: find the adjustment of the free parameters at the starting point that zeros the discrepancies at the other boundary point(s).
In the *"pure"* shooting, the integration proceeds from $x_1$ to $x_2$, and tries to match boundary conditions at the end of the integration. The implementation of shooting method, in this case, implements multidimensional, globally convergent Newton-Raphson. It seeks to zero $n_2$ functions of $n_2$ variables. The functions are obtained by integrating $N$ differential equations from $x_1$ to $x_2$.
At the starting point $x_1$ there are $N$ starting values $y_i$ to be specified, but subject to $n_1$ conditions. Therefore there are $n_2 = N - n_1$ freely specifiable starting values. Imagine that these freely specifiable values are the components of a vector $\mathbf{V}$ that lives in a vector space of dimension $n_2$, then, it's necessary write a subroutine (load) that generates a complete set of $N$ starting values $y$ satisfying the boundary conditions at $x_1$, from an arbitrary vector value of $\mathbf{V}$ in which there are no restrictions on the $n_2$ component values.

The routines *shoot/funcv* and *newt* from Press et al. (2003) have been used.

- **Subroutine:** `shoot/funcv`, `newt`

  **shoot/funcv:** The `shoot` routine is named `funcv` and is for use with `newt`. This routine solves a two point boundary value for coupled ODEs by shooting from `x1` to `x2`. The routine integrates the ODEs to `x2` using the Runge-Kutta method.

  **newt:** This subroutine uses a globally convergent Newton's method to adjust the values of **V** until the functions `f` are zero.

- **Uses:** `derivs`, `load`, `odeint`, `rkqs`, `score`

  **derivs:** The subroutine `derivs`, supplies derivate information to the ODEs integrator.

  **load:** This subroutine generate the initial values for the `nvar` ODEs at `x1` from the `n2` input coefficients `v(1:n2)`.

  **odeint:** Is the driver routine for `rkqs`, which provides Runge-Kutta integration over large intervals with adaptative step-size control. It stores intermediate results in a common block called `path`. Also records the number of function evaluations used, how many steps were successful, and how many were "bad".

  **rkqs:** Subroutine that performs a single step of fifth-order Runge-Kutta integration, with monitoring of local truncation error and corresponding step-size adjustment. The routine `rkqs` call the routine `rkck` to take a Cash-Karp Runge-Kutta step.

  **score:** The subroutine `score` evaluate the `n2` functions `f(1:n2)` that ought to be zero to satisfy the boundary conditions at `x2`. The functions `f` are returned on output.

- **Inputs:**

  **a)** $x_0$ initial, in our case the initial value is $v(1)$

  **b)** Integration limits $x_1$ and $x_2$.the lower integration limit is $x_1 = 0.0$.

- **Outputs:**

  **a)** Functions `f`. (functions F that are returned)

## B.3 Newton-Raphson method

The Newton-Raphson method is a root-finding method for solve equations numerically. This method requires the evaluation of both the function $f(x)$, and the derivate $f'(x)$, at arbitrary points $x$.
Geometrically, the Newton-Raphson formula consists in extending the tangent line at a current point $x_i$ until it crosses zero, then setting the next guess $x_i + 1$ to the abscissa of that zero-crossing. Algebraically, the method derives from the familiar Taylor series expansion of a function in the neighborhood of a point,

$$f(x + \delta) \approx f(x) + f'(x)\delta + \frac{f''(x)}{2}\delta^2 + \cdots \tag{B.11}$$

For small enough values of $\delta$, and for well-behaved functions, the terms beyond linear are unimportant, hence $f(x+\delta) = 0$ implies

$$\delta = -\frac{f(x)}{f'(x)} \tag{B.12}$$

For an efficient realization of Newton-Raphson the user provides a routine that evaluates both, the function $f(x)$ and its first derivate $f'(x)$ at the point $x$, This is the only input for `newt` that the user have to provide.
A feature of `newt` is that you need not supply the Jacobian matrix analytically; the routine will attempt to compute the necessary partial derivates of $F$ by finite differences in the routine `fdjac`.
The routine `newt` assumes that typical values of all components of $x$ and of $F$ are of order unity, and it can fail if this assumption is badly violated. You should rescale the variables by their typical values before invoking `newt` if this problem occurs.

- **Subroutine:** `newt`

  **newt:** The `newt` routine uses the globally convergent multi-dimensional Newton's method to seeks to zero `n2` functions of `n2` variables. The functions are obtained by integrating $N$ differential equations from `x1` to `x2`.

- **Uses:** `fdjac`, `fmin`, `lnsrch`, `lubksb`, `ludcmp`

  **fdjac:** Subroutine that compute the finite-difference Jacobian, used by `newt` to solve the partial derivates by finite differences. This routine uses differents techniques for computing numerical derivates.

  **fmin:** The subroutine `fmin` is a norm of a vector function used by `newt`.

  **flnsrch:** This routine is used in combination with `lubksb` to solve linear equations or invert a matrix. Given a matrix `a(1:n,1:n)`, with physical dimension `np` by `np`, this routine replaces it by the $LU$ decomposition of a rowwise permutation of itself.

  **lubksb:** Subrotuine to solve the set of $n$ linear equations $A \cdot X = B$ using back-substitution. `a` is a input, not as the matrix $A$ but rather as its $LU$ decomposition, dtermined by the routine `ludcmp`. `b(1:n)` is input as the right hand side vector $B$, and returns with the solution vector $X$. This routine takes into account the possibility that `b` will begin with many zeros elements, so it is efficient to use in matrix inversion.

  **ludcmp:** The subroutine `ludcmp` is called to perform approximate line minimizations. It's used by `newt`for search along a line.

- **Inputs:** The only input to newt is the routine `funcv`, which evaluates the function and first derivate at a point $x$.

- **Outputs:** Roots of the equation.

# C

# FITS FORMAT TO *XSPEC*

Tables with the calculated spectra have been created with *IDL programming language* from an ASCII file with the information of flux and energies. The energy interval goes from $0.1$ keV to $100$ keV with steps of $0.1$ keV.
The instructions below are a brief guide to read and create tables in *IDL* with the FITS format requirements of *XSPEC* for additive table models.

## C.1 FITS files in *IDL*

**General issues**

- Reading FITS files in IDL:

  `IDL>fits_info,'name.fits'`

  General information of FITS file. Primary header (extension 0) and number of extensions (1, 2, 3,...) with basic information of each one (name of extensions, number of data, etc.)

  - `fits_info`: Utility in IDL that provides information about the contents of a FITS file.
  - `'name.fits'`: FITS file name.

  `IDL>tabla=MRDFITS('name.fits',1,hd)`

  Read data and header of the extension 1 of file `'name.fits'` and save the information in `tabla`.

  - `MRDFITS`: Funtion in IDL allowing users to quickly read FITS files in all standard formats.
  - `tabla`: IDL variable to save data read (it can be any name).
  - `1`: number of the read extension (in the example above has been read the extension 1).
  - `hd` is the name given to the header of that extension (it can be any name).

  `IDL>help,tabla`

  Gives the structure of the extension read above (name of each column, type of data, and an example of how are the data).

  - Column 1: Name of the data.
  - Column 2: Type of data.
  - Column 3: Example of name and data.

  `IDL>print,tabla.name`

  Print information of the column `name` read with MRDFITS for the extension indicated previously.

  - `tabla`: IDL variable that has saved the information read with MRDFITS.
  - `name`: Name of one of the columns read in `tabla`.

  `IDL>print,tabla`

  Print all the data information of the extension read above with MRDFITS.

  - `tabla`: IDL variable that has saved the information read with MRDFITS.

  `IDL>print,hd`

  Print the header of the extension read with MRDFITS.

  - `hd`: Name given to the header of the extension read with MRDFITS.

- Creating FITS files in IDL:

  1. Read data:

     Read data `spectra.dat` and columns from a directory.

     `IDL>readcol,'/Users/.../spectra.dat',col1,col2,col3,col4`

     - `readcol`: Read a free-format ASCII file with columns of data into IDL vectors.

  2. Create structure[1]

[1]There are several data types in IDL: numbers, characters and structures. The structure is a set of several data series and can be mixed with numbers and characters and files of different dimensions.

We must create a structure (in the example below we call the structure `table`) with the data that has been read. The structure is a set of multiple data series. `tmp` (temporal) creates the structure.

For example from `spectra.dat`, we will create a table that has two data sets: one called `pepe` (which will have as much data as column 1) and another called `juan` (which will have as much data as column 2).

```
IDL>tmp={table,$
IDL>pepe:dblarr(n_elements(col1)),$
IDL>juan:dblarr(n_elements(col2))}
```

3. Include data columns:

   ```
   IDL>tmp.(0)=col1[2]
   IDL>tmp.(1)=col2
   ```

   Another way to do the same is:

   ```
   IDL>tmp.pepe=col1
   IDL>tmp.juan=col2
   ```

4. Creating the header:

   Create a header named `header`, with a number of rows as column 1 and call the extension `'prueba'`

   ```
   IDL>FXBHMAKE,header,n_elements(col1),'prueba'
   ```

   - `FXBHMAKE`: Utility in IDL that create basic FITS binary table extension (BINTABLE) header.

   ```
   IDL>print,header
   ```

   or:

   ```
   IDL>print,name_of_the_header
   ```

   - `print`: print header created above with `FXBHMAKE`.

   To add information to the header, use the utility:

   ```
   IDL>SXADDPAR,header,'COMMENT','additonal comments','more comments'
   ```

   - `SXADDPAR`: Procedure in IDL to add or modify a parameter in a FITS header array.

5. Creating the FITS file:

   Create a FITS file called `'prueba_file.fits'` with the header created previously (`header`) and the information of the variable `tmp`.

   ```
   IDL>MWRFITS,tmp,'prueba_file.fits',header,/CREATE
   ```

   - `MWRFITS`: Procedure that will write an IDL structure to a FITS file.

6. Adding extensions to FITS file:

   ```
   IDL>MWRFITS,tmp,'prueba_file.fits',header,/SILENT
   ```

[2] IDL start columns in 0.

## C.2 *XSPEC* requirements

The file structure for models in *XSPEC* is a FITS format described at:

`http://heasarc.gsfc.nasa.gov/docs/heasarc/ofwg/docs/general/ogip_92_009/ogip_92_009.html`

Additional information at:
`http://www.darts.isas.ac.jp/pub/legacy.gsfc.nasa.gov/software/lheasoft/lheasoft6.3/headas-6.3.2/ftools/spectral/tables/`

`ftp://legacy.gsfc.nasa.gov/fits_info/fits_formats/docs/`

## C.3 Preparing data for *XSPEC*

### C.3.1 ASCII TABLES

The ASCII tables were created with the *IDL* program `create_ascii.pro`, but it can be created with any tool. The important is that the ASCII files contain the necessary information to create the FITS tables to *XSPEC*.

Program to create ascii tables: `create_ascii.pro`
Compile line: `IDL>.r create_ascii.pro`
Run line: `IDL>ascii`

The FITS file, contain three extensions that are described below.

- EXTENSION 1: PARAMETERS

  Extension that contains the values of the parameters. In our case the parameter is the mass of the white dwarf with values:

  $M_{WD} = (0.6,\ 0.7,\ 0.8,\ 0.9,\ 1.0,\ 1.1,\ 1.2,\ 1.3,\ 1.4) M_{\odot}$

  column 1, row 1: name of the parameter (In our case: `masa`).

  column 2, row 1: Method; 0 if linear, 1 if logarithmic (In our case: 0:linear).

  column 3, row 1: Initial; initial value in the fit for the parameter.

  column 4, row 1: Delta; parameter delta used in the fit.

  column 5, row 1: Minimum; hard lower limit for parameter value.

  column 6, row 1: Bottom; soft lower limit for parameter value.

  column 7, row 1: Top; soft upper limit for parameter value.

  column 8, row 1: Maximum; hard upper limit for parameter value.

column 9, row 1: Numbvals; number of tabulated parameter values (In our case there are 9 values for the parameter mass).

column 10, row 1: Value; the tabulated parameter values. In this column should appear all the values for the parameter (0.6 0.7 0.8 0.9 ...)

Dimension: $[n\ columns \times 1\ row]$ (n=parameter values).

In our case: $Dim = [10\ columns \times 1\ row]$ But in the column 10 we have 9 values.

- EXTENSION 2: ENERGIES

  Extension containing the energy bins. The energy interval is from $0.1$keV to $100$keV with steps of $0.1$keV.

  Should contain two columns of data where the first column are the values for bins starting with the lower energy bin and the second column finishing with the higher energy bin.

  Dimension: $[n\ columns \times \#\ row]$ (n=low and high value of energy).

  In our case, we have 1000 energy bins: $Dim = [2\ columns \times 1000\ row]$

- EXTENSION 3: SPECTRA

  Extension containing the spectra and parameter values. Should contain two columns. The first column are the values for the parameter and the second column contain all the information of the spectra (In our case 1000 values of $F_E$).

  Dimension: $[n\ columns \times \#\ row]$ (n=2; n=1:parameter values and n=2:spectral information).

  In our case, we have 1000 values of $F_E$ and 9 values for the parameter ($M_{WD}$):

  $Dim = [2\ columns \times 9\ row]$; where column 2 has 1000 values.

### C.3.2 FITS TABLES

Once the ASCII data files have been created, we can create the FITS tables.

In our case, we created two FITS files. One using the spectra calculated with cooling approximation of Zombeck and another using the results of the cooling function of Sutherland & Dopita.

Program to create FITS tables: `tabla_xspec.pro`
Compile/run line[3]:

```
IDL>tabla_xspec,'prueba0','par_zkmass.dat',
'energies_zkmass.dat','spectra_zkmass.dat'


IDL>tabla_xspec,'prueba0','par_SDmass.dat',
'energies_SDmass.dat','spectra_SDmass.dat'
```

[3]Where prueba0 is the output name of FITS file.

The program `tabla_xspec.pro` create FITS files for *XSPEC*.

- Output File: (In the example above: `prueba0.fits`)
  - Zombeck: `ipzk.fits`
  - Sutherland & Dopita: `ipsd.fits`